Molecular Dynamics-Based Study of the Effect of Hydrogen on the Mechanical Properties of Fe-C System

Carlos Martínez

A Thesis
In the Department of
Mechanical, Industrial and Aerospace Engineering

Presented in Partial Fulfillment of the Requirements
For the Degree of
Master of Applied Science (Mechanical Engineering)
at Concordia University
Montreal, Quebec, Canada

June 2024

CONCORDIA UNIVERSITY

School of Graduate Studies

This is to certify that the thesis

prepared By: Carlos Martínez

Entitled: Molecular Dynamics-Based Study of the Effect of Hydrogen on the Mechanical Properties of Fe-C System

and submitted in partial fulfillment of the requirements for the degree of

Master of Applied Science (Mechanical Engineering)

complies with the regulations of the University and meets the accepted standards with respect to originality and quality.

Signed by the final Examining Committee:

Dr. Behrooz Yousefzadeh Chair

Dr. Behrooz Yousefzadeh Examiner

Dr. Michel Trudeau Examiner

Dr. Mamoun Medraj Supervisor

Approved by *Dr. Martin Pugh*

Dr. Martin Pugh, Chair of Department

2024 *Dr. Mourad Debbabi*

Dr. Mourad Debbabi, Dean of Faculty

Abstract

Molecular Dynamics-Based Study of the Effect of Hydrogen on the Mechanical Properties of Fe-C System

Carlos Martínez

Hydrogen embrittlement (HE) significantly impacts high-strength steels by reducing ductility and promoting brittleness. Research has shifted towards multifaceted approaches, with molecular dynamics (MD) simulations at the atomic scale being crucial. In this research, MD was employed using two interatomic potentials to investigate the role of hydrogen in Fe-C systems. The atomic models maintained a consistent carbon concentration while varying concentrations of hydrogen and progressed from single-crystalline through bicrystalline to polycrystalline models, increasing complexity and incorporating grain boundaries (GBs). Results showed a general decline in mechanical properties of the Fe-C system with increasing hydrogen content, with the failure outcome being influenced by simulation boundary conditions such as fully-periodic compared to shrink-wrapped in the pulling direction. The impact of hydrogen varied by crystal direction, highlighting anisotropy. Hydrogen significantly increased local vacancy and void formation, leading to earlier fracture initiation, and strongly suggesting the hydrogen-enhanced strain-induced vacancies (HESIV) mechanism among those commonly proposed for HE. Although evidence for the hydrogen-enhanced decohesion (HEDE) mechanism was limited, a potential synergistic effect with HESIV was suggested. The influence of hydrogen on dislocation density varied, and phase transformations (BCC to FCC/HCP) were frequent, driven by stress, crystal orientation, and potential type. Despite limitations, MD provides key insights into HE, underscoring the need to integrate simulation results with experimental data for a comprehensive understanding.

Acknowledgements

I extend my deepest gratitude to my parents, Eddy Martínez and Cecilia Chacín. Their unwavering support and exemplary values have influenced not only me but also my siblings, and their teachings about pursuing our passions while maintaining life's balance have been invaluable.

To Alejandro, Juan, and Raquel, my siblings, your individual journeys have been a testament to our parents' teachings. Each of you has been an inspiration, teaching me in your own unique ways.

My heartfelt thanks go to my dear wife, Alexa. Ever since our paths crossed, her love and unwavering support have been my pillar of strength, making even our long distance phase, while I was studying this master's, seem totally manageable.

Prof. Mamoun Medraj, my esteemed supervisor, deserves special mention. His faith in me, paired with his consistent guidance and support, both professionally and personally, has been a foundation of my academic journey.

I am profoundly grateful to Dr. Rajwinder Singh, my postdoc. His expertise, especially in introducing me to the realm of molecular dynamics simulations and his deep knowledge in material science, has been instrumental to my research.

To my lab mates, who are more like friends than colleagues, thank you for the camaraderie, shared experiences, and collective knowledge.

I would like to express my sincere appreciation to Safran Landing Systems. Their generous financial backing has been central, making this research effort possible.

Lastly, I am indebted to the Digital Research Alliance of Canada. Their exceptional HPC service and unwavering support played a crucial role in the simulation aspect of this work.

Table of Contents

List of Figures

List of Tables

Chapter 1: Introduction, Problem Statement and Thesis Layout

1.1 Introduction

HE is a phenomenon that affects steels and other metals [1]. It causes a significant decrease in ductility, ultimately leading to premature failure under stress [2]. Hydrogen has remarkable properties and has been, for quite some time, been promoted as fuel for zero carbon emission [3]-[5]. However, it can dissolve in most metals and metal alloys in various ways, such as during melting, electrochemical reactions (e.g., electroplating process), pickling, and welding [6], [7], and its interaction with crystal lattice features are a reason for concern in iron, steel, and other metals used in engineering [8]. Problems generated by the presence of hydrogen in materials are manifested in numerous ways, for instance, hydrogen-induced cracking, hydride cracking and other deleterious effects, often leading to catastrophic fracture [8]. Needless to say, as catastrophic failure is unacceptable in engineering, detrimental effects of hydrogen need to be reduced as much as possible.

Despite the extensive study of HE over the years, the exact nature of this phenomenon remains elusive. This is primarily due to its interdisciplinary nature, encompassing fields such as electrochemistry, materials science, and mechanics, which makes a comprehensive understanding difficult. In addition to the fact that direct experimental detection of hydrogen behavior poses a significant challenge due to the mobility of its atoms, its typical low concentration further limits the information about its states in materials, leaving much of the understanding speculative [9]. However, recent breakthroughs in experimental techniques are revealing the embrittlement entity and providing new insights into the mechanisms of HE [9], [10]. The initiation of this process begins when hydrogen diffuses into the metal from the environment. It adheres to the surface in the form of H_2 molecules or H_3O^+ ions before dissociating into single atoms and diffusing into the

material [11]–[13]. Hydrogen atoms at interstitial sites represent the majority of the total hydrogen atoms at thermal equilibrium and significantly influence the transport and distribution of hydrogen at various trap sites [13]–[15]. While direct determination of the location can be difficult (small solubility and high diffusivity of hydrogen), the preferential occupancy is at the tetragonal site (T-site) over the octahedral site (O-site) in a BCC lattice, shown by density functional theory (DFT) calculations of the total energy of the solid solution [16], [17].

Various mechanisms of HE have been proposed [10], including hydrogen-enhanced decohesion (HEDE), hydrogen-enhanced localized plasticity (HELP), and hydrogen-enhanced strain-induced vacancies (HESIV), among others. This work will focus mainly on these three mechanisms, being some of the most important [14], [15], [18].

Due to the elusive nature of hydrogen, the limitations of experiments become pronounced, including the inability to observe atomic-level interactions in real time, the complexity in isolating individual HE mechanisms, and the intricacy in maintaining controlled environments [19]–[22]. Complementing experimental and theoretical approaches, MD simulations have emerged as a valuable tool in the study of HE [23]. These simulations have the potential to provide new insights into the underlying mechanisms of HE and contribute to the development of more robust and resistant materials [24]. This work aims to qualitatively evaluate the influence of hydrogen on mechanical behavior of Fe-C alloys using MD simulations. Increasingly complex models will be used, starting with single-crystalline systems in three different orientations, progressing to two bicrystalline models, and culminating with a polycrystalline model, all subjected to tensile loading. The detailed methodology is presented in Chapter 3.

The goal of this work is to enrich the current understanding of HE in Fe-C systems and contribute to the existing body of knowledge by providing new insights derived from MD simulations.

1.2 Problem Statement

Studying the HE of steels using MD as a complementary tool to experiments is of great importance in the contemporary research domain, serving as a valuable complement to experimental studies. With growing interest in deciphering the mechanisms behind HE, MD offers unique insights that can bridge the gaps in the current understanding [25], [26]. However, most of the current MD studies of HE focus on potentials designed specifically for Fe-H interactions [18], [23], [25]–[32]. This thesis aims to broaden the scope by employing two recent ternary interatomic potentials for Fe-C-H systems, a Bond Order Potential (BOP) and a Modified Embedded Atom Method (MEAM) potential, to study the changes in mechanical properties of the Fe-C system in the presence of hydrogen.

1.3 Thesis Layout

This thesis begins with a literature review, showcasing current experimental and simulation work in the field. Then, it dives into the basic theory behind MD, establishing a theoretical backdrop. The methodology section delves into the creation of single-crystalline, bicrystalline, and polycrystalline models, detailing hydrogen concentrations, number of atoms for Fe, C, and H, as well as boundary conditions, type of loading (applied either directly as strain rate or indirectly as velocity rate), types of results reported (which include the stress-strain response, changes in phase distribution with strain, vacancy count with strain, and dislocation density variations with strain), and how the results are grouped to be presented. Following this, the results and discussion section expands on the results and presents them, per group of results (labelled as “cases”), comparing the base Fe-C system against the systems with different hydrogen concentrations. This is complemented by a discussion grounded in the literature review, which then culminates with the conclusion and future steps, summarizing learnings and suggestions for further exploration.

Chapter 2: Literature Review and Key Theoretical Concepts

2.1 Literature Review

In this section, a comprehensive analysis of existing research relevant to the study is provided. The purpose of this exploration is to understand the current state of knowledge, identify gaps in the literature, and lay the groundwork for the research questions. Examination of previous work establishes a framework for this study, highlighting its significance and contribution to the field. The following discourse will go into various findings and theoretical foundations that shape the area of focus.

HE was first identified in the late 19th century by the British scientist W. H. Johnson [33]. It was found that iron and steel were susceptible to hydrogen-induced damage, as a remarkable change in some of the mechanical properties of iron was observed, caused by its temporary immersion in hydrochloric and sulfuric acid. These changes are made evident due to the extraordinary decrease in toughness and breaking strain of the treated iron. Furthermore, even more remarkable, the change in properties was not permanent, as after a lapse of time the metal slowly regained its original toughness and strength. In the pursuit of understanding the source of these changes, a number of experiments were made by Johnson from time to time, some of which were conducted at a large scale in an iron mill where the quantities of sulfuric and hydrochloric acid were used to remove the oxide coating in the iron wire, before drawing it. This discovery sparked over a century of scientific research to understand how HE occurs [10], [34]–[37].

Before and at the beginning of the 20th century, the development of new technologies and industries, including the automobile, aerospace, and power generation industries, increased the demand for durable and reliable metals and emphasized the importance of understanding and

avoiding HE [38]–[42]. During this period, researchers conducted a series of experiments designed to study how hydrogen affects various metals and alloys under different conditions [35], [38], [43]–[45].

By mid-20th century, the presence of hydrogen was recognized to severely degrade the mechanical properties of steels, leading to catastrophic failures when loaded [46]. In a notable study, Troiano [37] demonstrated that hydrogen could be introduced into metals by a variety of mechanisms, including electrochemical reactions, contact with environments containing hydrogen, and high-temperature processes. This work also showed that HE was more pronounced in high-strength steels. These steels were increasingly used in critical applications such as bridge and building construction, pressure vessels, penstocks, automotive applications, aerospace applications (landing gears, fuel tanks, engines, among others), etc. [47]–[55].

Throughout the 20th century, HE research evolved as researchers developed new experimental techniques and theoretical models to understand this complex phenomenon [34], [36], [46], [56]–[62]. Advances in technology have also led to the emergence of new industries and applications, such as nuclear energy and 3D printing, in which HE could pose a significant risk, further emphasizing the importance of this research [63]–[67]. A wealth of experimental work has proposed various HE mechanisms, including:

- Hydrogen Enhanced Localized Plasticity (HELP), where hydrogen accumulated at dislocations, precipitates, and grain boundaries (GBs), among other locations, decreases the interaction energy of dislocation-obstacle interactions and assists the deformation processes locally, where hydrogen is present [10], [14], [32], [68]–[71].

- Hydrogen Enhanced Decohesion (HEDE), which proposes that interstitial hydrogen lowers the cohesive strength by dilatation of the atomic lattice, resulting in intergranular failure [14], [71]–[73].
- Hydrogen Enhanced Strain Induced Vacancies (HESIV), where hydrogen enhances the formation and coalescence of vacancies, resulting in fracture [14], [74]–[77].

Nonetheless, it is suggested that these mechanisms often act synergistically rather than in isolation. Many studies indicate a common interaction between multiple HE mechanisms, particularly HELP + HEDE [68], [72], [78]–[88]. While some HE mechanisms may be more dominant, no single mechanism seems to fully explain the phenomenon by itself. Consequently, there has been a growing reliance on various experimental, theoretical, and computational approaches to help understand this complex phenomenon. In particular, atomistic simulations have been increasingly used to test nanoscale systems and provide a valuable avenue for exploring the mechanisms underlying HE in metals [24], [27]–[29], [32], [89], [90]. Notably, MD simulations have emerged as a powerful tool for the study of HE at the atomic scale, providing valuable insights into the fundamental processes that underlie HE, such as hydrogen-metal bonding and the nucleation and propagation of hydrogen-induced cracks [90]. While MD can help to a great degree in understanding HE in metals (hoping to study mechanisms such as HELP, HEDE and HESIV), it can be limited by a few factors, such as the need for a validated interatomic potential, simulations being normally performed at very high loading rates (which minimizes or eliminates important kinetics that happen at lower rates, like hydrogen diffusion, plastic flow, and slow crack growth) and limitation of computational power [27]–[29]. These factors are being addressed over time as more interatomic potentials are developed, validated, and computational power is steadily increased, leading to more complex simulations and reduced computational time. On the other

hand, by performing targeted simulations, it is possible to qualitatively (and sometimes quantitatively) evaluate in detail the proposed mechanisms of hydrogen effects in metals [28]. Nevertheless, as already mentioned, MD results must be objectively evaluated based on their dependency on the details of the interatomic potential [29].

Despite these challenges, recent advances in computational power and the development of more accurate and transferable interatomic potentials have enabled MD simulations to address increasingly complex and realistic material systems. This has allowed researchers to investigate the role of microstructural features (such as GBs, dislocations, and vacancies) in hydrogen trapping and embrittlement [91]. New interatomic potentials for Fe-C-H systems that closely represent the composition of real steels became recently available, such as the ones developed by Zhou et al. [92] in 2020 and Mun et al. [93] in 2023 (more information about these two potentials will be given in a subsequent section). MD simulations are expected to play an even more important role in future research as the understanding of HE continues to evolve. For example, multiscale modeling approaches that combine atomistic-level MD simulations with larger-scale simulations (e.g., dislocation dynamics and finite element models) hold promise for bridging the gap between atomic-scale processes and macroscopic material behavior [94]. The development of more resilient materials and effective mitigation strategies against HE may be facilitated by this integrated approach.

Already having been through an overarching perspective of the prevailing theories, mechanisms, and experimental (and simulation) approaches in the field, a more nuanced exploration of selected research will be presented. This more in-depth analysis serves to complement the general information already shown, offering a thorough examination of key studies (some were already briefly mentioned above and some are new) that have shaped the current understanding. By going

into these specific investigations, the aim is to illuminate intricate details and complex relationships that may not be apparent in a broader context. The ensuing discussion will thus focus on meticulously unraveling these critical aspects, allowing a more comprehensive appreciation of the subject matter.

Djukic et al. [72] focused on the relationship between the microstructures of steels and HE mechanisms. Interestingly, the research sets forth that the primary mechanisms for HE can shift based on the experimental setup. The findings also suggest that both HELP and HEDE mechanisms coexist in a variety of steel types, with the roles of various trapping sites such as GBs, vacancies, and dislocations as illustrated in Figure 1. A key take-away from the work is that the transition between ductile and brittle fractures due to HE is governed by several factors, including stress accumulation from increased local plasticity and the specific conditions of hydrogen diffusion and concentration. For instance, lower hydrogen levels and stress conditions favor HELP, while higher concentrations and stress conditions favor HEDE. This study underscores that current experimental conditions often mask the interplay between HELP and HEDE, leaving questions open about intricate influences of hydrogen on steel deformation. Complementing the research of Djukic et al., Ogawa et al. [95] proposed a synergistic HELP + HESIV + HEDE model, as shown in Figure 2. Through extensive fatigue crack growth (FCG) tests on commercially pure iron, the intricacies of brittle-like intergranular fractures are illuminated. Figure 3 gives an in-depth look at the effects of hydrogen near the tip of a fatigue crack, also close to GBs, emphasizing the role of hydrogen-enhanced dislocation structures (HELP) at the crack tip. These dislocations then pile up and deposit hydrogen at the GBs, facilitating intergranular (IG) crack propagation paths once the original crack reaches the GB. This happens together with microvoids formed along the GBs and in the lattice, underscoring the multifaceted nature of HE.

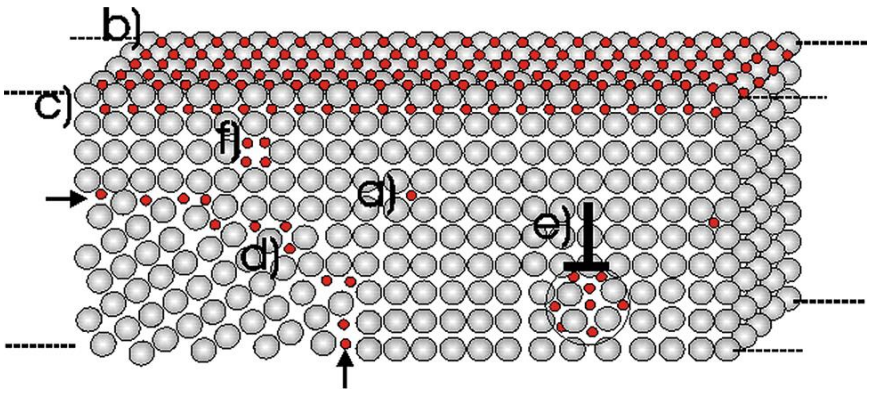

Figure 1 – Schematic that shows the different trapping sites for hydrogen in steels: (a) interstitial sites; (b) surface traps; (c) subsurface traps; (d) GB traps; (e) dislocation traps; (f) vacancy traps. Courtesy of Pundt et al. [96].

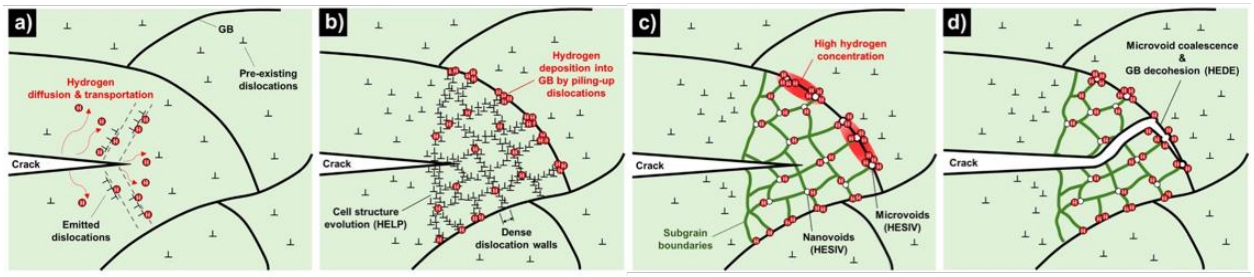

Figure 2 – Schematic showing the HELP, HESIV and HEDE mechanisms can work together to produce an IG crack propagation in pure iron. Courtesy of Ogawa et al. [95].

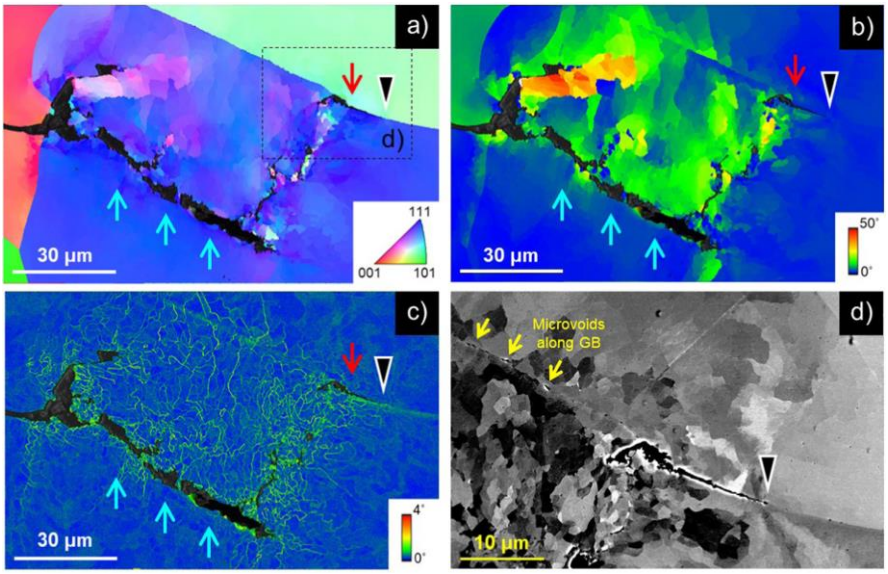

Figure 3 – Observation of the fatigue crack propagated in hydrogen gas. The crack grows from left to right, first inside the adjacent grain and then along the GB. Notice how microvoids form along the GB too. Courtesy of Ogawa et al. [95].

In the presence of hydrogen, vacancy formation when strain is applied is an important angle of current research on HE, particularly the HESIV mechanism. A study done by Sakaki et al. [97] focuses on the effect of hydrogen on vacancy formation in iron during plastic deformation. It was discovered that the presence of hydrogen primarily results in an increase in vacancy aggregation, rather than the proliferation of dislocations, supported by the data presented in Table 1. It illustrates roughly 4.8 times the number of vacancies formed in the hydrogen precharged sample in comparison to the non-precharged sample, even though the density of dislocations remains largely unaffected, supporting HESIV and pointing away from HELP. Sugiyama and Takai [71] complement the discussion by conducting experimental research on the influence of hydrogen in forming diverse lattice defects in pure iron specimens, under plastic strain, employing low-temperature thermal desorption spectroscopy (L-TDS). It was concluded that hydrogen plays an effective role in promoting vacancy formation and localizing the dislocation configuration near the GBs, without altering the number of generated dislocations. This once again supports HESIV. HELP could also be supported, even if the number of dislocations remained the same, as they were localized due to the presence of hydrogen. Figure 4 provides visual evidence for the changes in grain reference orientation deviation values induced by hydrogen, clearly showing increased grain orientation deviation near the GB (as shown within the red dotted line), indicating a localized intragranular strain instead of more uniform strain as seen in the specimen without hydrogen.

Table 1 – Results of deformed iron with and without hydrogen. Notice how vacancy concentration increases drastically and dislocation density remains virtually the same. Courtesy of Sakaki et al. [97].

Strain	Hydrogen	C_d ($\times 10^{10}$/cm^2)	C_v ($\times 10^{-7}$)
10%	Non-charged	1	–
	Charged	0.9	1.7
20%	Non-charged	2.2	1.7
	Charged	1.9	8.2

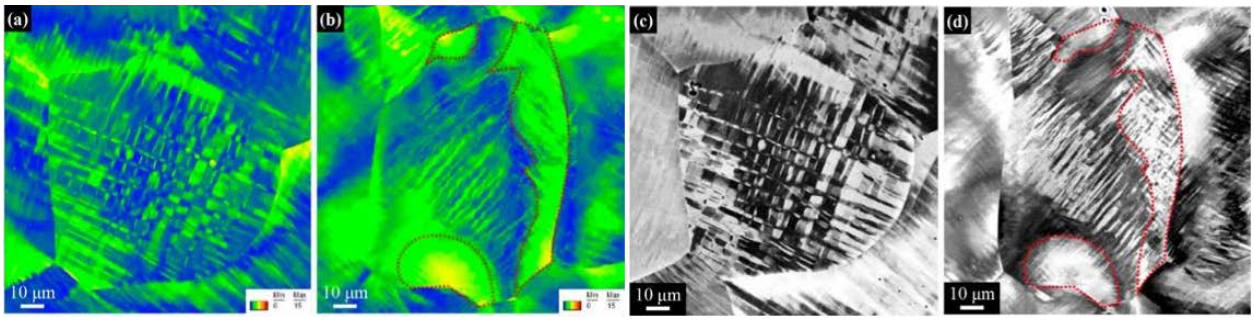

Figure 4 – EBSD-derived GROD maps for specimens at (a) 25% ε_p and (b) H + 25% ε_p, along with ECC images corresponding to (c) 25% ε_p and (d) H + 25% ε_p specimens. Courtesy of Sugiyama and Takai [71].

Building on this, the interaction of dislocations and hydrogen-vacancy complexes in α-Fe was studied using MD simulations by Li et al. [89]. It was shown that, unlike simple lattice vacancies, hydrogen-vacancy complexes are not absorbed by dislocations traversing the lattice. This led to an increased vacancy concentration during plastic deformation in the α-Fe system with hydrogen. Figure 5 illustrates such phenomenon. Such findings suggest that hydrogen could be instrumental in creating more vacancies and preventing their absorption by dislocations during the process of plastic deformation, supporting HESIV. In a more general approach, Matsumoto et al. [32] studied the impact of hydrogen in BCC iron through various MD simulations, ranging from crack growth and nanoindentation to tensile loading, and employing a unique interatomic potential for BCC iron. This potential was adjusted to account for the effects of pseudo-hydrogen, showing that the presence of hydrogen could indeed induce early yielding and rupture. The results, illustrated in Figure 6, provide a visual representation of this, showcasing the significance of the HESIV mechanism as an increase in vacancy formation during loading is identified.

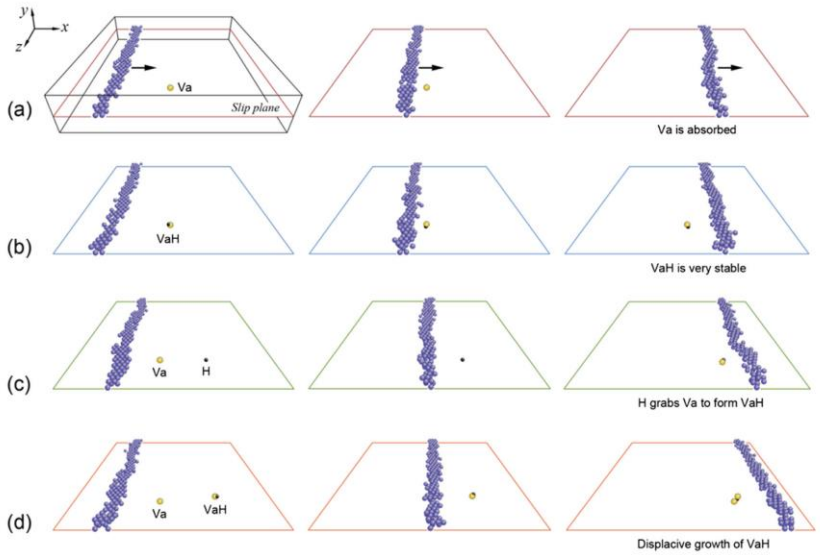

Figure 5 – Illustration showing the high stability of hydrogen-vacancy complex when interacting with dislocations. Hydrogen can stabilize vacancies within the material, preventing them from being absorbed by passing dislocations. Additionally, hydrogen may even capture other vacancies that have previously been absorbed by the dislocations. Courtesy of Li et al. [89].

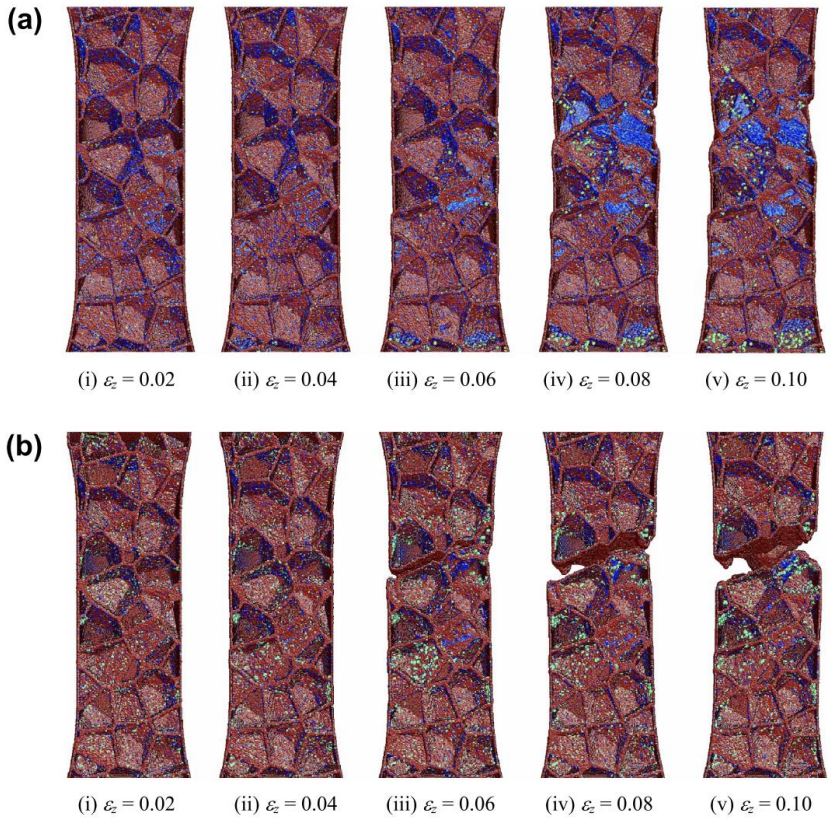

Figure 6 – Illustration of the different results between (a) iron without hydrogen effects, and (b) iron with pseudo-hydrogen effects. The color coding is as follows: red represents surfaces; light blue, stacking faults; dark blue, partial dislocations; green, vacancies. A comparison of the two shows that the system incorporating pseudo-hydrogen effects fractures at a lower strain and is a noticeable increase in the number of vacancies formed. Courtesy of Matsumoto et al. [32].

Continuing on the side of MD simulations, Song et al. [27], [28] provided a comprehensive investigation through MD simulations on HE in iron. While the focus was on the mechanical properties and how hydrogen played its part, a new mechanism for HE was proposed and demonstrated (see Figure 7). This mechanism does not encompass all experimental observations but establishes a firm base in understanding the brittle fracture associated with HE. Interestingly, the findings also illuminate the fact that hydrogen hindered the motion of edge dislocations, thus challenging the commonly proposed mechanisms for HELP. In a similar manner, Gou et al. [98] further suggested the lack of the HELP mechanism, by conducting an in-depth investigation into hydrogen-induced cracking (HIC) in welded X80 pipeline steel. The approach was multifaceted, combining impact tests, slow strain rate tensile tests, and MD modeling. The results identified a heightened susceptibility to HIC, especially within the coarse-grained heat-affected zone, which displayed distinct intergranular brittle fracture following hydrogen charging. It was proposed that the presence of hydrogen atoms obstructs the emission of dislocations, causing energy accumulation that is eventually released through crack initiation. Table 2 shows the mechanical properties (for all types of samples) that resulted from experiments, revealing that the presence of hydrogen does affect these properties negatively. Visual evidence, as seen in Figure 8, offers a stark contrast between the base metal with and without hydrogen charging, as the absence of hydrogen results in a fracture surface with typical ductile characteristics, contrary to a more cleavage-like fracture surface under the presence of hydrogen. Matsubara [31] then proceeded to investigate tempered lath martensitic steel, both experimentally and via MD simulations. It was observed that in hydrogen-rich environments, cracks showed a distinct pattern, propagating by linking isolated interfacial failures ahead of the crack tip. Figure 9 uses EBSD maps to contrast microcrack initiation in steel within air and hydrogen environments, showing that cracks start

within a grain in air but along GBs in hydrogen, with less plastic deformation indicated by sparse high kernel average misorientation (KAM) values in the hydrogen environment. This suggests the role of hydrogen in inhibiting dislocation emission, pointing once again away from HELP. Nonetheless, the presented MD simulations on twist GBs illustrate (in Figure 10) how hydrogen affects the stress-strain response differently based on misorientation angles, as hydrogen can enhance, inhibit, or not affect the dislocation emission depending on the twist at the GBs, suggesting the role of anisotropy in both the promotion and inhibition of dislocation emission.

In contrast, supporting the presence of HELP, Xing et al. [99] recently (in 2024) conducted an MD study on hydrogen-induced plastic deformation and cracking in α-Fe. The interatomic potential employed for iron was developed by Mendelev et al. [100], fitting the iron-hydrogen interaction with DFT calculations. This study proposed that hydrogen, in effect, enhances dislocation emission in the [110]<111> slip system, while inhibiting it in other slip systems, but only up to a critical concentration, as shown in Table 3. Once this concentration is surpassed, dislocation emission is inhibited at GBs, where hydrogen atoms pin dislocations and cause piling-up, generating a stress concentration. This effectively points to HELP, but only inside a certain range of hydrogen concentration. Vacancy generation in the presence of hydrogen was also explored and it was shown that, under strain, vacancy formation increases as hydrogen concentration increases (indicative of HESIV), leading to void generation and coalescence at GBs that results in cracking, as shown in Figure 11. Complementing this, Tomatsu et al. [73] explored hydrogen-induced intergranular failure (HIIF) in a Ni-Cr alloy, highlighting the significance of HELP and HEDE mechanisms while diminishing the role of HESIV. While the study was not centered on steels, it proposes a dislocation nucleation model applicable to high-strength steels, although the contribution ratio of the HELP and HEDE mechanisms might be different from that in the Ni-Cr alloy. Through detailed

examination, the research showcased the importance of the dislocation nucleation and the prevalence of lattice defects beneath the HIIF surface. The results further indicated higher defect densities in certain samples and refuted the involvement of HESIV in HIIF. Figure 12 outlines the HIIF process in the Ni-Cr alloy, emphasizing the collaborative roles of HELP and HEDE. This underscores the complexity surrounding the mechanisms of HE, particularly HELP and HESIV. The varied and occasionally conflicting findings within recent studies suggest that a full understanding is yet to be achieved, emphasizing the continuous need for ongoing research in HE.

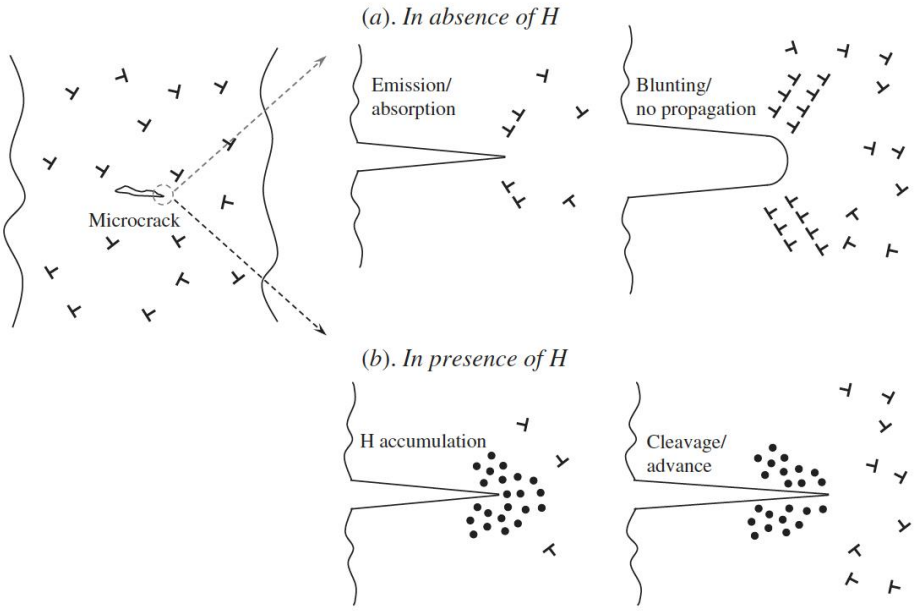

Figure 7 – Schematic showing the behavior of a pre-existing crack during loading, in two scenarios: (a) without hydrogen, where the crack blunts due to the emission and absorption of dislocations; (b) with hydrogen, where hydrogen buildup near the crack tip prevents the emission and absorption of dislocations, causing brittle fracture. Courtesy of Song et al. [24].

Table 2 – Mechanical properties per type of sample tested, with and without hydrogen charging. Courtesy of Gou et al. [98].

Experimental conditions		*UTS* (MPa)	*RA* (%)	*EL* (%)
BM	without hydrogen	654.28	36.61	14.06
	with hydrogen	678.96	8.04	3.94
FGHAZ	without hydrogen	609.27	40.95	19.77
	with hydrogen	544.69	10.67	4.33
CGHAZ	without hydrogen	624.73	25.67	13.06
	with hydrogen	526.10	5.87	2.28

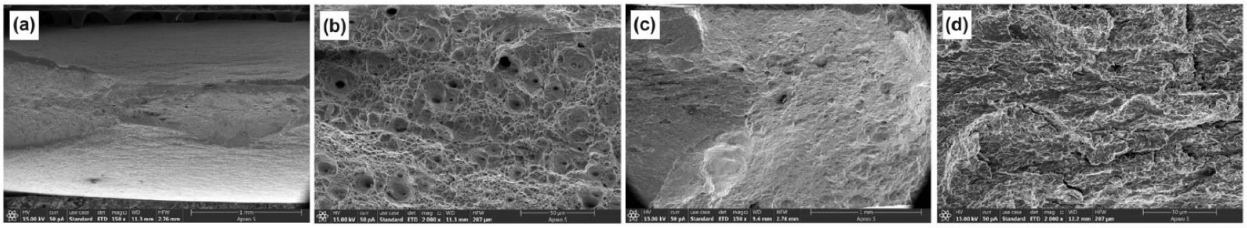

Figure 8 – SEM views of the fracture surface of the base metal specimen without hydrogen: (a) 150x (b) 2000x; and with hydrogen: (c) 150x (d) 2000x. Courtesy of Gou et al. [98].

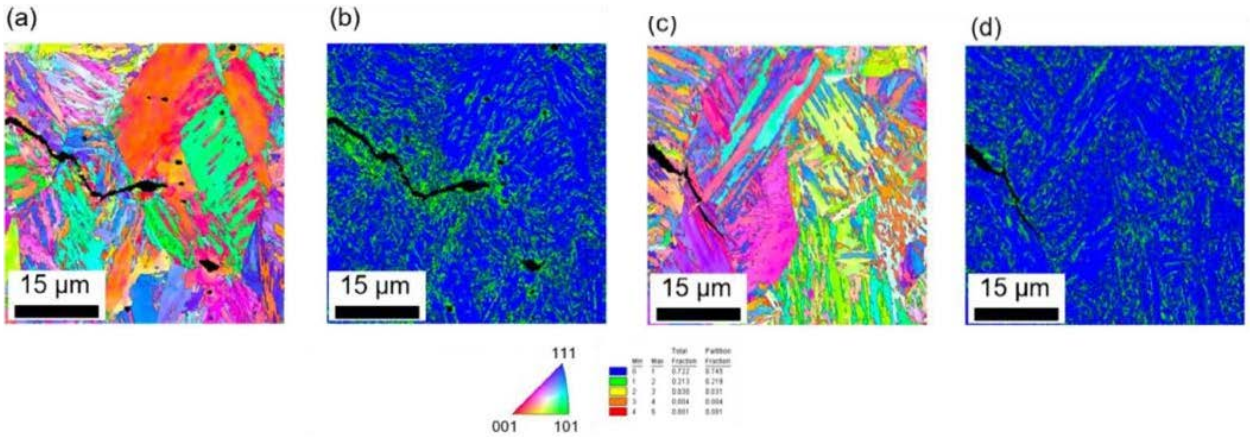

Figure 9 – EBSD examination of crack tip areas formed in (a, b) atmospheric and (c, d) hydrogen gas conditions. Inverse pole figure (IPF) maps are presented in (a) and (c), while KAM maps for the respective areas are displayed in (b) and (d). Courtesy of Matsubara [31].

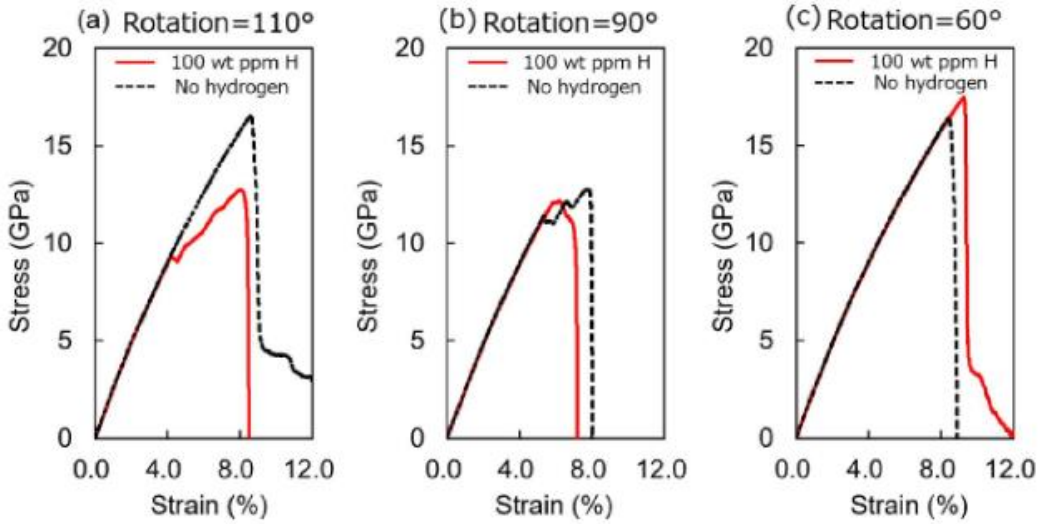

Figure 10 – Stress-strain curves of tensile MD simulations at different twist GBs. Courtesy of Matsubara [31].

Table 3 – Dislocation density in the models with 20 and 30 grains at various hydrogen concentrations. Courtesy of Xing et al. [99].

Hydrogen concentration (H/Fe%)	Overall dislocation density (Å^2)		
	20 grains 12 cycles	6 cycles	30 grains 6 cycles
None hydrogen	0.1167	0.0628	0.0798
0.0005	0.1300	0.0695	0.0839
0.001(critical point)	0.1171	0.0627	0.0862
0.005	0.0994	0.0537	0.0670

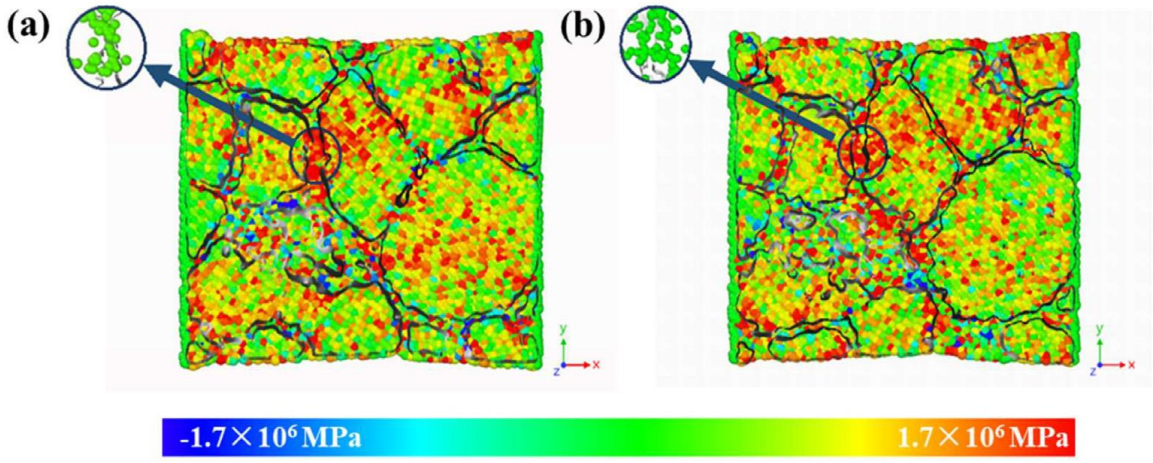

Figure 11 – Vacancy and stress concentration distributions at the GBs. The green bubbles inside the zoomed in area represent vacancies. Courtesy of Xing et al. [99].

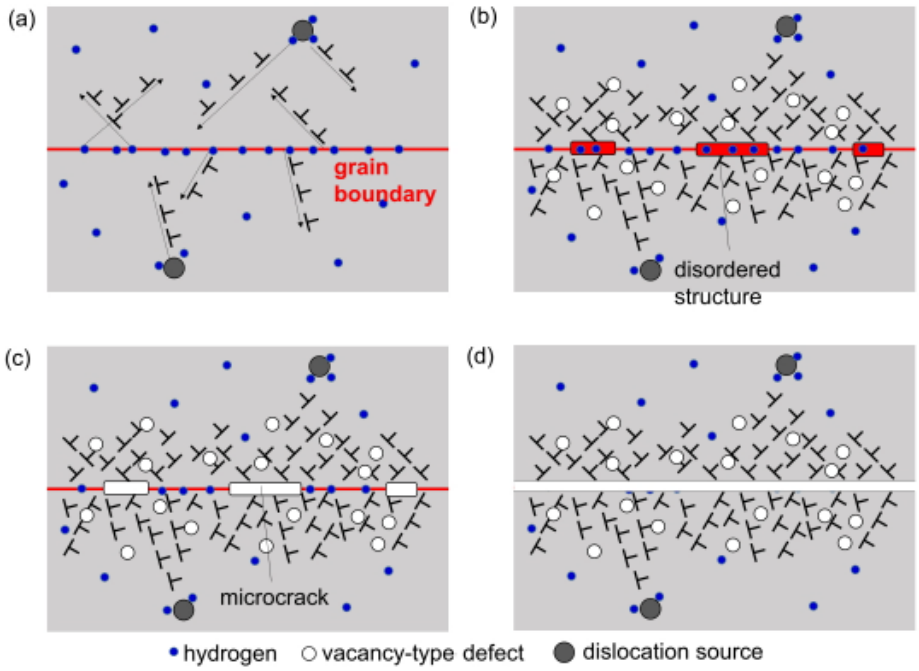

Figure 12 – Schematic representation of the progression of HIIF in the Ni-Cr alloy, illustrating the intertwined roles of the HELP and HEDE mechanisms, from initial dislocation nucleation to the culmination in intergranular fracture. Courtesy of Tomatsu et al. [73].

Further, a curious observation across MD studies is the potential phase transformation from BCC to FCC/HCP in iron systems. Such transformations, often seen in iron systems under high strain rates (inherent in MD), have been reported in various studies, both experimentally [101]–[104] and using simulation [30], [105]–[110], suggesting the role of carbon and hydrogen in facilitating these transitions [107], [108]. Rohr et al. [101] illuminated this through their extensive investigation on high-strength steel (NiCrMoV). At high pressures (surpassing 13 GPa), a transition from BCC to HCP was noted, as represented in Figure 13 which shows a phase diagram plotting temperature with pressure for pure iron. The transition from BCC to HCP occurs at about 13 GPa at a temperature of 300 K. Complementing this work, Nguyen et al. [107], using first-principles simulations, delved into the phase transition from BCC to FCC in iron, driven by interstitial carbon. It was found that carbon positioned at the octahedral interstitial sites promotes the BCC to FCC transition while challenging the reverse process. Similarly, Castedo et al. [108], used first-principles simulations to probe the role of interstitial hydrogen on the phase transformation of iron from BCC to HCP, going through FCC. This transformation sequence aligns with the Bain's model [111], a theoretical model that describes the hypothetical transition between FCC and BCC lattices through coordinated stretching and compression without breaking atomic bonds. The insights from this research [111] suggest that the presence of hydrogen at octahedral interstitial sites generates an intrinsic stress field that can be alleviated by lattice distortion, thereby favoring the sequence of transformations from BCC to FCC and subsequently to HCP.

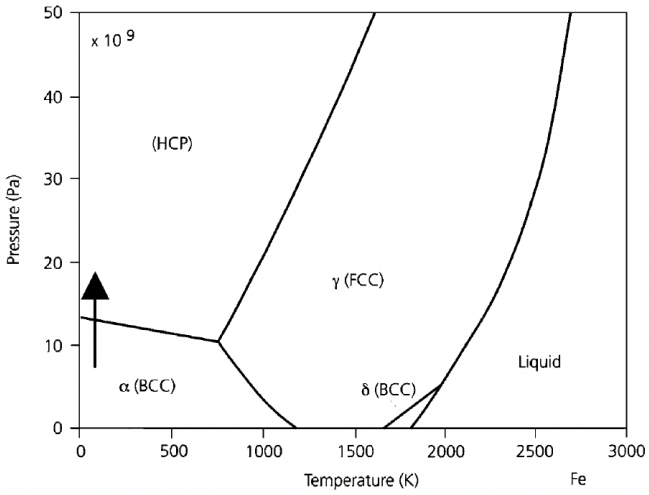

Figure 13 – Phase diagram (temperature against pressure) for pure Fe. The black arrow intersects right where the BCC to HCP transformation occurs at 13 GPa. Courtesy of Rohr et al. [101].

Building on the same discussion of the general influence of hydrogen, a study carried out by Xing et al. [30] employed MD to analyze the brittleness and intergranular cracking tendency in α-Fe due to hydrogen. The work was grounded as well on the potential developed by Mendelev et al. [100], which is very suitable for GB simulations, augmented with DFT calculations. The researchers found that, while hydrogen was seen to typically alleviate stress at GBs, its presence could paradoxically intensify GB volume expansion and lead to intergranular cracking and even phase transformations at the GBs (Figure 14). The influence of hydrogen on GB deformation and dislocation emission is pronounced, especially at smaller excess volumes. It leads to a pinning effect in the $[111](\bar{1}\bar{1}2)$ slip system and an increased mobility in the $[\bar{1}11](110)$ slip system (suggesting HELP in this direction), indicating that hydrogen can both aid and hinder dislocation emission. Ma et al. [112] pursued a similar direction of investigation, examining the effects of external strain on atomic structures within symmetrical GBs in BCC iron, also using the potential developed by Mendelev et al. [100]. Two primary mechanisms were explored: activation of slip systems and dislocation formation, and phase transformation from an initial BCC to an FCC structure. The results highlighted a phase transformation from BCC to FCC structures under strain

(as shown in Figure 15), a phenomenon similarly noted in earlier shock wave investigations on polycrystalline iron by Gunkelmann et al. [105].

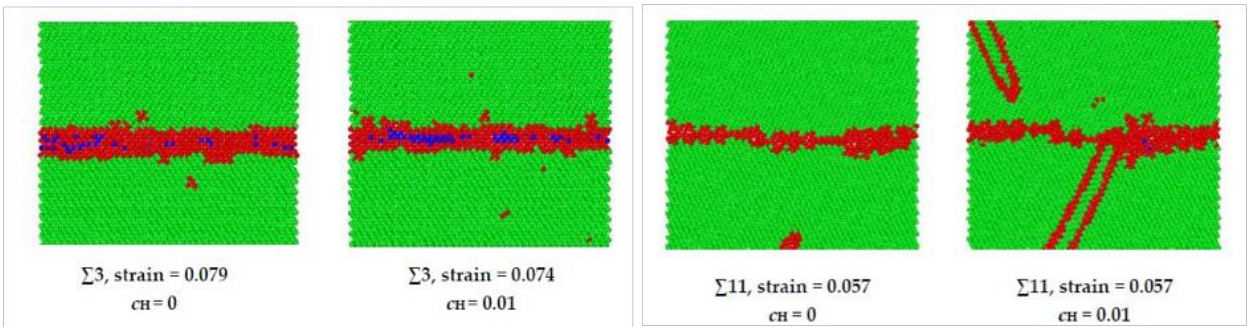

Figure 14 – Results showing phase transition strain in Σ3 GB and twinning emission strain in Σ11. The FCC structure is shown in blue, the BCC structure in green and unknown structures in red. Courtesy of Xing et al. [30].

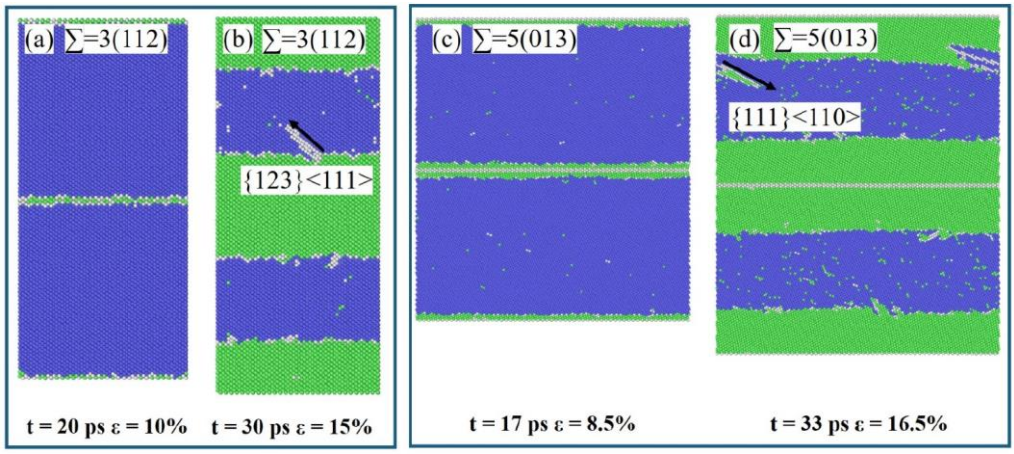

Figure 15 – Snapshots of two different GB configurations. It can be observed how, under strain, the BCC to FCC transformation occurs at the GB and extends from there. Courtesy of Ma et al. [112].

Further widening the spectrum of investigation related to phase transformation, Zhang et al. [102] engineered a microelectromechanical testing device, making it possible to conduct assessments at atomic resolution up to 1556 K. The intricate transitions from BCC to FCC in tungsten at 973 K were disclosed, offering keen insights into phase transformations under strain, an observation notably not exclusive to steel. This BCC to FCC phase transformation seems to favor lattice shearing on the (011) plane. Figure 16 shows detailed TEM images with atomic resolution of the nucleation and propagation of a crack, possible due to the depth of understanding that atomic-level clarity can contribute, and a schematic for the BCC to FCC transformation. Exploring further into

the transformative behaviors of BCC metals, a recent study by Lu et al. [113] disclosed a BCC to FCO (face-centered orthogonal) transition in nano-sized single-crystalline molybdenum. Through high-resolution TEM (HRTEM) imaging, the nucleation of grains transitioning to an FCO phase was observed. This change, modulated by various factors, includes processes like lattice shearing, also favoring {110} planes. First-principles calculations affirm the stability of the FCO phase. Figures 17-19 offer an insightful visualization of this structural evolution observed in their study [113], emphasizing the role of lattice shearing during the transformation. These findings augment the understanding of BCC metal deformations and their structural evolutions. On the other hand, Wang et al. [104] studied the phase transformation of iron under static pressure, utilizing postmortem samples analyzed with TEM. The estimated peak pressure near the loading surface reached ~16.4 GPa, significantly exceeding the predicted stress threshold (~13 GPa) for the initiation of martensitic transformation under hydrostatic conditions. Microstructural fingerprints were traced to a reversible martensitic transformation (α→ε→α). Signature characteristics, such as needle-like regions and three sets of {112}<111> twins exhibiting a threefold symmetry, distinctly indicate the occurrence of martensitic transformations during the reversible α→ε phase transition, even though no ε is retained after the pressure is released. The transformed areas could be differentiated from areas without martensitic transformation, enabling a quantitative evaluation of the transient ε-phase formed at different locations and pressures under shock-loading in a polycrystalline sample. Figure 20 illustrates the transformation in α-Fe through an inverse pole figure color map and Figure 21 provides a schematic overview of the α→ε→α phase transformations. Complementing this study, Hawreliak and Turneaure [103] utilized broadband x-ray diffraction to investigate the reversible BCC to HCP phase transformation in [100]-oriented single crystal iron under high pressure. The experiments involved shock compressing iron samples

to pressures exceeding 25 GPa, effectively surpassing the α→ε transition threshold. This transformation was observed to be reversible upon uniaxial strain release, demonstrating a transformation memory effect with minimal stress hysteresis and indicating unique phase transition pathways under dynamic strain conditions, differing from the Burgers mechanism [114]. In this mechanism, the crystal structure is altered through simultaneous shear deformation with alternating repositioning of the adjacent atomic planes, described as $(110)_{bcc} \parallel (0001)_{hcp}$ and $[\bar{1}11]_{bcc} \parallel [\bar{2}110]_{hcp}$.

These studies undoubtedly offer a valuable foundation for interpreting phenomena observed in MD studies of BCC systems, including iron. Numerous MD simulations [115]–[117] have been conducted on iron nanowires, confirming the phase transformations reported in the corresponding experimental research. Nonetheless the role of hydrogen in these types of transformations remains undetermined experimentally.

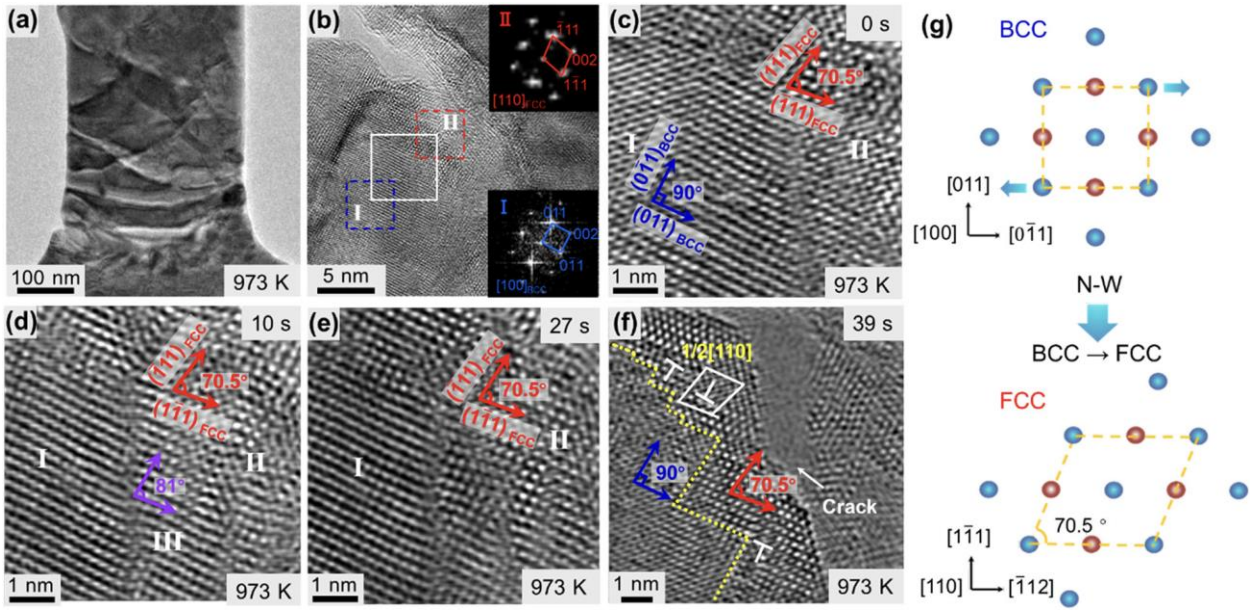

Figure 16 – HRTEM observation of strain-induced BCC-FCC phase transformation and crystallographic schematic of the BCC-FCC phase transformation by habit plane shear of the lattice. Courtesy of Zhang et al. [102].

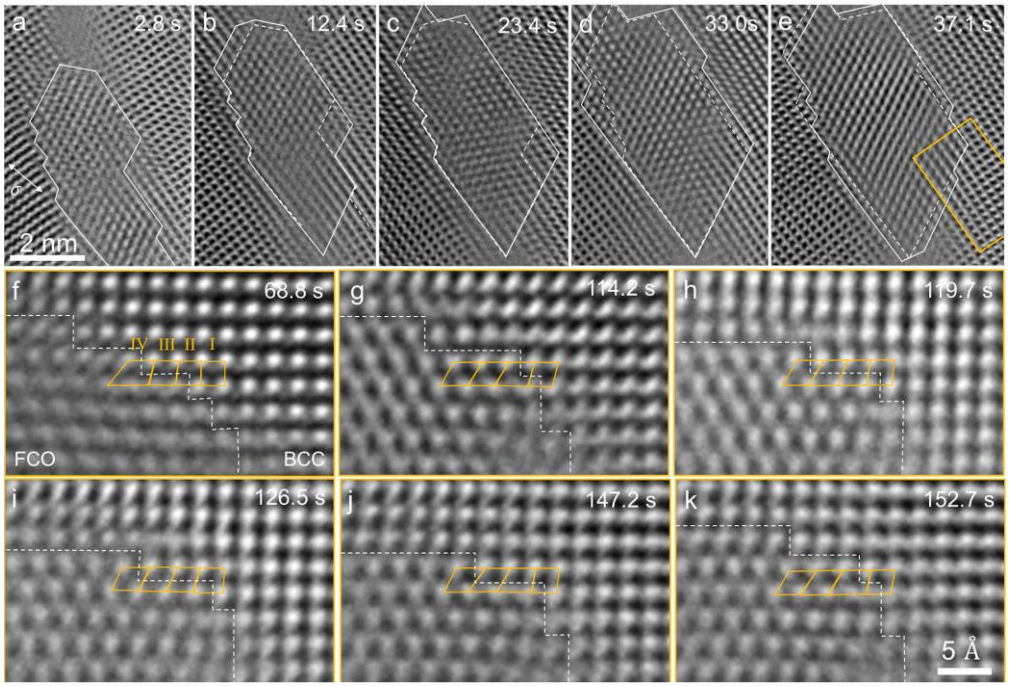

Figure 17 – Visualization of FCO phase growth. Distinct boundaries track the grain's evolution from a slender FCO phase to its expansion under stress. Atomic-scale HRTEM images detail the BCC to FCO transition, highlighting challenges like lattice mismatch and stress variations. Post-fracture stability in the FCO phase is observed, with no reversible atomic shifts. Courtesy of Lu et al. [113].

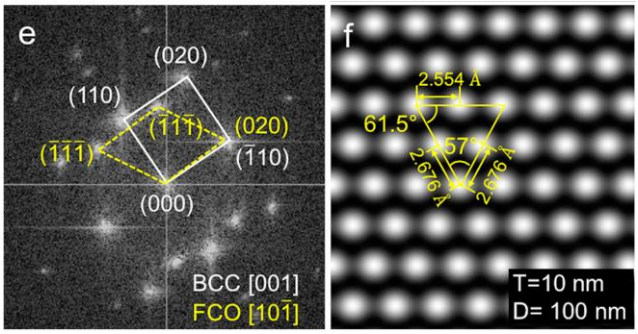

Figure 18 – FFT image of a grain depicting both BCC and FCO lattices. A simulated HRTEM view confirms the observed structural transformation in the metal. Courtesy of Lu et al. [113].

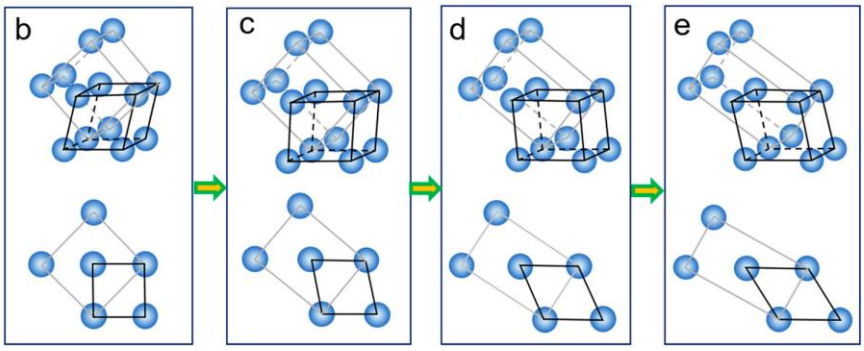

Figure 19 – Atomic models representing the BCC to FCO transition. Both 3D and 2D models emphasize the original BCC cells and subsequent lattice changes. The transformation process, including shearing and shuffling, offers insights into the structural evolution of Mo. Courtesy of Lu et al. [113].

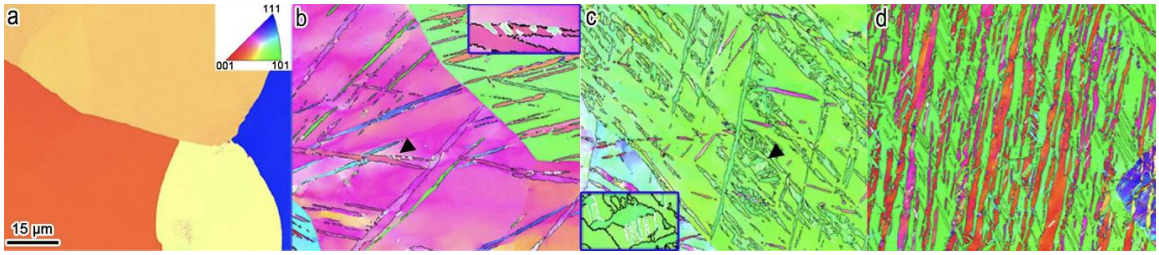

Figure 20 – Inverse pole figure color map overlapped with twin boundaries in α-Fe, both before (a) and after (b, c, d) shock-loading. Post shock-loading, numerous twin lamellae emerge, predominantly {112}<111> twins marked by black lines, while {332}<113> twins, indicated by white lines, appear sparingly. The colors denote crystallographic orientations normal to the observation plane, as shown in the stereographic triangle in (a). Insets in (b, c) provide magnified views of areas highlighted by arrows, illustrating detailed changes. Courtesy of Wang et al. [104].

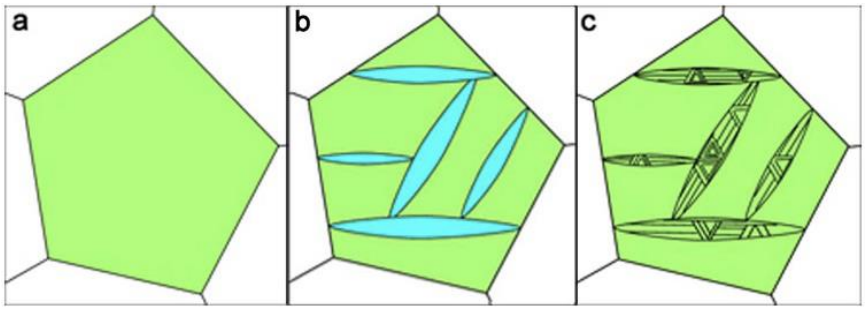

Figure 21 – Schematic representation of the α→ε→α phase transformations. (a) Depicts the initial α-grain. (b) Illustrates the α→ε phase transition induced by shock loading, resulting in the formation of needle-like ε regions. (c) Shows the ε→α reverse transition occurring within the ε-needles after unloading. The α-phase is represented by green, while the ε-phase is depicted in blue. Black lines delineate the boundaries of the microstructural features. Courtesy of Wang et al. [104].

Another key topic to underscore is that HE is anisotropic as its degree depends on crystallographic directions [118]–[125]. In BCC iron, for example, hydrogen reduces the cleavage stress in {100} planes [123] while, at the same time, GBs around {100} are more susceptible to be enriched in hydrogen atoms [124]. Also in BCC iron, under shock compression, hydrogen atoms prevent the phase transition in the [100] direction, enhancing spall strength at high strain rate, while promoting dislocation emission in the [111] direction, accelerating dislocation mediated growth of voids and thus lowering spall strength [125]. Furthermore, the effect of hydrogen in metals can influence the plastic anisotropy, increasing or decreasing the activation energy of slip systems [119]. Processes like cold drawing or additive manufacturing can introduce or amplify anisotropy, altering the

susceptibility of a metal to HE [120]–[122]. This anisotropic behavior is not simply a detail, but an important aspect in predicting and mitigating the detrimental effects of HE in steels and other metals. Therefore, it will receive emphasis in this thesis research.

HE stands as a multifaceted phenomenon that challenges researchers in both its complexity and intricacies. The literature mainly emphasizes mechanisms such as HELP, HESIV, and HEDE, yet the understanding and simulation of these mechanisms pose their own set of challenges. Within the realm of MD simulations, current potentials for Fe-H and Fe-C-H systems permit the observation of changes in mechanical properties. However, simulations face constraints that impede alignment with experimental results, such as exceedingly high strain rates or extremely short simulation times, which are necessary due to limited computational resources. These limitations can affect critical aspects like hydrogen diffusion and the visibility of certain HE mechanisms, like HELP. Additionally, the influence of boundary conditions during simulation further complicates matters. Despite these challenges, mechanisms like HESIV and HEDE do become discernible, as HELP favors lower strain rates [28], [72]. In the pursuit of advancing the understanding, this thesis will document changes in mechanical properties as observed in the simulations, laying a foundation upon which future steps can take place. As this discussion progresses into the following sections, the focus will shift deeper into the methodologies, results, and potential contributions this work may offer to the broader field of study.

This literature review, while not exhaustive, underscores the objective to go into more complex models and document the outcomes. It highlights a promising avenue for exploration through MD simulations on Fe-C and Fe-C-H systems and aims to contribute a piece to the complex puzzle of HE in steels.

2.2 Fundamental Principles of Molecular Dynamics Simulations

The information for this subsection is extracted and paraphrased from Chapter 1 "Introduction to Molecular Dynamics" found in the book "Lecture Notes in Physics" [126].

MD can be defined as the science of simulating the time dependent behavior of a system of particles. The evolution of the set of interacting atoms over time is performed by integrating their equation of motion with boundary conditions appropriate for the geometry or symmetry of the system. MD, in order to calculate the microscopic behavior of a system from the laws of classical mechanics, requires a description of the interaction potential (or force field) between the atoms as an input. As such, the quality of the results of an MD simulation depends directly on the accuracy of the description of inter-particle interaction potential. The choice of the potential depends directly on the application. As such, MD acts as a computational microscope. This microscopic information is later converted to macroscopic, observable information, like pressure, temperature, heat capacity, stress tensor, etc., using statistical mechanics. MD techniques have seen extensive use in almost all the branches of science. For example, in the determination of reaction rates in chemistry, solid state structures, surfaces and defects formation in material science, protein folding in biochemistry, along with others.

The fundamental elements for an MD simulation are (i) the interaction potential (i.e., potential energy) for the particles, from which the forces can be calculated and (ii) the equations of motion governing the dynamics. The laws of classical mechanics are followed, mainly Newton's law

$$F_i = m_i a_i \ , \tag{1. 1}$$

in which i each atom in a system composed of N atoms, m_i is the mass of the atom, a_i its acceleration and F_i the force acting upon it as a result of the interactions with the other atoms. One can alternatively solve the classical Hamiltonian equation of motion

$$\dot{p}_i = -\frac{\partial H}{\partial r_i}, \tag{1. 2}$$

$$\dot{r}_i = \frac{\partial H}{\partial p_i}, \tag{1. 3}$$

where p_i and r_i are the momentum and position co-ordinates for the i^{th} atom. The Hamiltonian, H, is defined as a function of position and momenta, given by

$$H(p_i, r_i) = \sum_{i=1}^{N} \frac{p_i^2}{2m_i} + V(r_i) . \tag{1. 4}$$

The force applied on an atom can be calculated as the derivative of the energy with respect to the change in the position of the atom

$$F_i = m_i a_i = -\nabla_i V = \frac{dE}{dr_i} . \tag{1. 5}$$

By using knowledge of the atomic forces and masses, one can calculate the positions of each atom through a series of extremely small time steps, typically in the order of femtoseconds. Parting from the accelerations, the velocities are calculated

$$a_i = \frac{dv_i}{dt} . \tag{1. 6}$$

Lastly, the positions are calculated from the velocities

$$v_i = \frac{dr_i}{dt} . \tag{1. 7}$$

To sum up the procedure, at each step, the forces on the atoms are computed and combined with the current positions and velocities to generate new positions and velocities a short time step ahead. The force acting on each atom at each interval is assumed to be constant. After the short time step, the atoms are then moved to the new positions, the updated set of forces is computed from these new positions and the cycle goes on and on until the number of the predetermined steps is reached. As simulations with a macroscopic number of atoms or molecules (around 10^{23}) is impossible to handle with MD, it is necessary to use statistical mechanics to extract the macroscopic information from the microscopic information provided by the MD simulation.

It is important to note two major properties of the equations of motion. Firstly, they exhibit time-reversal symmetry, which means they take the same form when the transformation from *t* to -*t* is made. This symmetry implies that microscopic physics is independent of the direction of the flow of time, making MD a deterministic technique. Given an initial set of position and velocities, the subsequent time evolution is entirely determined from its current state. Secondly, the equations of motion conserve the Hamiltonian, which is equivalent to the conservation of the total energy of the system. This can be straightforwardly observed by computing the time derivative of H (Hamiltonian) and substituting equations (1.2) and (1.3) for the time derivatives of position and momentum.

$$\frac{dH}{dt} = \sum_{i=1}^{N} \left[\frac{\partial H}{\partial r_i} \dot{r}_i + \frac{\partial H}{\partial p_i} \dot{p}_i \right] = \sum_{i=1}^{N} \left[\frac{\partial H}{\partial r_i} \frac{\partial H}{\partial p_i} - \frac{\partial H}{\partial p_i} \frac{\partial H}{\partial r_i} \right] = 0 \ . \qquad (1.8)$$

This provides an important link between MD and statistical mechanics.

Statistical mechanics allows us to connect the microscopic details of a system to macroscopic properties using the Gibbs ensemble concept. This concept is based on the idea that many individual microscopic configurations of a large system can lead to the same macroscopic

properties, which means that there is no need to know the precise motion of every particle in order to predict the properties of the system. Instead, simply averaging over a large number of identical systems, each in a different microscopic configuration, is sufficient. This approach characterizes microscopic observables in terms of ensemble averages, which can be determined by fixed values of thermodynamic variables like energy (E), temperature (T), pressure (P), volume (V), particle number (N) or chemical potential (μ). One of the fundamental ensembles is the micro-canonical ensemble (NVE), which is characterized by constant particle number (N), constant volume (V) and constant energy (E). Other examples include the canonical or NVT ensemble, with constant particle number (N), constant volume (V) and constant temperature (T); the isothermal-isobaric or NPT ensemble, with constant particle number (N), constant pressure (P) and constant temperature (T); and the grand-canonical or μVT ensemble, with constant chemical potential (μ), constant volume (V) and constant temperature (T). These variables can be viewed as experimental control parameters that specify the conditions under which an experiment is performed.

The computational power required to run an MD simulation can often be limiting. The length of the simulation time is directly dependent on the duration of each time step, during which forces are calculated. It is crucial to choose a small enough time step to avoid discretization errors, while at the same time selecting a sufficiently large number of time steps (and thus simulation time) to model the desired effect accurately. The simulation length should be large enough that the system goes through all possible phase space points in the ensemble, but not so large that it takes an extraordinary amount of time, for instance, less than the vibrational frequency of the system. A good guideline is that the atoms should not move more than 1/20 of the nearest neighbor distance in the chosen time step. Specific processes occur over a wide range of time scales, including bond vibrations (femtoseconds), collective vibrations (picoseconds) and protein folding (milliseconds

to microseconds), and these time scales need to be captured in the simulation. The integration time step is determined by the fastest varying force and is of the order of femtoseconds, which limits the accessible time scale of MD simulations from picoseconds to nanoseconds. As a result of this limitation, and no matter how powerful a computer is, slower mechanisms such as diffusion are challenging to model using MD simulations, and this requires the use of multiscale models.

As a final note, the general procedure for MD simulations can be defined in the next 5 steps (as depicted in Figure 22):

1. Initial atoms positions and velocity at the start ($t = 0$).
2. Calculation of the interaction energy between atoms based on the potential file.
3. Calculation of the force between atoms.
4. Calculation of the acceleration, based on previously calculated force and mass of the atoms. Velocity per atom is then calculated after the selected time step (dt).
5. Recalculation of the interaction energy between atoms at new positions and velocities ($t + dt$).

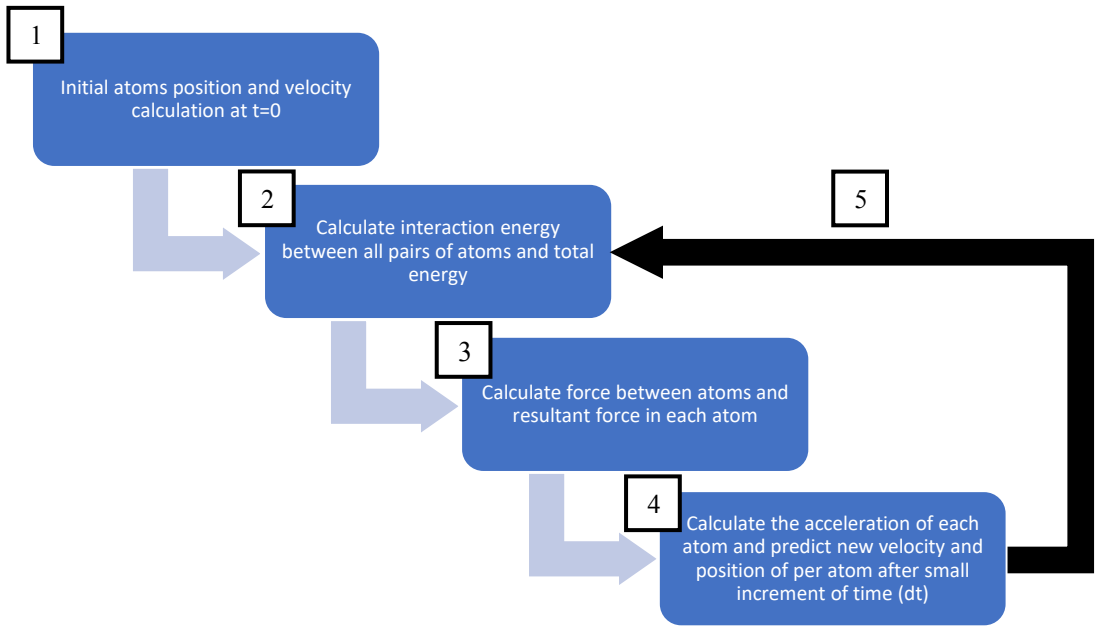

Figure 22 – General and basic procedure of MD simulations.

2.3 Employed Interatomic Potentials

2.3.1 Bond Order Potential

A bond order potential (BOP) is an advanced interatomic potential that goes beyond conventional pair potentials by accounting for the directional nature of chemical bonding and multicenter interactions in materials [127], [128]. Unlike pair potentials, which consider only pairwise interactions between atoms, BOPs provide a more accurate description of the complex bonding environment in materials, making them suitable for simulating materials with different bonding configurations and coordination numbers.

The foundation of BOPs lies in the tight-binding formalism, a semi-empirical quantum mechanical method that strikes a balance between computational efficiency and accurate representation of electronic structures [129]. By incorporating tight-binding concepts, BOPs are able to capture the dependence of bond strength on the local atomic environment, making them particularly useful for simulating materials that undergo structural transformations or exhibit diverse bonding environments.

In the context of MD simulations, BOPs offer several advantages over traditional pair potentials. First, the ability of BOPs to describe directional bonding allows for more accurate simulations of materials that exhibit anisotropic properties or undergo phase transformations [128]. Second, BOPs account for multicenter interactions that are essential for understanding the structural, electronic, and mechanical properties of materials [127]. Finally, BOPs are often more transferable across materials and conditions without extensive parameter tuning [129], which can save time and effort when simulating materials systems. Using BOPs in MD simulations, researchers can gain valuable insight into phenomena such as phase transformations and GB behavior, and

mechanical properties of a wide range of materials, including metals, semiconductors, and insulators.

Zhou et al. [92] carried out a comprehensive review of the literature on different interatomic potentials with the express purpose of constructing a tripartite potential from existing binary potentials, resulting in two distinctive Fe-C-H ternary potentials capable of accurately representing the influences of hydrogen on various deformation properties and mechanisms across a range of Fe-C steel microstructural variations which include FCC austenite (γ-Fe), BCC ferrite (α-Fe), and orthorhombic Fe_3C cementite. These phases can manifest in a variety of morphologies and combinations such as martensite, bainite, and pearlite. The constructed potentials demonstrate a robust ability to represent these intricate microstructural features. This is achieved through stable MD simulations of systems containing all three integral phases (FCC, BCC, and Fe_3C) together with FCC to BCC phase transformation. Researchers also predict that the two BOPs have the ability to effectively simulate the effect of hydrogen on the deformation behavior in Fe-C steels. These potentials have the critical ability to simulate the complex α-γ-δ phase transformation of iron, which is an integral feature of many Fe-C steels. Additionally, their capability to effectively represent iron carbides has been very promising, which has been a challenge in the past [92], [130].

2.3.2 Modified Embedded Atom Method Potential

The Modified Embedded Atom Method (MEAM) is a type of interatomic potential that has been developed to improve the accuracy and transferability of MD simulations, particularly for metallic systems [131]. The MEAM builds upon the original Embedded Atom Method (EAM) by incorporating angular forces, which allow it to better represent the behavior of materials under a variety of conditions, including those that involve complex bonding environments or crystal structures [132]. In MEAM, as its approach is grounded on the DFT, the energy of an atom is

described as a function of the electron density around the atom, which is determined by the positions of its neighboring atoms. This provides a more accurate description of atomic interactions than pair potentials, which only consider the distance between two atoms.

In the context of MD simulations, MEAM potentials offer several advantages. First, by including angular forces, MEAM potentials can accurately describe the directional nature of bonds in materials, which is crucial for simulating materials with complex bonding configurations or that undergo phase transformations [131]. Second, MEAM potentials are also transferable across different materials and conditions, making them highly versatile for a wide range of simulations [132]. By using MEAM potentials in MD simulations, researchers can gain valuable insights into a variety of materials behaviors, including mechanical properties, phase transitions, and defect dynamics.

Mun et al. [93] aimed to create a MEAM potential for the Fe-C-H. To develop this potential for the ternary Fe-C-H system, the authors first reviewed and analyzed existing potentials for single elements (Fe, C, and H) and binary systems (Fe-C, Fe-H, and C-H). Then, modifications were made to these potentials to better describe the interactions in the ternary Fe-C-H system. The modifications include, but are not limited to, adjusting parameters related to the strength of the atomic bond, the screening function, and the equilibrium atomic distance.

After developing the new potential, its performance was validated by comparing its predictions with results from other potentials (ReaxFF and BOP), experimental data, and first-principles calculations. This comparison included various properties such as phase stability, lattice constants, and elastic constants. It was concluded that this new Fe-C-H MEAM potential successfully reproduces the experimental and first-principles results for the various properties considered. This potential can be used in atomistic simulations to study the influence of hydrogen and carbon on

the mechanical and physical properties of iron-based materials. It can also serve as a valuable tool for understanding HE, carbon solubility, and related phenomena in steel and other iron-based alloys. Therefore, MEAM will be used in the current research as will be detailed in the following chapters.

Chapter 3: Methodology

This section outlines the processes for model creation, details model specifications, and offers an overview of simulation procedures and general information regarding the successive steps within each simulation. At the end of this chapter, two detailed tables outline the characteristics of each executed model, which include the crystal direction or GB types, the number of atoms per type, the type of potential employed, the type of loading (strain rate or velocity rate), the results reported and how these are grouped (in cases, i.e., Case 1, 2, 3 and 4).

3.1 General Procedure

The basic procedure to perform the simulations is:

1. Creation of the atomic model:
    a. Construction of the basic Fe-C cell, with carbon at the octahedral sites.
    b. The basic Fe-C cell is multiplied to obtain the desired dimensions (the bicrystalline and polycrystalline models make use of Voronoi tessellation, explained later). If reorientation is required, it is first reoriented and then expanded.
    c. Random removal of carbon atoms to obtain the desired concentration (0.45 wt. %).
    d. Hydrogen atoms are added to randomized tetrahedral sites in specified concentrations, which will be detailed later.
2. Import and run of atomic model into MD software:
    a. Minimization (Molecular Statics - MS) and equilibration (MD) at desired temperature are performed as the first steps.
    b. Loading of the atomic model (either in the form of strain rate or velocity rate, depending on the boundary conditions).

c. Post-processing of the results to obtain information such as the stress-strain response, changes in the phase distribution, variations in the dislocation density, and vacancy formation, all compared to increasing strain. This involves using the output data from MD software to make plots, calculations, visualization, etc. All results are compared between the Fe-C system and Fe-C-H systems with varying hydrogen concentration.

All atomic models were created using Atomsk [133], [134] which is a command-line program to create, manipulate and convert data files for atomic-scale simulations. The MD simulations were carried out using Large-scale Atomic/Molecular Massively Parallel Simulator (LAMMPS) MD software [135] developed by Sandia National Laboratories. Results from the simulation are mainly post-processed in OVITO [136] (results visualization and data extraction), MATLAB [137] and Python [138] (the last two are mainly for data extraction, calculations, and plot generation).

Having outlined the procedure for performing the simulations, a detailed examination of the types of results is given next:

(1) The stress-strain response: the stress is extracted directly from the component of the pressure tensor in the Y direction and compared to the increasing strain.

(2) Changes in the phase distribution with strain (BCC, FCC, HCP, and non-standard structures): measured using the Common Neighbor Analysis (CNA) tool [139] in OVITO. Prior to loading, the primary phase composition is largely Body-Centered Cubic (BCC) with the remainder classified as "Other". This classification is due to the presence of interstitial atoms (both carbon and hydrogen) that perturb the original BCC configuration, causing OVITO to label these perturbations under the "Other" category. As the carbon content remains constant, an increase in

hydrogen concentration increases the amount of non-standard phases and decreases the presence of the BCC phases prior to loading.

(3) Variations in the dislocation density with strain (measured in both count/nm^3 and nm/nm^3): the Dislocation Extraction Algorithm (DXA) tool [140], [141] in OVITO is used to extract dislocation data from each system. This tool identifies all defects present in the crystal, determines the Burgers vectors, and then generates a line representation of the dislocations. Each dislocation representation consists of a start and end point, both of which define the orientation of the dislocation line, which can connect with other dislocation lines to form a node. The color of the dislocation line indicates the type of dislocation: for example, green represents 1/2 <111> dislocations (which make up the vast majority of the types shown) and pink represents <100> dislocations.

(4) The progression of the number of vacancies as a function of strain: the Wigner-Seitz defect analysis tool [142] in OVITO is employed to monitor the progression of vacancies throughout the deformation of the system. In a general sense, it operates by contrasting each deformed state of the system against the sites defined in the initial reference state (prior to loading). When there is a variation in atom count at any site (meaning either an increase or decrease in atoms), a defect is identified. A site becomes labeled as a vacancy when it no longer contains any atom.

The following sections delve into the details of each of the atomic models: single-crystalline, bicrystalline and polycrystalline.

3.2 Single-Crystalline Models

The basic single-crystalline model is composed of iron atoms in BCC phase and the corresponding number of carbon atoms to reach the desired concentration of 0.45 wt. %. The orientations selected

for these models are X [$\bar{1}10$] Y [111] Z [$11\bar{2}$] for Orientation I, X [$1\bar{1}0$] Y [110] Z [001] for Orientation II, and X [010] Y [100] Z [001] for Orientation III. The simulation box dimensions vary between orientations, but not much. The schematic of the atomic models for Orientation I, II, and III are shown in Figure 23. In the basic Fe-C systems, hydrogen atoms are added randomly at tetrahedral interstitial sites to obtain the desired concentration of 1, 3, 5 and 8 at. %. For the equilibration phase, the boundary conditions are kept periodic in each axis, meaning that particles can interact across the boundary, and any atom that crosses the boundary re-enters on the other end [143]. Also, these boundary conditions result in a more bulk-like behavior of the system. Molecular statics (MS) simulation is run to minimize the system energy and avoid any possible atom overlap prior to applying strain to the system. Conjugate gradient (CG) algorithm is used for energy minimization [144]. Afterwards, the system is kept running for several ps without any external loading at 300 K in order to stabilize the atoms. The Nose-Hoover barostat and thermostat (NPT) isothermal-isobaric ensemble [145] is used to stabilize the system temperature and pressure, the latter as close to 0 bar as possible. In the final stage (the loading stage), two different sets of boundary conditions are used (the results for both sets are grouped under Case 1 and 2, respectively): for the first set, all axes maintain periodic boundary conditions, with a strain rate of 6.7 x 10^8 s^{-1} applied to the longitudinal axis (Y-axis) over 1.5 ns, culminating in a total strain of 1.005. In contrast, the second set has periodic conditions on the X and Z axes, while using a shrink-wrapped boundary on the Y axis, causing the box to lose periodicity in that direction and preventing atomic interactions across the boundary. Given the inability to directly apply a strain rate under non-periodic conditions, a velocity is instead imposed on a selected group of atoms in the top and bottom of the model. This velocity, when divided by the initial length of the model, results in an equivalent strain rate. For this batch of simulations, the intended strain rate is 1x10^9

s^{-1}, resulting in variable velocities across the models to match the desired strain rate. The canonical (NVT) ensemble is used for these simulations [146]. The purpose of comparing these two boundary conditions is to observe differences in the stress-strain behavior, as fully periodic conditions could significantly delay a potential fracture (enabling the extreme elongation achieved), while shrink-wrapped conditions could precipitate the fracture much earlier. As a result, for Case 1, results are considered valid up to a fraction of the total strain of 1.005, varying with each orientation. On the other hand, for Case 2, simulations are run until fracture occurred without all reaching necessarily the same strain level. Specifically, for this second scenario, only the basic Fe-C system and the Fe-C-H system, with a hydrogen concentration of 3 and 8 at. %, are run. Table 4 includes the details for the single-crystalline systems.

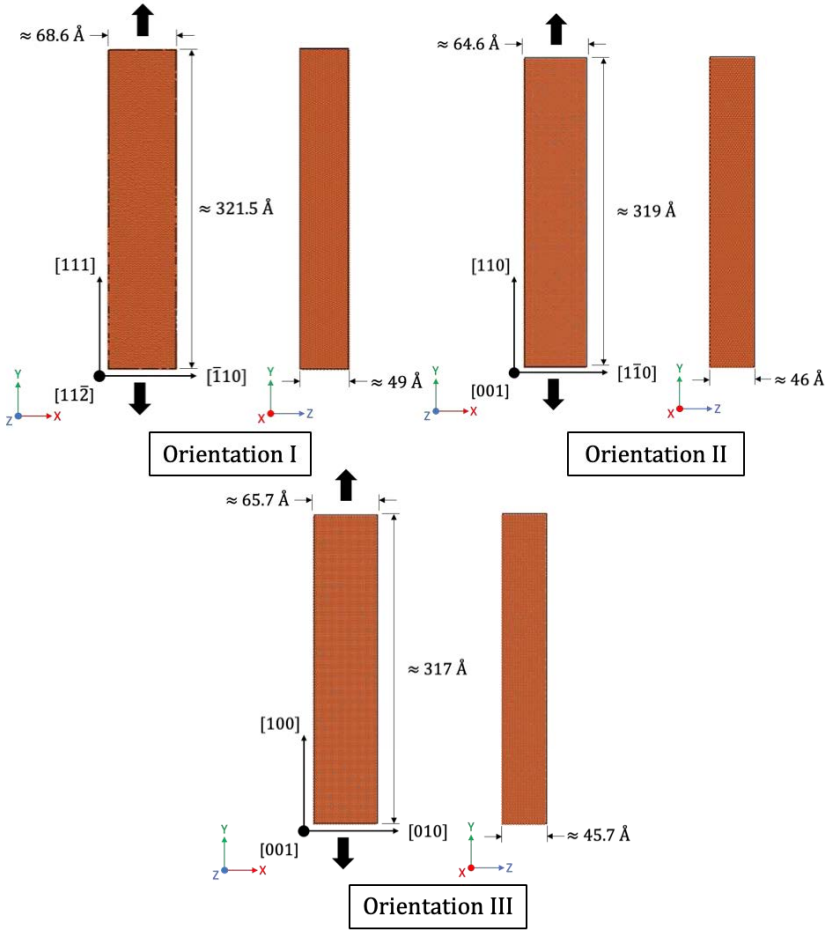

Figure 23 – Schematic of each orientation. The black arrows indicate the loading direction.

3.3 Bicrystalline Models

The construction of the bicrystalline model is more complex because the Voronoi tessellation method [147]–[151] must be used to generate the grains. In a general sense, a Voronoi tessellation is constructed by generating a set of distinct points within a defined space, such as a two-dimensional plane. For each given point within this set, a unique region is delineated that contains all locations within the plane that are closer to that particular point than any other. These regions form individual cells associated with each point. The cumulative ensemble of these cells, spanning the entire underlying space, constitutes the Voronoi tessellation. Figure 24 shows the general steps to create a bicrystalline model.

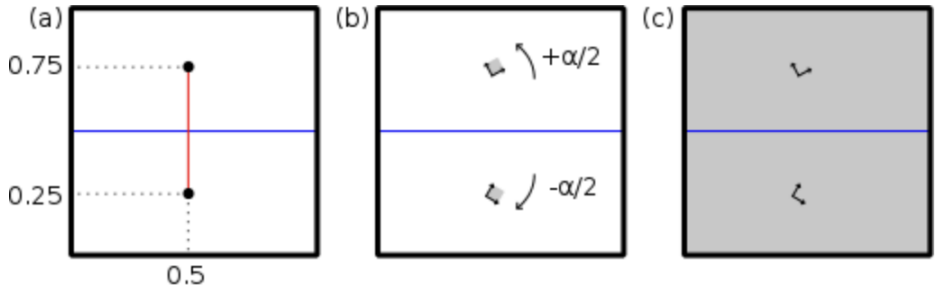

Figure 24 – Creation for a bicrystalline model using Voronoi tessellation: (a) Nodes (black dots) are introduced at given positions inside the simulation box. (b) Atomic "seeds" (for instance unit cells) are placed at the positions of the nodes, with the given crystal orientation. (c) Both seeds are expanded and each cut at the GB. Courtesy of Atomsk [147].

The bicrystalline models represent a Σ3<110>[112] and Σ5<100>[210] GBs, with the resultant Fe-C systems visualized in Figure 25. Although the models exist in three dimensions, the grains traverse the full thickness extent of the model. This configuration essentially creates a two-dimensional model that is extruded to a certain thickness, effectively providing a three-dimensional representation. Carbon concentration (at 0.45 wt. %) is controlled in the same way as in the single-crystalline models. Hydrogen concentrations of 100, 150 and 200 wt. ppm are applied, primarily around and at the GB. The strain rate applied is 1 x 10^9 s^{-1} and the simulation follows

the same steps as those implemented in the single-crystalline model using a shrink-wrapped boundary on the Y axis. The results for bicrystalline simulations are grouped under Case 3.

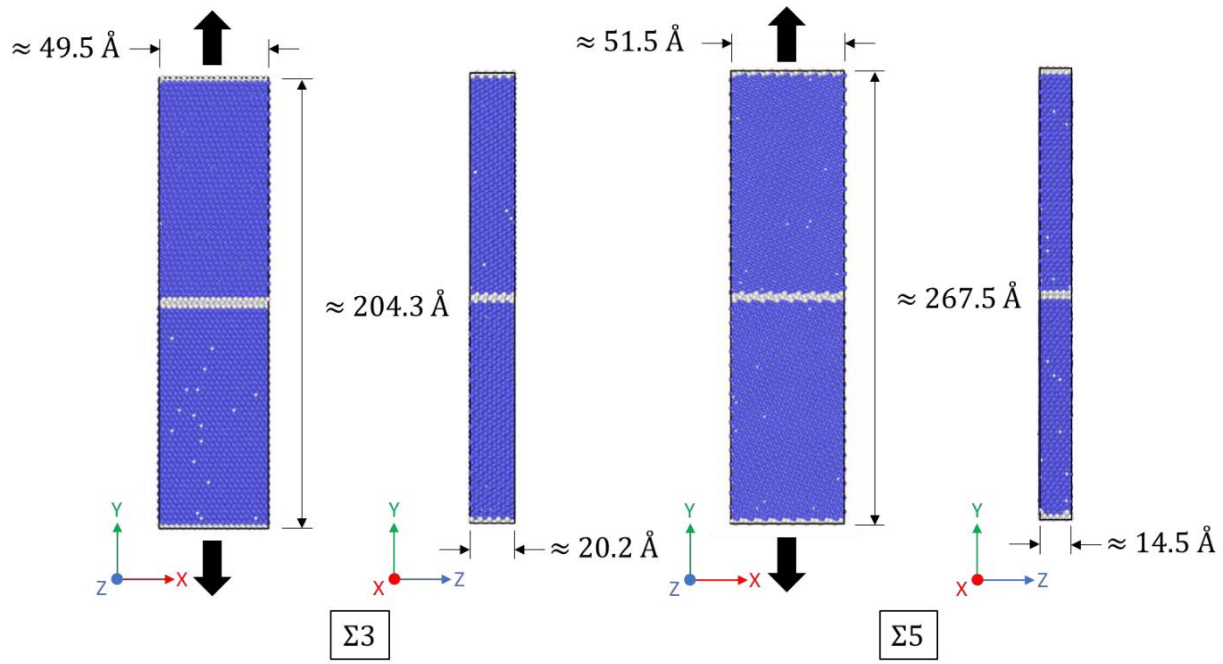

Figure 25 – Bicrystalline models used. Blue represents BCC iron, lines of white as GBs (except on the top and bottom, as they represent the surface) and white spots, distributed along all the BCC iron structure, as carbon atoms. The black arrows indicate the loading direction.

3.3 Polycrystalline Model

The polycrystalline model is also created by taking advantage of the Voronoi tessellation. The process, shown in Figure 26, is close to the creation of a bicrystalline model, just expanded to allow for additional grains. Even though the steps shown correspond to the formation of a 2D polycrystalline model, the same steps can be extended to create a 3D model. As in the bicrystalline models, the grains on this model are extruded to a specified thickness, achieving a three-dimensional representation. Carbon concentration (at 0.45 wt. %) is controlled the same way as in the single-crystalline and bicrystalline models. The resultant system can be visualized in Figure 27. Hydrogen concentrations of 100, 150 and 200 wt. ppm are applied, and distributed in various locations: (a) at the GBs, (b) at the interior of grains and (c) randomized (this location only for a

concentration of 100 wt. ppm). The three cases are shown in Figure 28. Please note that the radius of the hydrogen atoms is increased to almost 5 times just for visualization purposes. The strain rate applied is 1 x 10^9 s^{-1} and the simulation follows the same steps as those implemented in the bicrystalline model. Table 5 includes the details for the bicrystalline and polycrystalline systems. The results for the polycrystalline simulations are grouped under Case 4.

As mentioned before, the interatomic potential files used for all simulations were (1) a ternary Fe-C-H BOP, specifically the BOP I, developed by Zhou et al. [92] at Sandia National Laboratories; and (2) a ternary Fe-C-H MEAM potential developed by Mun et al. [93] at Mississippi State University.

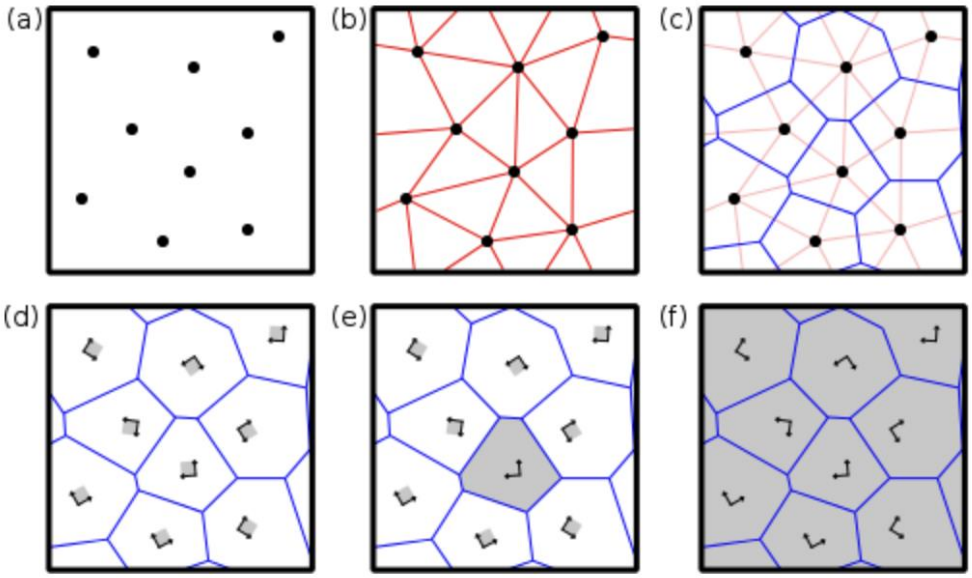

Figure 26 – Steps to form a polycrystalline model using Voronoi tessellation: (a) Nodes (black dots) are introduced at given positions inside the simulation box. (b) Nodes are linked with their neighbors (red lines). Periodic boundary conditions are used. (c) The normal to the red lines are found (blue lines). These blue lines define the contours of the future grains, i.e., the GBs. (d) Atomic seeds (for instance unit cells, as mentioned before) are placed at the positions of the nodes, with the given crystal orientation. (e) A seed is expanded in the three directions of space. Atoms that are outside of the grain are removed. (f) After all seeds have been expanded and cut inside their respective grains, one obtains the final polycrystalline model. This illustrates the generation of Voronoi polycrystal in 2-D, but can be generalized to the 3-D case. Courtesy of Atomsk [148].

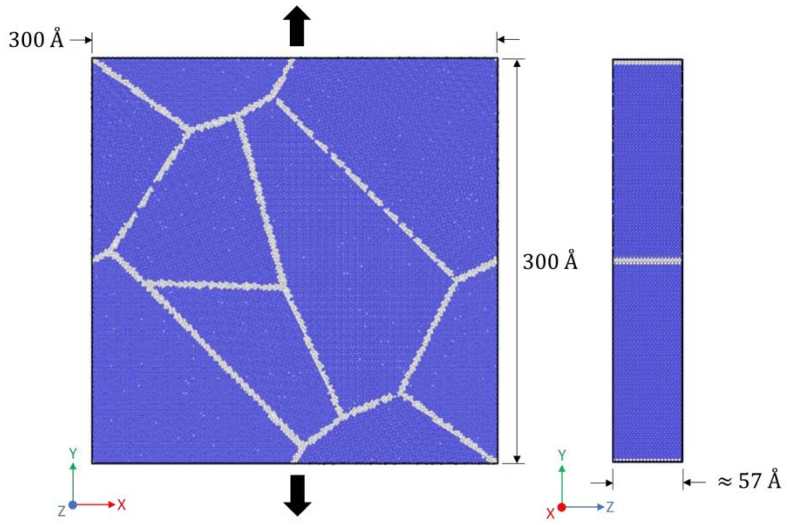

Figure 27 – Polycrystalline model used. Blue represents BCC iron, lines of white as GBs and white spots, distributed along all the BCC iron structure, as carbon atoms. The black arrows indicate the loading direction.

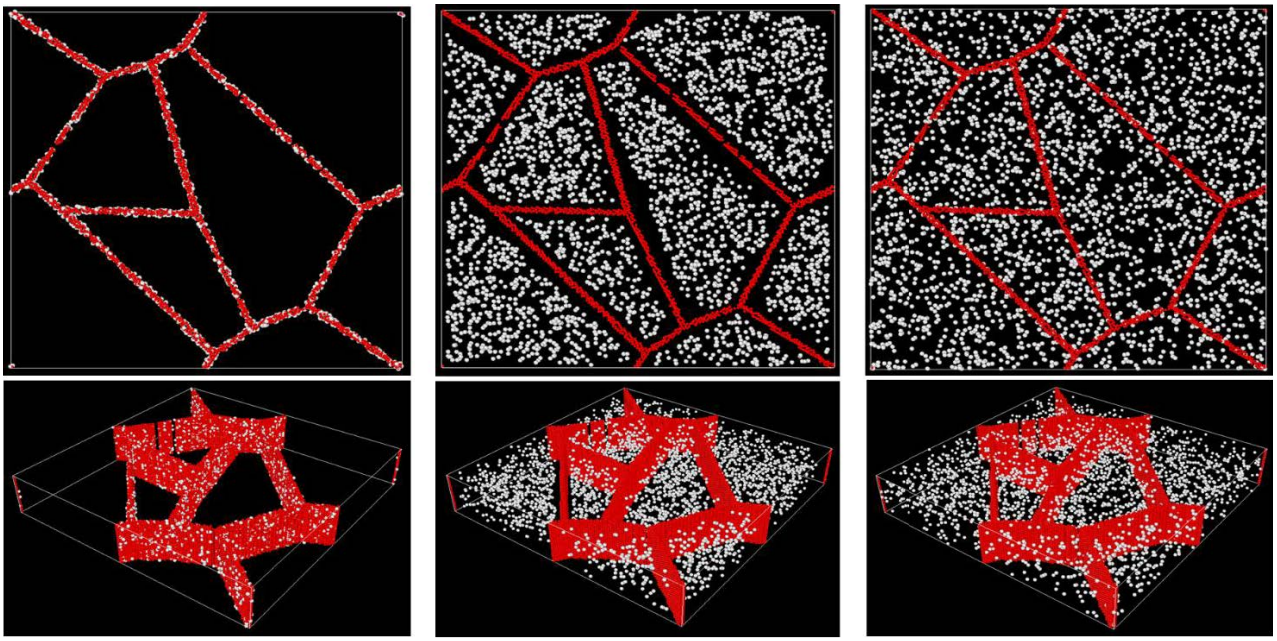

Figure 28 – Hydrogen distribution in the Fe-C-H systems: (a) at GBs, (b) at grain interior and (c) randomized.

Table 4 – Description of the single-crystalline simulation models run and results reported in this study.

Crystal Structure	Direction (Y)	Fe Atoms	C Atoms (0.45 wt.%)	H Atoms	System	Potential	Load Type	Result Type	Case (Results Grouping)
SC	[111] Orientation I	92820	1951	0	Fe-C	BOP & MEAM	SR	SSR VC PD DD	1
				938	Fe-C-H, 1 at.% H				
				2871	Fe-C-H, 3 at.% H				
				4885	Fe-C-H, 5 at.% H				
				8071	Fe-C-H, 8 at.% H				
	[110] Orientation II	80896	1717	0	Fe-C				
				817	Fe-C-H, 1 at.% H				
				2502	Fe-C-H, 3 at.% H				
				4258	Fe-C-H, 5 at.% H				
				7034	Fe-C-H, 8 at.% H				
	[100] Orientation III	81696	1717	0	Fe-C				
				825	Fe-C-H, 1 at.% H				
				2527	Fe-C-H, 3 at.% H				
				4300	Fe-C-H, 5 at.% H				
				7104	Fe-C-H, 8 at.% H				
	[111] Orientation I	92820	1951	0	Fe-C		VR		2
				2871	Fe-C-H, 3 at.% H				
				8071	Fe-C-H, 8 at.% H				
	[110] Orientation II	80896	1717	0	Fe-C				
				2502	Fe-C-H, 3 at.% H				
				7034	Fe-C-H, 8 at.% H				
	[100] Orientation III	81696	1717	0	Fe-C				
				2527	Fe-C-H, 3 at.% H				
				7104	Fe-C-H, 8 at.% H				

SC = Single-crystalline, BC = Bicrystalline, PC = Polycrystalline, SR = Strain Rate, VR = Velocity Rate,
SSR = Stress-Strain Response, PD = Phase Distribution, VC = Vacancy Count, DD = Dislocation Density

Table 5 – Description of the bicrystalline and polycrystalline simulation models run and results reported in this study.

Crystal Structure	Grain Boundary	Fe Atoms	C Atoms (0.45 wt.%)	H Atoms	System	Potential	Load Type	Result Type	Case (Results Grouping)
BC	Σ5<100>[210]	12800	269	0	Fe-C	BOP & MEAM	VR	SSR VC PD	3
				71	Fe-C-H, 100 wt.ppm H at Grain Boundary				
				107	Fe-C-H, 150 wt.ppm H at Grain Boundary				
				143	Fe-C-H, 200 wt.ppm H at Grain Boundary				
	Σ3<110>[112]	17615	355	0	Fe-C				
				98	Fe-C-H, 100 wt.ppm H at Grain Boundary				
				147	Fe-C-H, 150 wt.ppm H at Grain Boundary				
				196	Fe-C-H, 200 wt.ppm H at Grain Boundary				
PC	Random	534200	11227	0	Fe-C	BOP			4
				2974	Fe-C-H, 100 wt.ppm H at Grain Boundaries				
					Fe-C-H, 100 wt.ppm H at Grains' Interior				
					Fe-C-H, 100 wt.ppm H Randomized				
				0	Fe-C	MEAM		SSR VC PD DD	
				2974	Fe-C-H, 100 wt.ppm H at Grain Boundaries				
					Fe-C-H, 100 wt.ppm H at Interior of Grains				
					Fe-C-H, 100 wt.ppm H Randomized				
				0	Fe-C				
				3464	Fe-C-H, 150 wt.ppm H at Grain Boundaries				
					Fe-C-H, 150 wt.ppm H at Grains' Interior				
					Fe-C-H, 150 wt.ppm H Randomized				
				0	Fe-C				
				5949	Fe-C-H, 200 wt.ppm H at Grain Boundaries				
					Fe-C-H, 200 wt.ppm H at Grains' Interior				
					Fe-C-H, 200 wt.ppm H Randomized				

SC = Single-crystalline, BC = Bicrystalline, PC = Polycrystalline, SR = Strain Rate, VR = Velocity Rate,
SSR = Stress-Strain Response, PD = Phase Distribution, VC = Vacancy Count, DD = Dislocation Density

Chapter 4: Results and Discussion

For each system, the stress-strain response is reported first, then followed by dislocation density in response to increasing strain, the variation in phase distribution (or vice versa), and the shift in vacancy count with increasing strain, in an effort to explain the behavior in the stress-strain response. Specifically, the explanation for the stress-strain response is dissected into two parts: right when the system yields, and the plastic region. While connections to the literature review will be drawn where most appropriate, repetition will be minimized since many results echo previously discussed findings. Consequently, the connection is highlighted only in the most relevant results. Detailed explanations are given in the following sections.

4.1 Case 1: Single-Crystalline with Periodic Boundary Condition in All Axes

4.1.1 Bond Order Potential

Figure 29 shows the stress-strain response for all orientations, while Table 6 shows a comparison between the peak stress and the corresponding strain for all the Fe-C-H systems relative to the Fe-C system in all orientations. Figure 30 shows snapshots of the systems at the same strain (post-yield) of all orientations. A general trend is observed, where the addition of hydrogen lowers the peak stress obtained and the strain corresponding to each respective peak stress. Also, as shown in the stress-strain plots and Table 6, the corresponding effect of hydrogen significantly varies between orientations (having a major impact on the peak stress obtained in Orientation II and III), which suggests that anisotropy plays a role on how hydrogen affects the response under load [123], [125]. It is important to notice the variation in the slope of the elastic segment of each stress-strain response, which notably diminishes with increasing hydrogen concentration. This aligns with findings of hydrogen decreasing the elastic modulus in a defect-free perfect crystal [26], [152], [153].

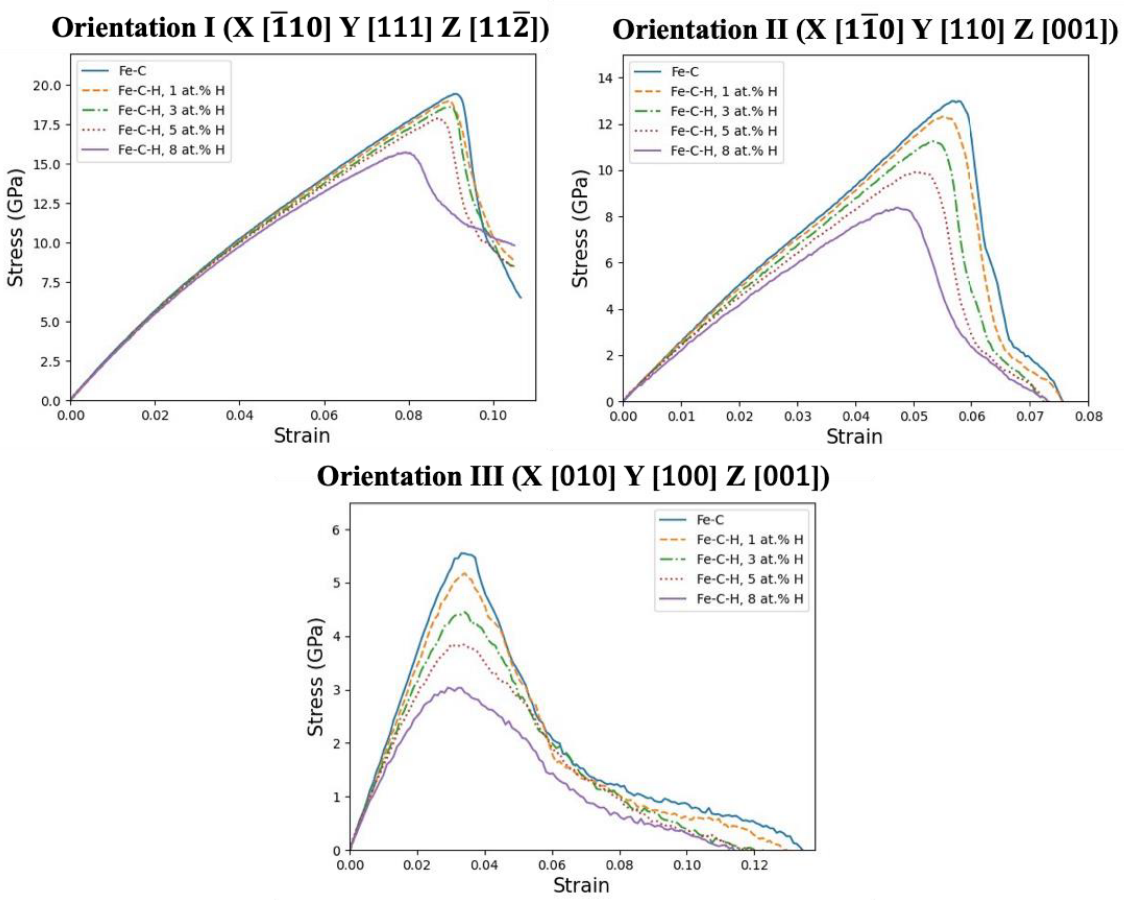

Figure 29 – Plots depicting stress - strain response for all orientations.

Table 6 – Comparison of peak stress and yield strain for all orientations.

Orientation	System	Peak stress (GPa)	Change (%)	Yield strain	Change (%)
Orientation I	Fe-C	19.48	-	0.0926	-
	Fe-C-H, 1 at. % H	18.99	-2%	0.0895	-3%
	Fe-C-H, 3 at. % H	18.64	-4%	0.0895	-3%
	Fe-C-H, 5 at. % H	17.92	-8%	0.0869	-6%
	Fe-C-H, 8 at. % H	15.75	-19%	0.0790	-15%
Orientation II	Fe-C	13.02	-	0.0567	-
	Fe-C-H, 1 at. % H	12.34	-5%	0.0555	-2%
	Fe-C-H, 3 at. % H	11.29	-13%	0.0530	-6%
	Fe-C-H, 5 at. % H	9.93	-24%	0.0509	-10%
	Fe-C-H, 8 at. % H	8.40	-36%	0.0486	-14%
Orientation III	Fe-C	5.62	-	0.0342	-
	Fe-C-H, 1 at. % H	5.21	-7%	0.0339	-1%
	Fe-C-H, 3 at. % H	4.50	-20%	0.0339	-1%
	Fe-C-H, 5 at. % H	3.93	-30%	0.0335	-2%
	Fe-C-H, 8 at. % H	3.12	-45%	0.0326	-5%

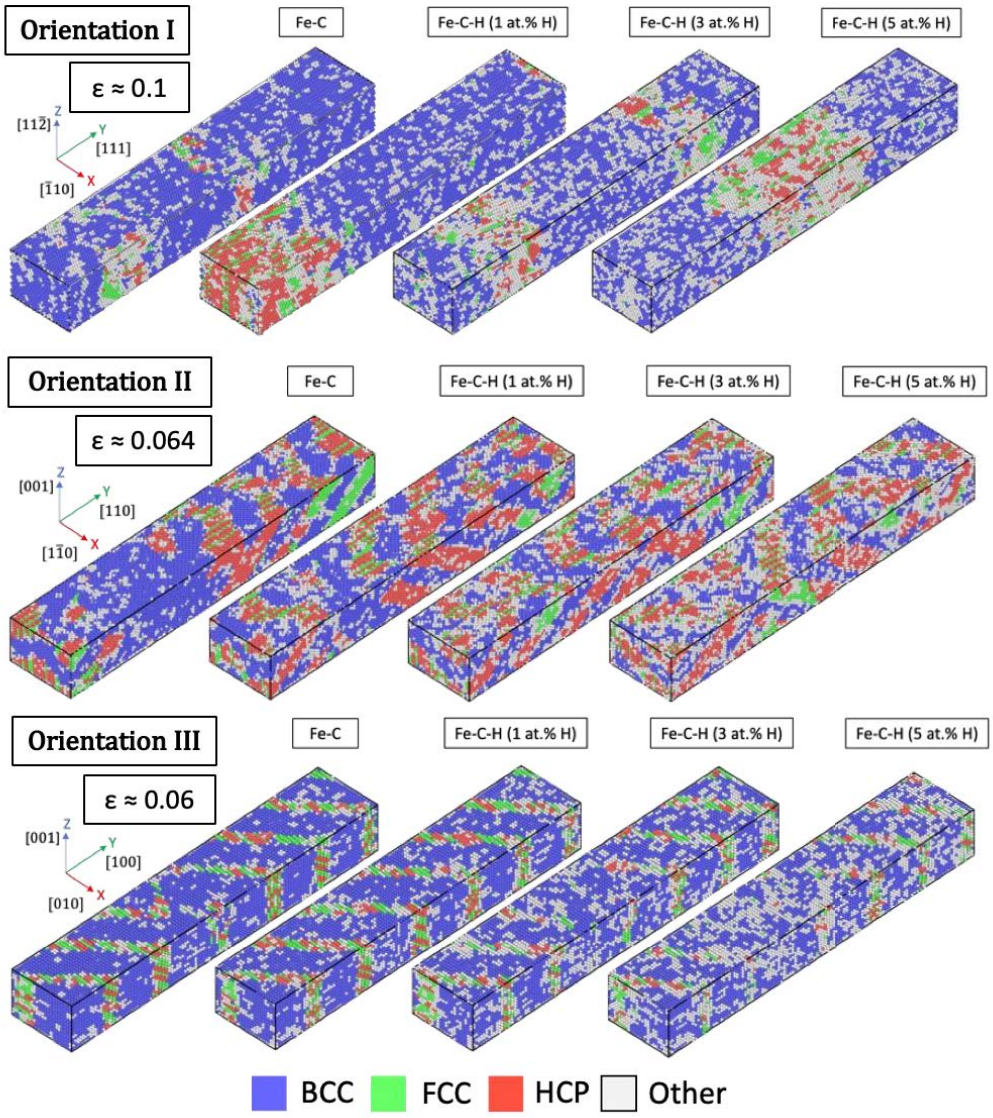

Figure 30 – Simulation snapshots during loading, at or around yield, for all orientations. The highest hydrogen concentration was omitted.

The stress-strain response can be observed at two points: right before the transition from the elastic to the plastic region, and the plastic region itself. Two possible shear mechanisms that could yield the systems are dislocation emission and phase transformation (from BCC to FCC/HCP). Figure 31 shows the dislocation emission for all orientations. Dislocation emission seems dependent on the orientation, as it is observed only in Orientation I. As Orientations II and III do not emit dislocations, it could be suggested that the only yielding mechanism for these two orientations is

the phase transformations observed. Phase transformation releases energy via lattice shearing in {100} planes [102], [113], and these elevated stress levels could potentially activate the stress transformation as a means of energy release, observed experimentally [106], [107], in simulations [30], [112], and both experimentally and in simulations [101], [102]. The orientation of these planes relative to the loading direction varies, resulting in characteristic bands, especially noticeable in Orientation II and III. The presence of hydrogen appears to lower the stress required for phase transformation, potentially causing earlier yielding at higher hydrogen concentrations. However, the total amount of phase transformation does not necessarily increase with hydrogen concentration. For instance, in Orientation I (Figure 32), the most substantial transformation occurs at 1 at. % H, diminishing at higher concentrations. In contrast, Orientation II (Figure 33) exhibits a consistent level of transformation across all hydrogen concentrations, suggesting independence from hydrogen concentration. Orientation III (Figure 34) seems to support the same conclusion. These findings indicate that up to a certain amount, or even independent of the concentration, hydrogen might promote BCC to FCC/HCP phase transformations in certain directions, possibly due to lattice distortion [108]. Nonetheless, the main takeaway would be hydrogen initiating phase transformation at a lower stress as hydrogen concentration is increased, and possibly also anticipating initial dislocation emission as observed in Figure 31 (specifically in the case of Orientation I).

During the plastic region, plastic deformation is a multifaceted phenomenon that can involve phase transformation, dislocation emission, and vacancy formation. Referring again to Figure 31, Orientation I reveals a complex interplay between hydrogen concentration and dislocation emission. Specifically, two distinct patterns emerge. In terms of dislocation count per volume (count/nm^3), there is a peak observed at a 3 at. % H concentration. This suggests that within certain

hydrogen concentration ranges, there is an increase in the nucleation of dislocations, supporting the HELP mechanism in this range. However, this increase in dislocation count does not correlate with an increase in the total length of the dislocations. When considering the metric of dislocation length per volume (nm/nm^3), the data indicates a decrease as hydrogen concentration increases. In fact, the Fe-C system without hydrogen consistently presents the longest dislocations. Figure 35 provides simulation snapshots at approximately 0.1 strain, which illuminate the aforementioned patterns. In the absence of hydrogen, the system tends to form numerous elongated dislocations. However, as we introduce hydrogen, these dislocations appear to shorten, and become virtually non-existent with a concentration of 8 at. % H. As such, two distinct behaviors are observed: a lower hydrogen concentration appears to promote the nucleation of dislocations, as suggested by Xing et al. [99], resulting in a greater number of shorter dislocations. However, as hydrogen concentration increases, both the nucleation and growth of dislocations start to be suppressed, also indicated by Xing et al. [99] as well as numerous other studies [24], [27], [28], [30]–[32], [71], [97], [98], pointing away from the HELP mechanism. This highlights the inner complexity of dislocation emission with increasing hydrogen concentration, not completely explaining the clear pattern seen on the stress-strain response plots, where yielding occurs earlier as the concentration of hydrogen is increased. Nonetheless, Figure 31 suggests that independent of the dislocations formed during the plastic range, hydrogen could anticipate the initial emission of dislocations. On the other hand, vacancy formation seems consistent once plastic deformation starts, marking a clear trend, as generally increasing hydrogen concentration increases vacancy formation in all three orientations (Figure 36). Nevertheless, there is some overlap, especially with the two highest hydrogen concentrations (5 and 8 at. % H), which even interchange places at the end in Orientation II, resulting in the highest vacancy formation with a concentration of 5 at. % H. For Orientation

III, the highest vacancy formation is consistently observed with a concentration of 3 at. % H. This suggests that the relationship between hydrogen concentration and vacancy formation is linear but only up to a point, varying by orientation. Additionally, the variation in behavior across the different orientations, despite a general consistency, demonstrates that the effect of hydrogen varies in each direction (indicating anisotropic properties). This overarching trend of increased vacancy creation in response to the presence of hydrogen persists across the board, suggesting the HESIV mechanism as proposed in various studies [31], [32], [71], [74]–[76], [89], [95], [97]. However, discerning the impact of vacancies, phase transformation and dislocation emission within the plastic range proves challenging, due to the lack of a clear correlation with the plastic region of the stress-strain curve per orientation.

Given the complexity involved in considering various factors such as orientations, boundary conditions, and interatomic potential, the subsequent step employs the other available potential for Fe-C-H systems, the MEAM potential. This approach aims to assess how the change in potential influences the results under identical simulation conditions, thereby complementing the current understanding on the behavior of the systems.

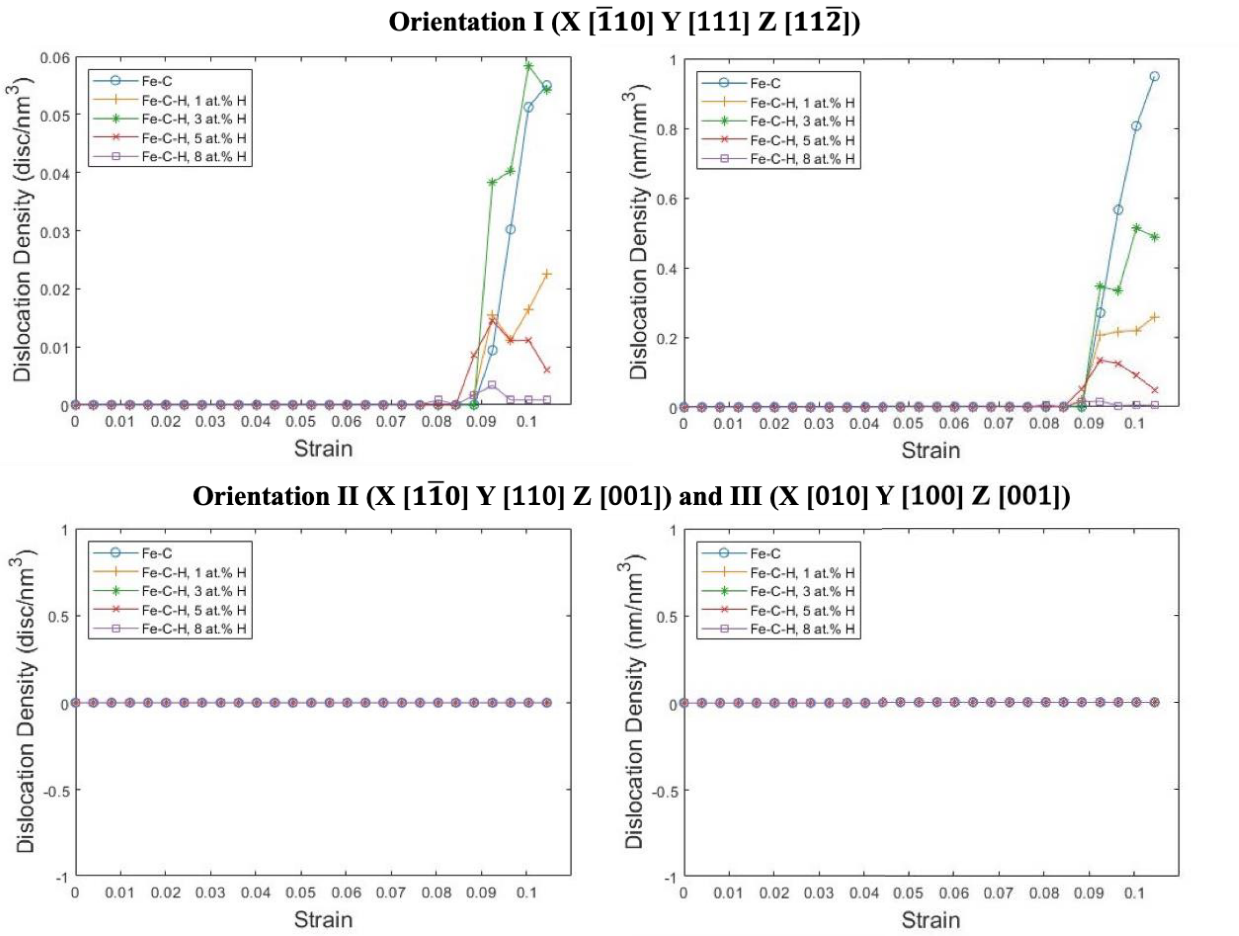

Figure 31 – Plots depicting dislocation density with increasing strain for all orientations.

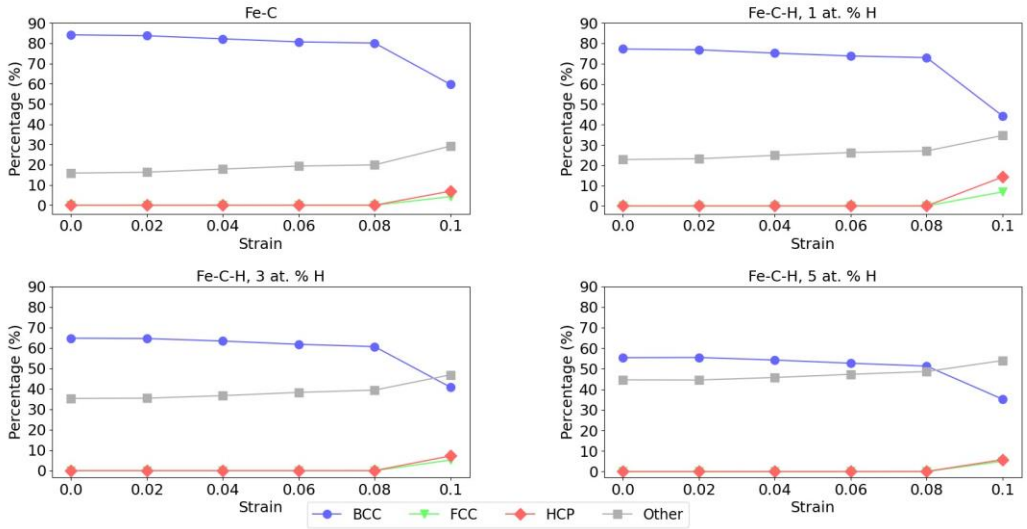

Figure 32 – Plots depicting the relative distribution of the structural phases with strain for Orientation I (X [$\bar{1}$10] Y [111] Z [11$\bar{2}$]).

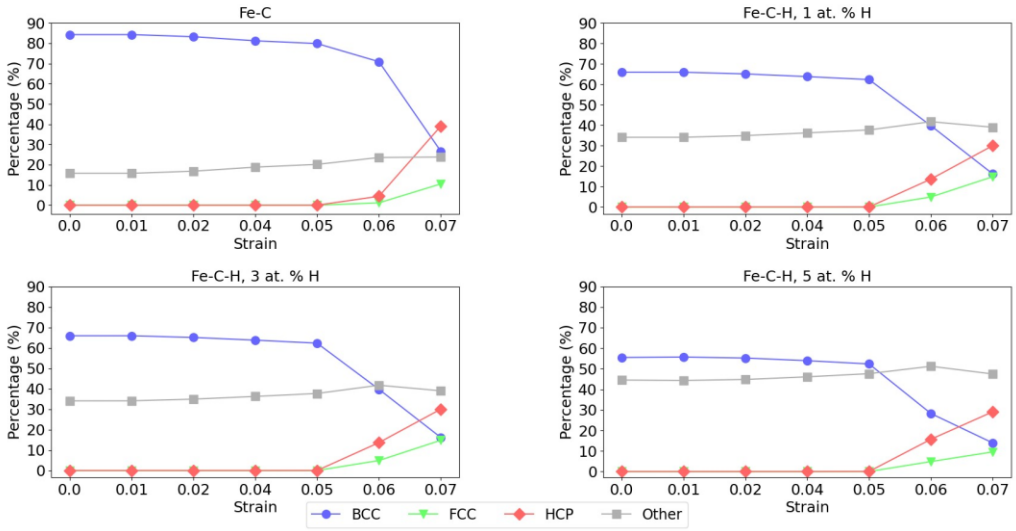

Figure 33 – Plots depicting the relative distribution of the structural phases with strain for Orientation II (X [1$\bar{1}$0] Y [110] Z [001]).

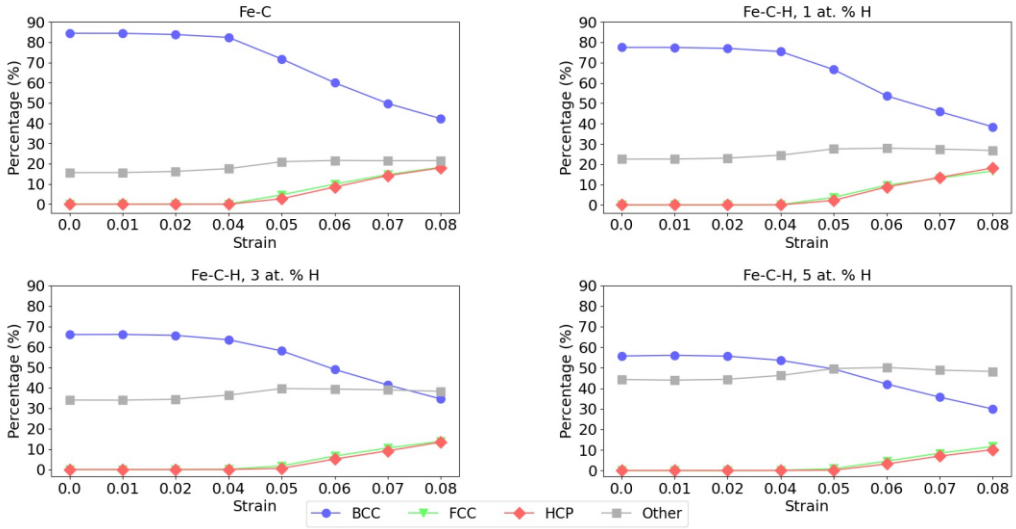

Figure 34 – Plots depicting the relative distribution of the structural phases with strain for Orientation III (X [010] Y [100] Z [001]).

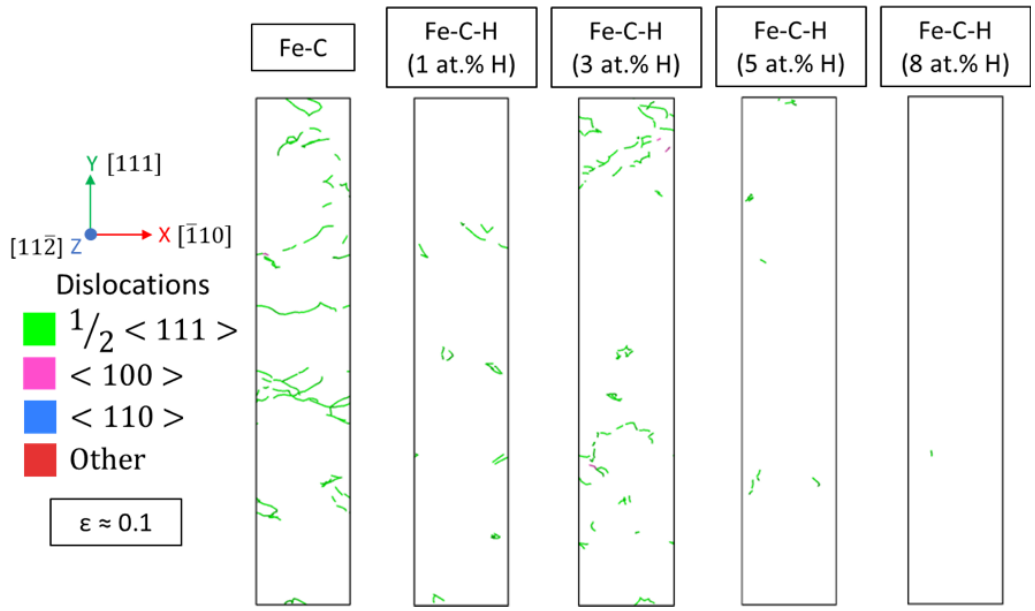

Figure 35 – Simulation snapshots showing the dislocations formed in Orientation I at a strain of around 0.1.

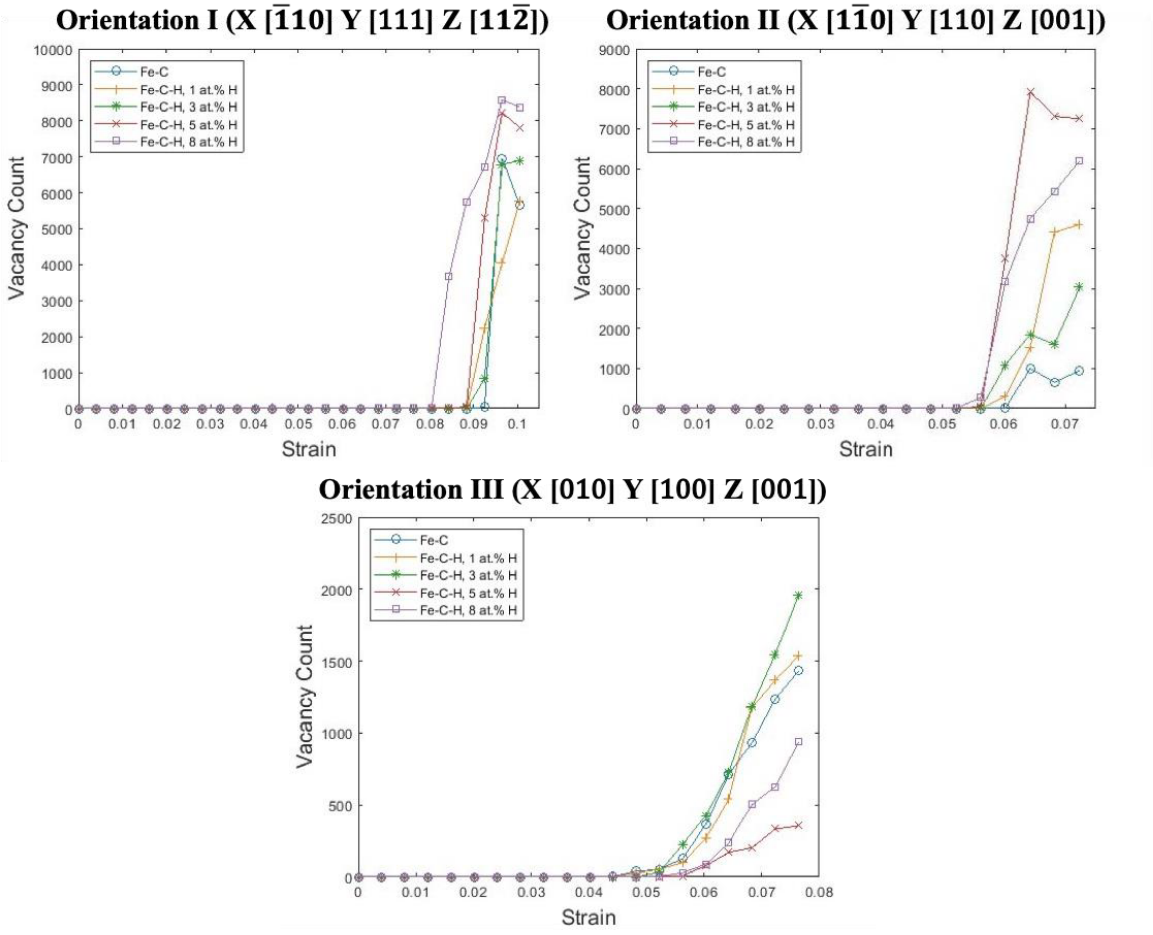

Figure 36 – Plots depicting vacancy count with increasing strain for all orientations.

4.1.2 Modified Embedded Atom Method

In a similar manner to the results using the BOP, Figure 37 shows the stress-strain response for all orientations using the MEAM. Table 7 shows a comparison between the peak stress and the corresponding strain at peak stress for all the Fe-C-H systems relative to the Fe-C system in all orientations. Figure 38 shows snapshots of the systems at the same strain (usually post-yielding) of all orientations. Notice how a consistently lower peak stress is obtained with this potential compared to the BOP. In all cases, the same general trend is present: it is observed where the addition of hydrogen mostly lowers the peak stress obtained, but interestingly the corresponding strain level increases for Orientation I and II. Also, in Orientation I, a hydrogen concentration of 1 at. % seems to increase both peak stress and corresponding strain level. Orientation III does present a decrease in the corresponding strain level as hydrogen concentration is increased.

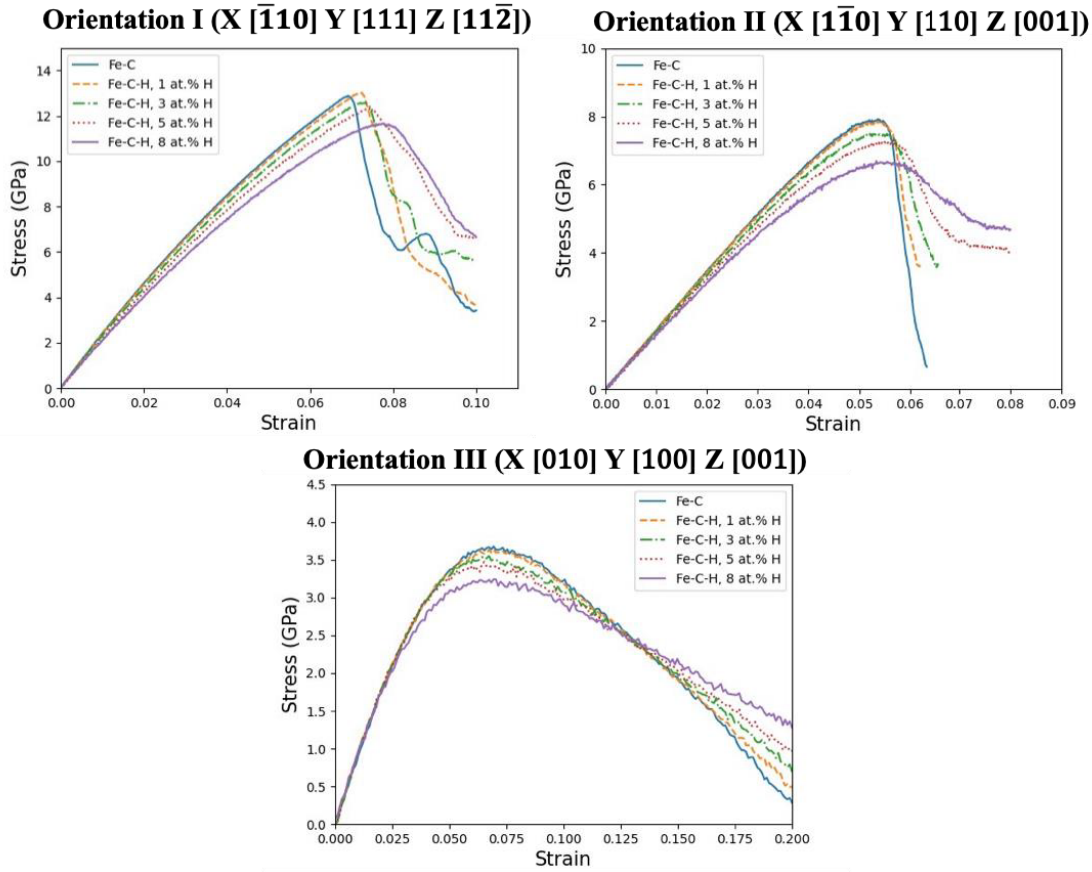

Figure 37 – Plots depicting stress - strain response for all orientations.

Table 7 – Comparison of peak stress and yield strain for all orientations.

Orientation	System	Peak stress (GPa)	Change (%)	Strain at peak stress	Change (%)
Orientation I	Fe-C	12.89	-	0.0690	-
	Fe-C-H, 1 at. % H	13.06	1%	0.0722	5%
	Fe-C-H, 3 at. % H	12.62	-2%	0.0734	6%
	Fe-C-H, 5 at. % H	12.34	-4%	0.0737	7%
	Fe-C-H, 8 at. % H	11.68	-9%	0.0776	12%
Orientation II	Fe-C	7.93	-	0.0520	-
	Fe-C-H, 1 at. % H	7.87	-1%	0.0538	4%
	Fe-C-H, 3 at. % H	7.54	-5%	0.0532	2%
	Fe-C-H, 5 at. % H	7.31	-8%	0.0568	9%
	Fe-C-H, 8 at. % H	6.73	-15%	0.0547	5%
Orientation III	Fe-C	3.71	-	0.0681	-
	Fe-C-H, 1 at. % H	3.66	-1%	0.0680	0%
	Fe-C-H, 3 at. % H	3.60	-3%	0.0673	-1%
	Fe-C-H, 5 at. % H	3.51	-5%	0.0668	-2%
	Fe-C-H, 8 at. % H	3.30	-11%	0.0631	-7%

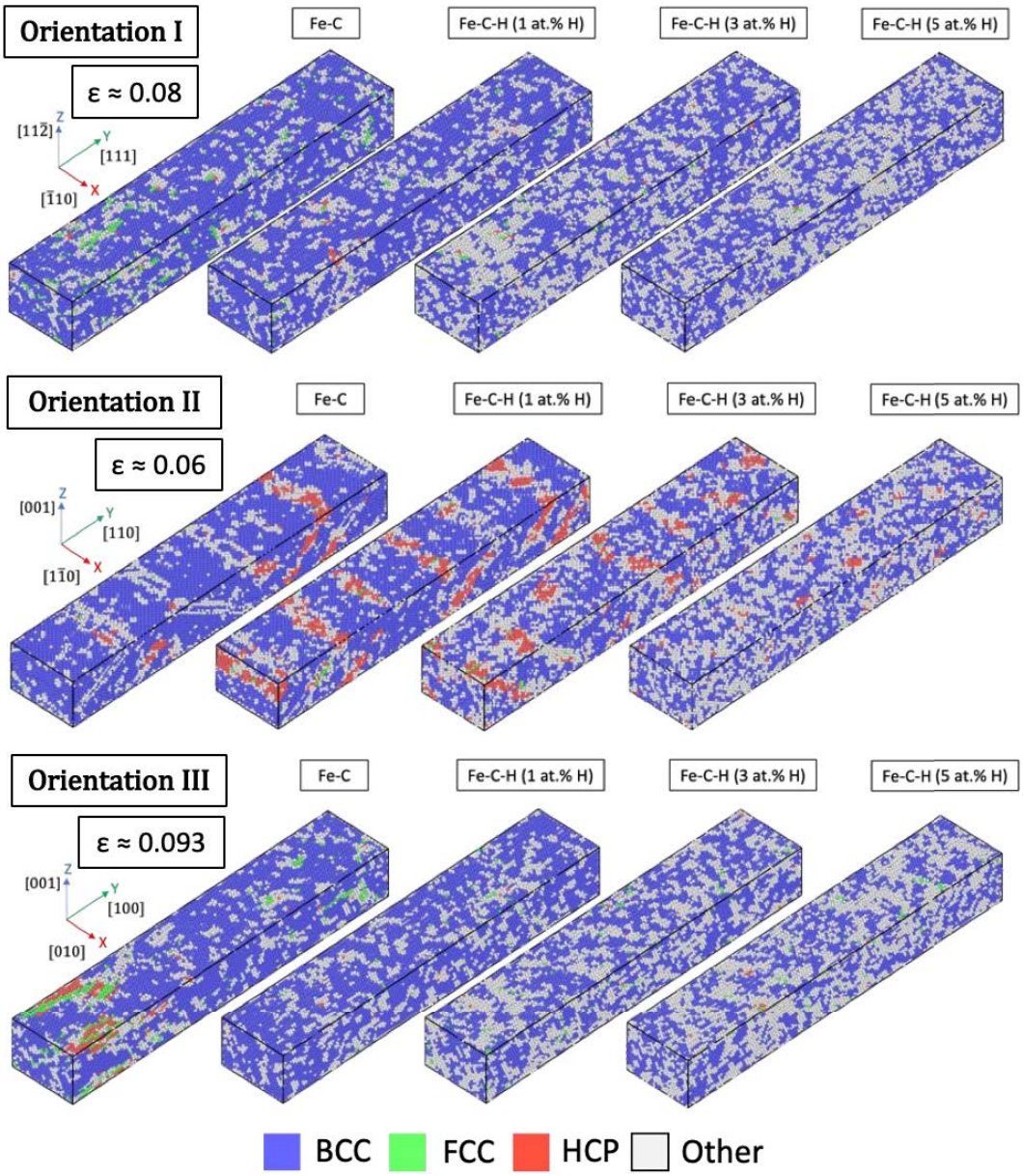

Figure 38 – Simulation snapshots during loading, at or around yield, for all orientations. The highest hydrogen concentration was omitted.

The initial yielding mechanism for Orientations I and II is both dislocation emission and phase transformation. For Orientation III, it would only be phase transformation, similar to what was observed in case of BOP. Figure 39 displays the respective dislocation density plots for Orientation I and II. No plot for Orientation III is provided, as it does not exhibit any dislocations within the studied strain range. Interestingly, results with this potential indicate that the presence of hydrogen

causes a delay in dislocation emission, manifesting at a higher yielding strain but with nonetheless reduced stress. This phenomenon likely accounts for the delayed yielding observed in Orientations I and II. In contrast, Orientation III exhibits earlier yielding as the hydrogen concentration increases, without dislocation emission, but rather through phase transformation. In Orientation I, a hydrogen concentration of 1 and 3 at. % consistently shows the highest dislocation density measured in terms of count/nm^3. A hydrogen concentration of 1 at. % normally results in higher dislocation density, expressed in nm/nm^3, but is occasionally surpassed by 3 at. % H and the base Fe-C system while loading. Beyond 3 at. % H, there is a steady decline in dislocation density for both types of measurements. Overall, this pattern follows the behavior observed with the BOP, again supporting the suggestion from Xing et al. [99] that hydrogen can increase dislocation density up to a certain concentration, beyond which dislocation emission is inhibited. Orientation II shows a different trend, where the addition of hydrogen inhibits dislocation emission at any concentration, hinting at the effects of anisotropy. Interestingly, though, more dislocations are emitted at a concentration of 3 at. % H compared to 1 at. % H. Figure 40 showcases simulation snapshots around a strain of 0.1 and 0.08 for Orientation I and II, respectively, where the aforementioned trends can be visualized. Looking at Figures 41-43 (phase transformation plots for Orientation I, II, and III respectively), all three orientations undergo phase transformation, but it is more significant in Orientations II and III. Overall, a notable reduction in phase transformation is observed, which may be attributed to the lower peak stress obtained when compared to the results obtained with the BOP. In Figure 41, Orientation I exhibits visible phase transformation in the base Fe-C system only, with no apparent increase in transformation rates as hydrogen concentration rises. A similar case is seen in Figure 43, as the highest phase transformation in Orientation III is seen without the presence of hydrogen. Only in Orientation II does the presence

of hydrogen seem to affect the phase transformation, with the highest transformation observed at a concentration of 5 at. % H. This finding somewhat contrasts with the BOP results for the same orientation, where phase transformation seemed unaffected by hydrogen concentration. In general, the results point away from hydrogen generally enhancing the quantity of phase transformation, also partially supported by the results observed using the BOP. However, the results with both potentials do not rule out that in certain conditions hydrogen might actually aid phase transformation. In addition, particularly to the MEAM potential, hydrogen increases the strain at yield, but nonetheless the yield strength is generally lowered as concentration is increased.

As in the case with the BOP, the plastic portion in the stress-strain curve, strain presents an erratic behavior. Once the yielding starts, vacancies start to form. Figure 44 presents the vacancy count plot for all orientations. After yielding, Orientation I and III maintain, in general, the same consistent trend (increasing vacancy formation as hydrogen concentration is increased), but Orientation II displays varied outcomes. This can be partially attributed to the increased yield strain as hydrogen concentration is increased (peaking at 5 at. % H) as this can directly influence the initial surge in vacancy formation. However, this increased yield strain is also observed in Orientation I as hydrogen concentration increases, but it does not reflect the same degree of inconsistency in vacancy formation. In Orientation III, despite showing a considerably lower number of vacancy formation (below 30 compared to more than 1000s) compared to the amount observed using the BOP, there is a clear trend indicating an increase in the number of vacancies with rising hydrogen concentration. The overall picture suggests that HESIV is present in all orientations once each respective yield occurs, but might be limited to a maximum concentration of hydrogen. Nonetheless, as with the BOP, the effect that HESIV has on the stress-strain curve is not easy to determine in the current simulation conditions.

With the current observations so far in Case 1, it is indicated that the BOP achieves higher peak stress compared to the MEAM potential, which may be a key factor in the observed differences in phase transformation, as phase transformation is significantly more pronounced with the BOP. This reduced phase transformation observed with the MEAM potential possibly results in energy being released through dislocation emission, as it is observed in Orientations I and II, not only in Orientation I as observed with the BOP. Furthermore, both the BOP and MEAM potentials typically exhibit an increase in vacancy formation as the concentration of hydrogen rises. However, the erratic behavior observed in plastic strain across both potentials complicates the clear understanding of how vacancy formation affects the systems.

As the results so far do not prove conclusive, the subsequent case (Case 2) involves a minor modification to the boundary conditions: applying shrink-wrap in the Y direction. This is done with the aim of observing failure manifested as a fracture, which would be evident in the stress-strain curve as an abrupt decline in stress, approaching zero or a value near it. Plus, it is easily observable in the simulation snapshots. This change is also made as an attempt to reduce or eliminate the erratic behavior in the plastic region, as the fully periodic boundary conditions inhibit fracture (most probably by delaying void formation and growth [92]), and can be considered a large factor behind this behavior.

Orientation I (X [$\bar{1}$10] Y [111] Z [11$\bar{2}$])

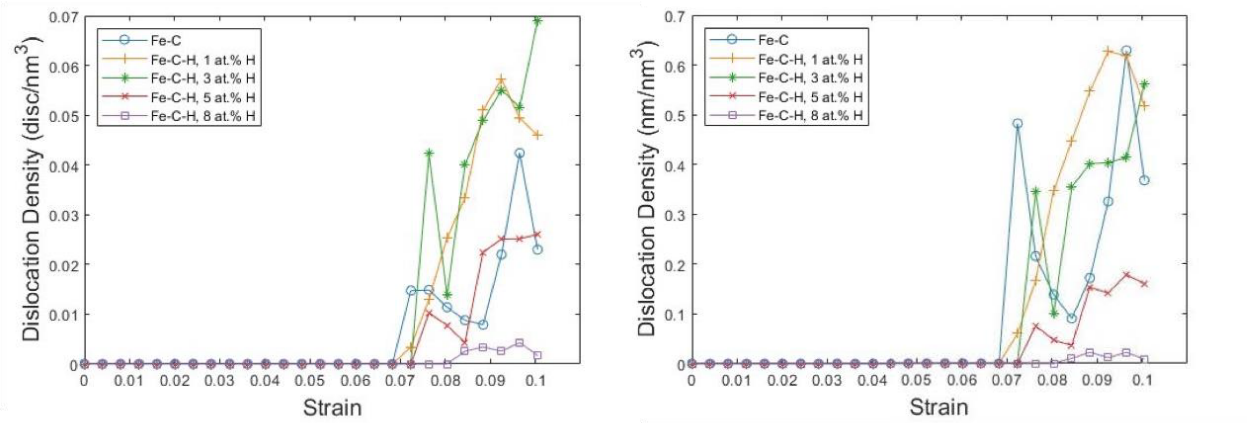

Orientation II (X [1$\bar{1}$0] Y [110] Z [001])

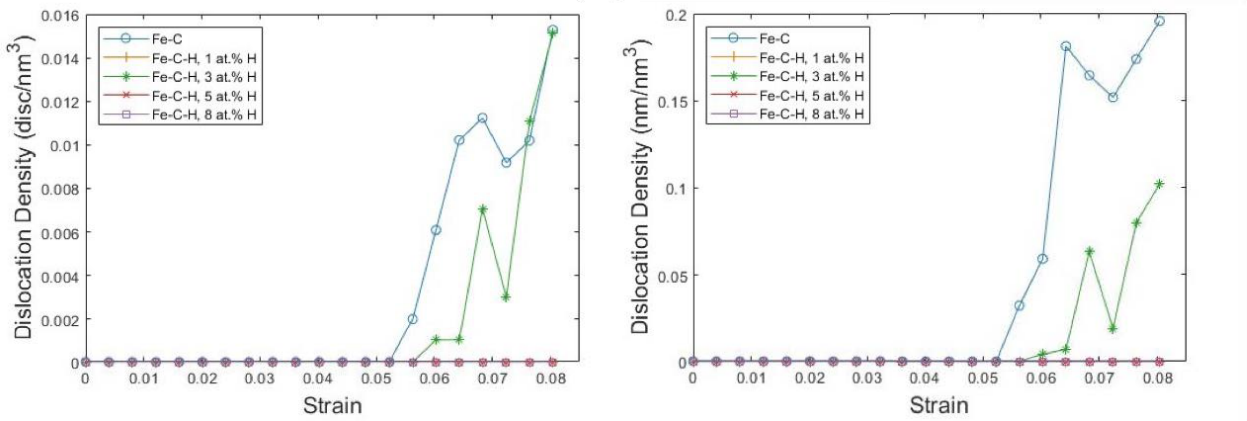

Figure 39 – Plots depicting dislocation density with increasing strain for Orientation I and II.

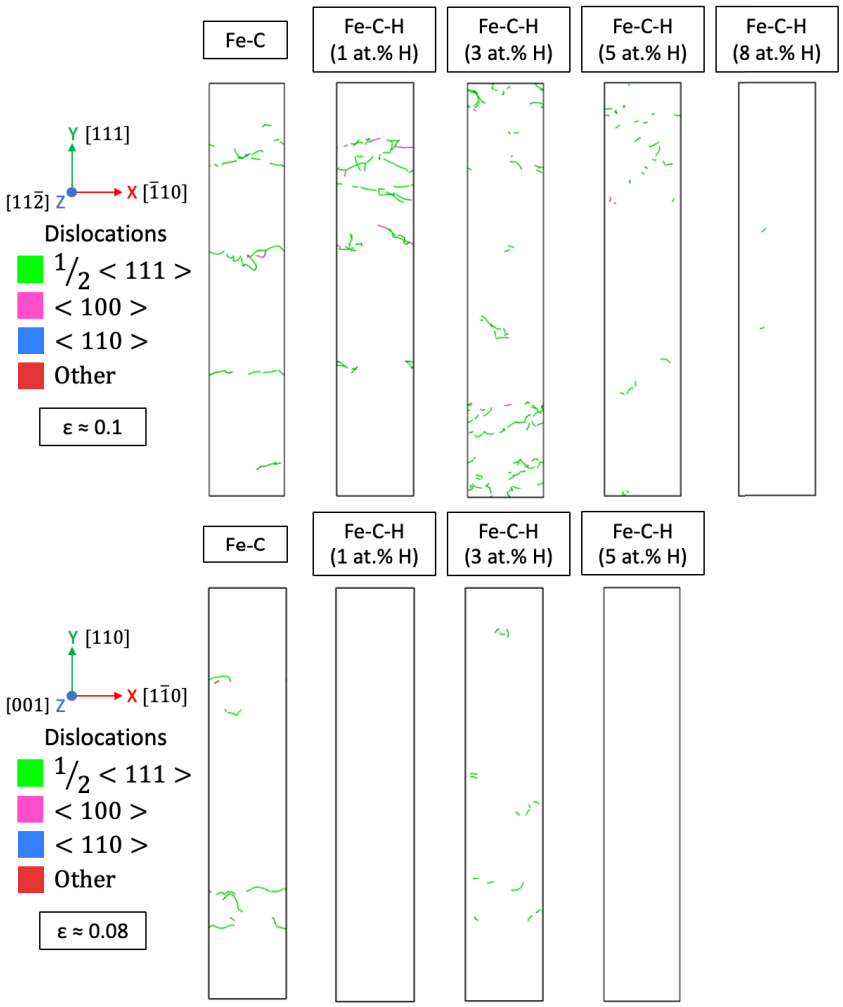

Figure 40 – Simulation snapshots showing the dislocations formed in Orientation I and II at a strain of around 0.1 and 0.08 respectively.

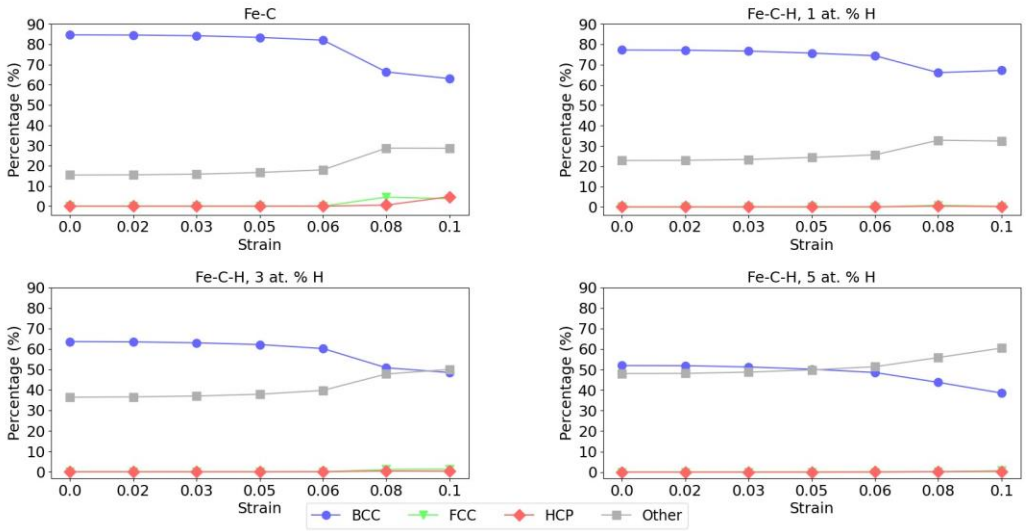

Figure 41 – Plots depicting the relative distribution of the structural phases with strain for Orientation I (X [$\bar{1}$10] Y [111] Z [11$\bar{2}$]).

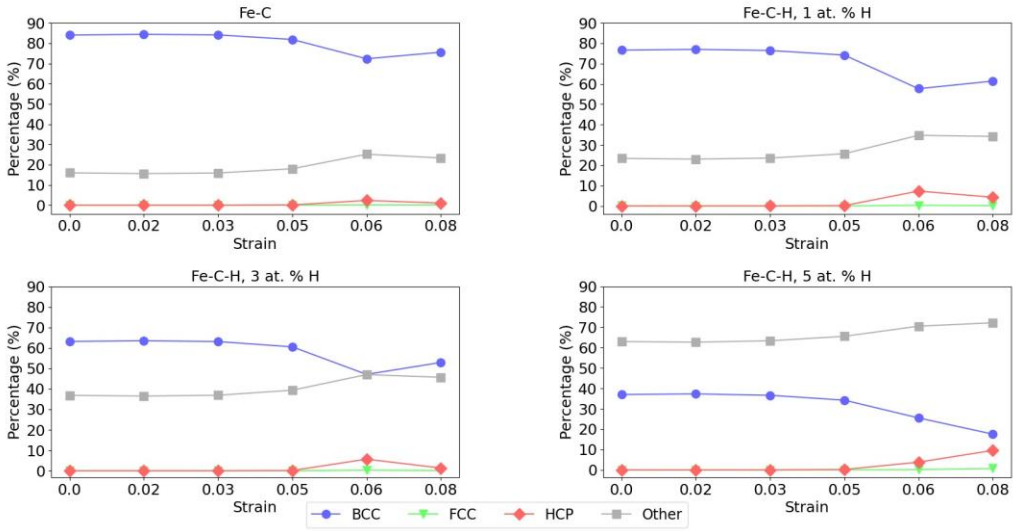

Figure 42 – Plots depicting the relative distribution of the structural phases with strain for Orientation II (X [1$\bar{1}$0] Y [110] Z [001]).

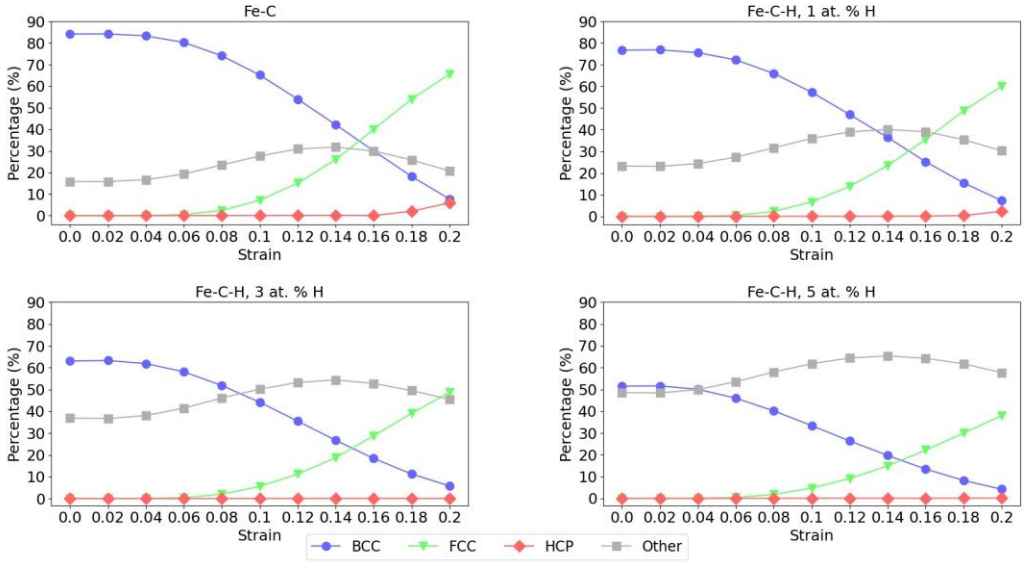

Figure 43 – Plots depicting the relative distribution of the structural phases with strain for Orientation III (X [010] Y [100] Z [001]).

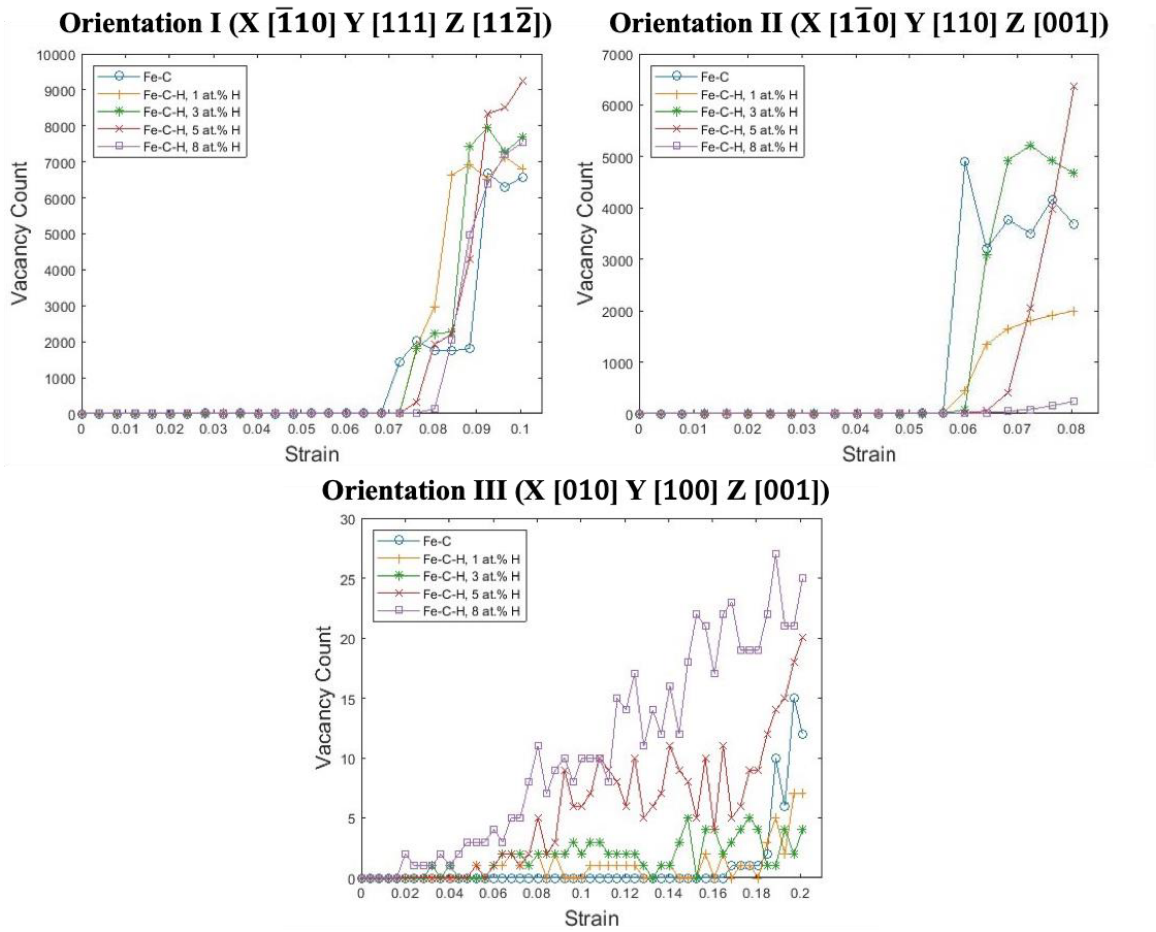

Figure 44 – Plots depicting vacancy count with increasing strain for all orientations.

4.2 Case 2: Single-Crystalline with Shrink-Wrap Boundary Condition in Y Axis

4.2.1 Bond Order Potential

As with Case 1, the stress-strain response will be discussed first. Figure 45 illustrates the stress-strain response for all orientations. These figures are further complemented by Table 8, showing a comparison between the peak stress and the strain at or near when fracture occurs, highlighting that peak stress does not necessarily coincide with failure, especially in Orientations I and II. Meanwhile, Figure 46 presents simulation snapshots taken near the point of fracture for each respective orientation, which is now possible with the shrink-wrapped boundary condition in the Y direction, as fracture is not inhibited. As evidenced by prior models, it is observable that hydrogen generally impairs the mechanical properties of each system. Typically, systems with

hydrogen attain a lower maximum strain than their hydrogen-absent counterparts. The exception is Orientation I, and while it does achieve a higher strain prior to fracture as the hydrogen concentration is increased, it simultaneously reaches a diminished peak stress. Notably, the stress level in the systems with hydrogen starts to decline before that of the Fe-C system, but nonetheless reach fracture afterwards. Also, in Orientation II, there does not seem to be a marked difference on the fracture strain between a hydrogen concentration of 3 and 8 at. %, but the peak stress obtained definitely lowers with the higher concentration. The influence of hydrogen on the different orientations becomes more pronounced under these specific boundary conditions, and it is interesting to see how the location of fracture initiation actually varies in some cases. In other words, the local increase and accumulation of vacancies may eventually form voids, leading to fracture.

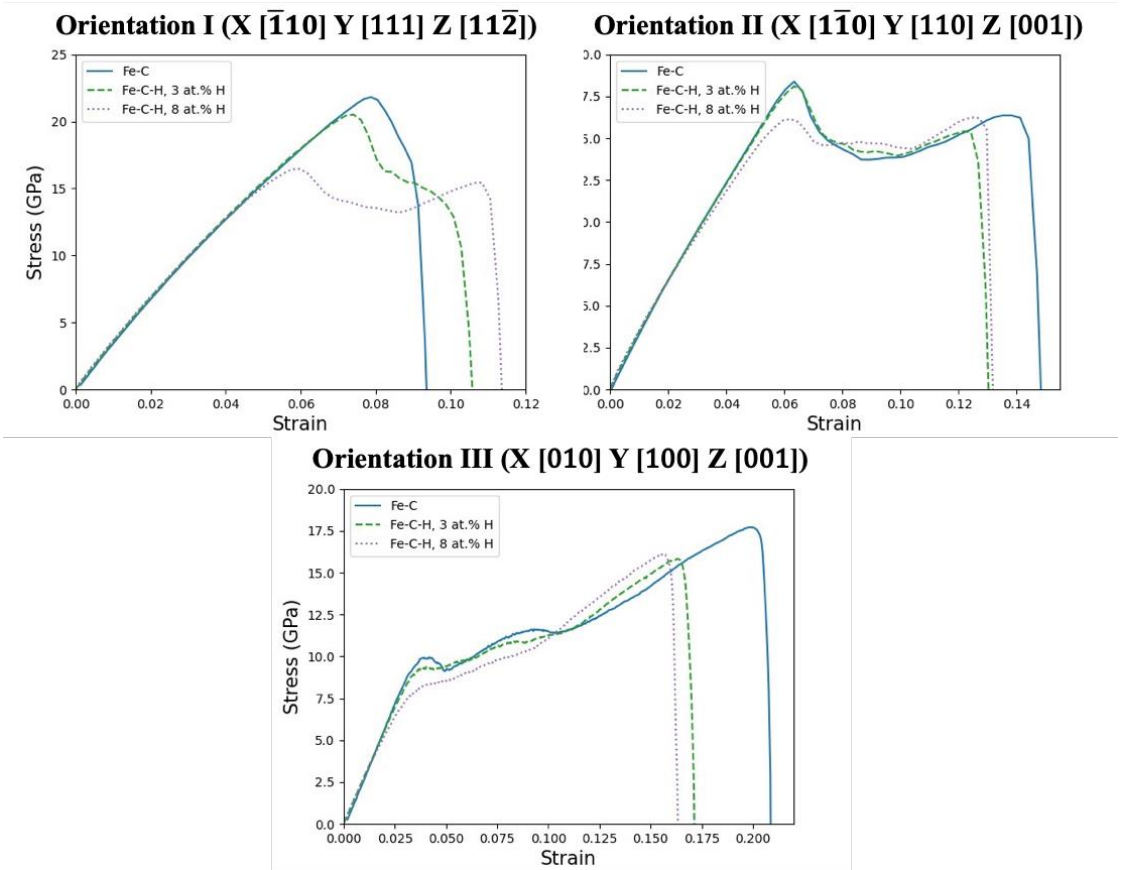

Figure 45 – Plots depicting stress – strain response for all orientations.

Table 8 – Comparison of peak stress and fracture strain for all orientations.

Orientation	System	Peak stress (GPa)	Change (%)	Fracture strain	Change (%)
Orientation I	Fe-C	21.84	-	0.078	-
	Fe-C-H, 3 at. % H	20.56	-6%	0.105	33%
	Fe-C-H, 8 at. % H	16.54	-24%	0.109	39%
Orientation II	Fe-C	18.42	-	0.143	-
	Fe-C-H, 3 at. % H	18.18	-1.29%	0.126	-12%
	Fe-C-H, 8 at. % H	16.28	-11.63%	0.126	-12%
Orientation III	Fe-C	17.97	-	0.206	-
	Fe-C-H, 3 at. % H	15.83	-12%	0.163	-21%
	Fe-C-H, 8 at. % H	16.11	-10%	0.156	-24%

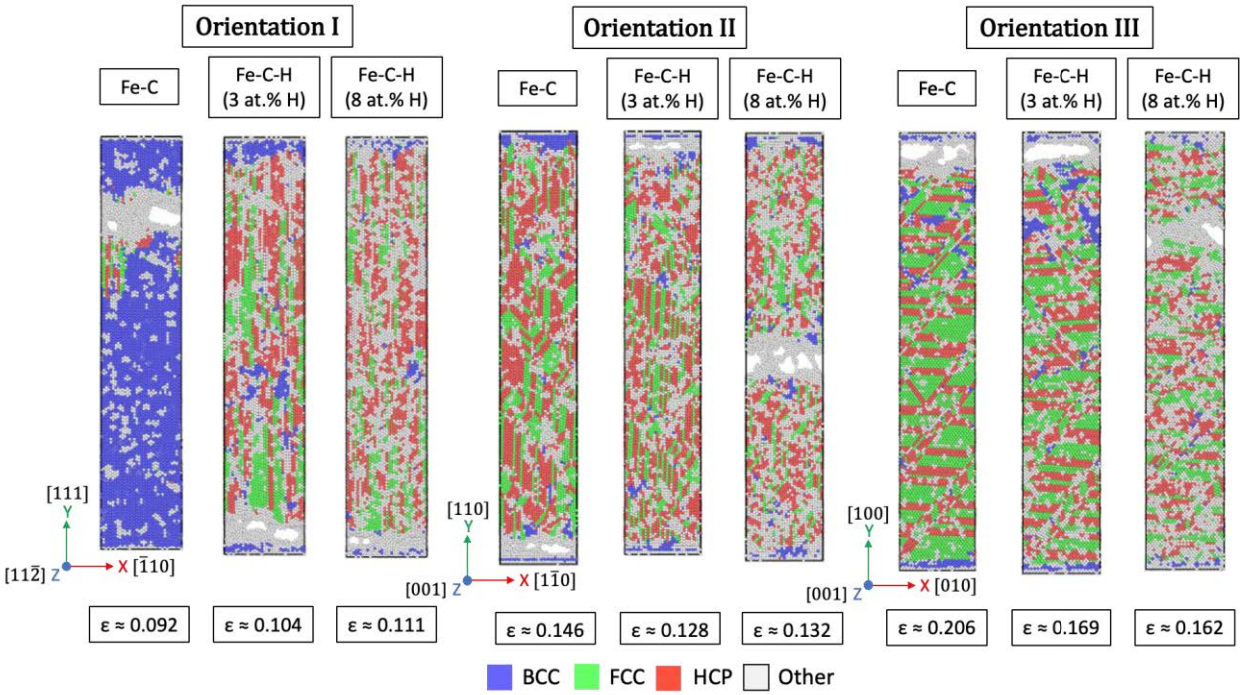

Figure 46 – Simulation snapshots during loading, at fracture strain, for all orientations.

Compared to Case 1, the yield initiation mechanism is solely phase transformation, as no dislocations are emitted in any orientation when using this potential. Figures 47-49 present the relative phase distributions for Orientation I, II, and III, respectively. For Orientation I, the data

suggests that the presence of hydrogen continues to assist the phase transformation, but increased hydrogen concentration does not necessarily increase phase transformation. This is shown to a lesser extent in Orientations II and III. Once more, the influence of crystallographic orientations on the phase transformations is notable.

The plastic region starts once the first considerable dip in stress occurs, and it marks the initiation in the formation of vacancies. The vacancy formation plots are shown in Figure 50, which presents results for all orientations. A consistent phenomenon is observed across the varying orientations as, like in Case 1, the inclusion of hydrogen invariably augments the formation of vacancies as the systems are subjected to strain, especially in Orientations I and III. Orientation II shows the vacancy formation for both systems containing hydrogen starting slightly after the base Fe-C system, but once vacancy formation starts, they surpass the base system at higher strains, both systems containing hydrogen failing beforehand. As seen so far, this increase in vacancy formation likely originates from the activation of the HESIV mechanism, impacting directly on the stress-strain behavior of the models. With the exception of Orientation I, systems with hydrogen consistently reaching fracture before their hydrogen-free counterpart, again underlining how the influence of hydrogen can vary depending on the orientation. Nonetheless, hydrogen consistently lowers the yield stress as shown in all three orientations. With the enhanced formation of vacancies as the hydrogen concentration is increased, it is believed that fracture initiation happens due to the HESIV mechanism as voids are formed as vacancies start accumulating locally. Figure 51 (a) presents a comparison of the vacancies formed at approximately the same strain (~ 0.13), between the base Fe-C system and the Fe-C-H system with the highest hydrogen concentration of 8 at. %. This comparison is drawn on a planar cut through the center of each system to enhance vacancy visualization. Note that in the presence of hydrogen, vacancies not only form more uniformly

throughout the system but also appear in greater numbers, often directly adjacent to the hydrogen atoms. On the contrary, in the base Fe-C system, vacancies are distributed less uniformly, resulting in larger empty spaces throughout the system. Figure 51 (b) shows the total number of vacancies and the vacancies around the fracture zone for the same Fe-C-H system, comparing it against the Fe-C system at the same strain level of approximately 0.13. This comparison underscores a marked rise in the concentration of vacancies around the fracture zone in the Fe-C-H system relative to the Fe-C system. The change in the boundary condition definitely helps clarify the impact in the formation of vacancies as fracture is now possible. The next step involves the use of the MEAM potential in combination with shrink-wrap boundary condition to observe if there is any change in the observations.

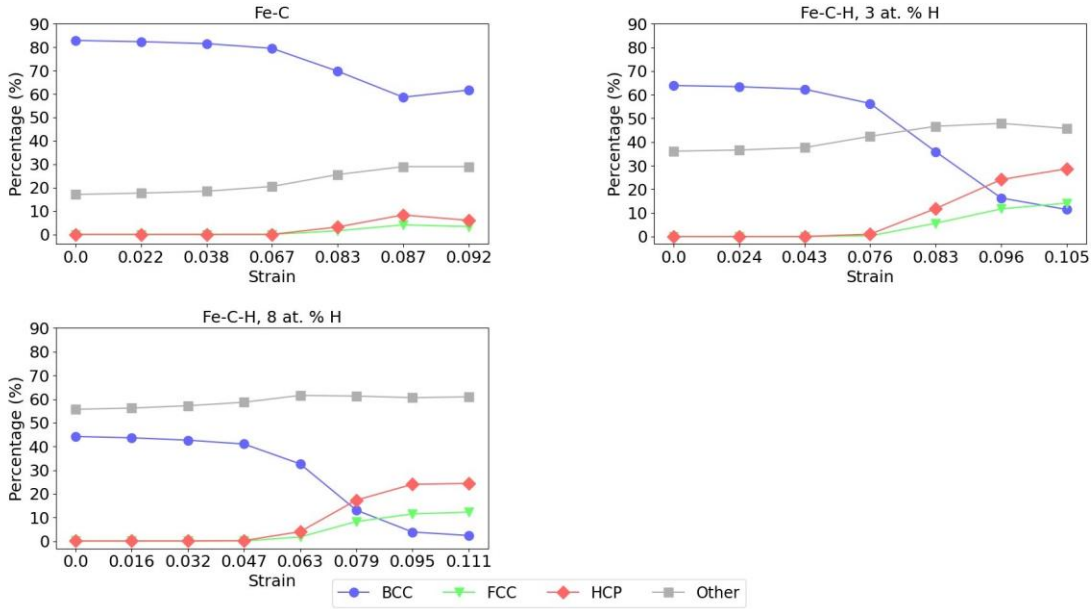

Figure 47 – Plots depicting the relative distribution of the structural phases with strain for Orientation I (X [$\bar{1}$10] Y [111] Z [11$\bar{2}$]).

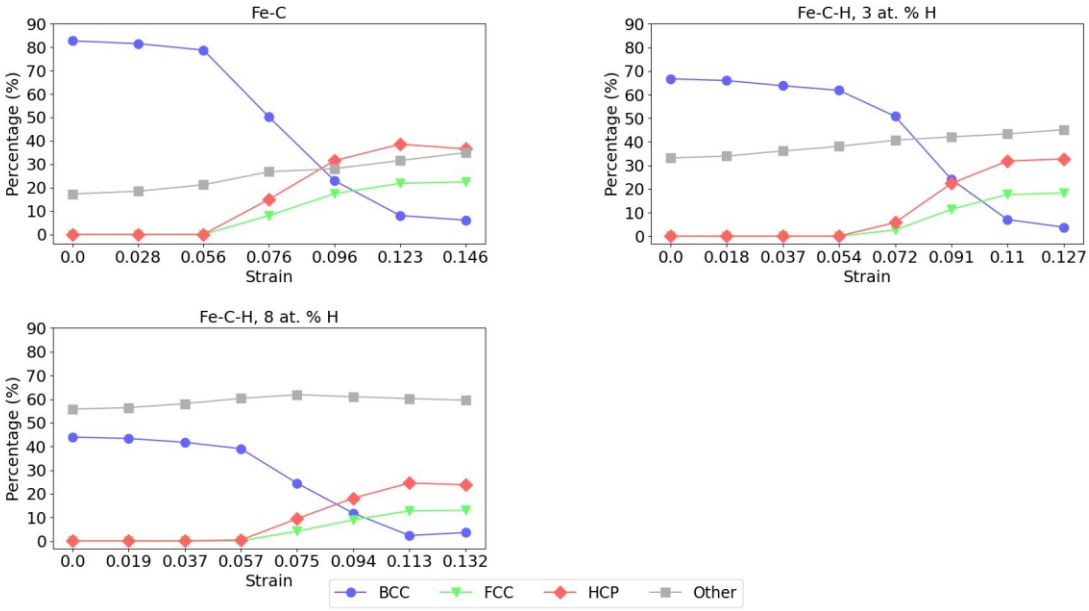

Figure 48 – Plots depicting the relative distribution of the structural phases with strain for Orientation II (X [1$\bar{1}$0] Y [110] Z [001]).

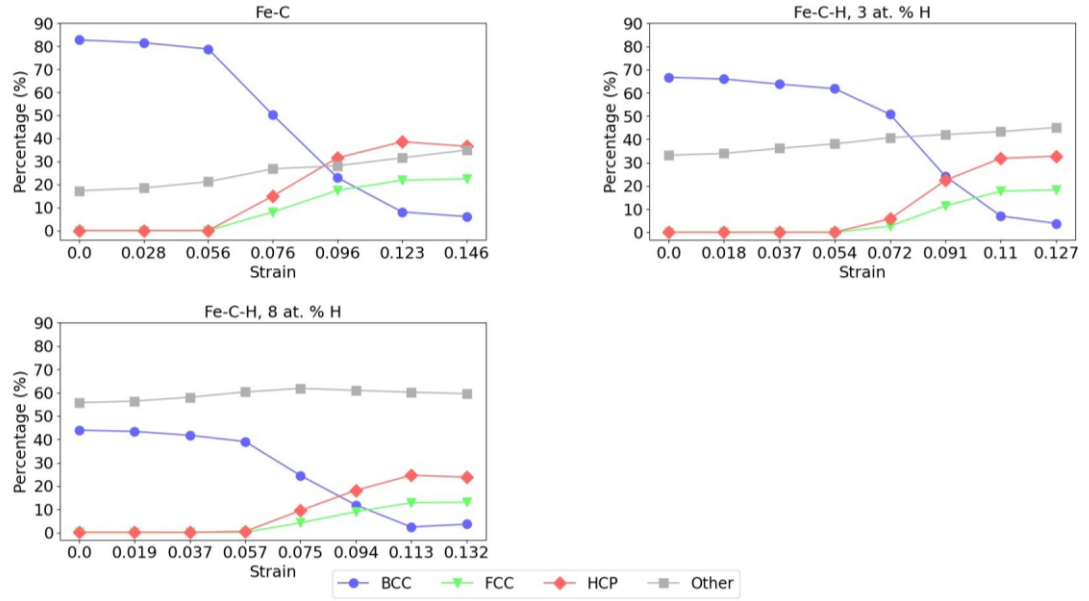

Figure 49 – Plots depicting the relative distribution of the structural phases with strain for Orientation III (X [010] Y [100] Z [001]).

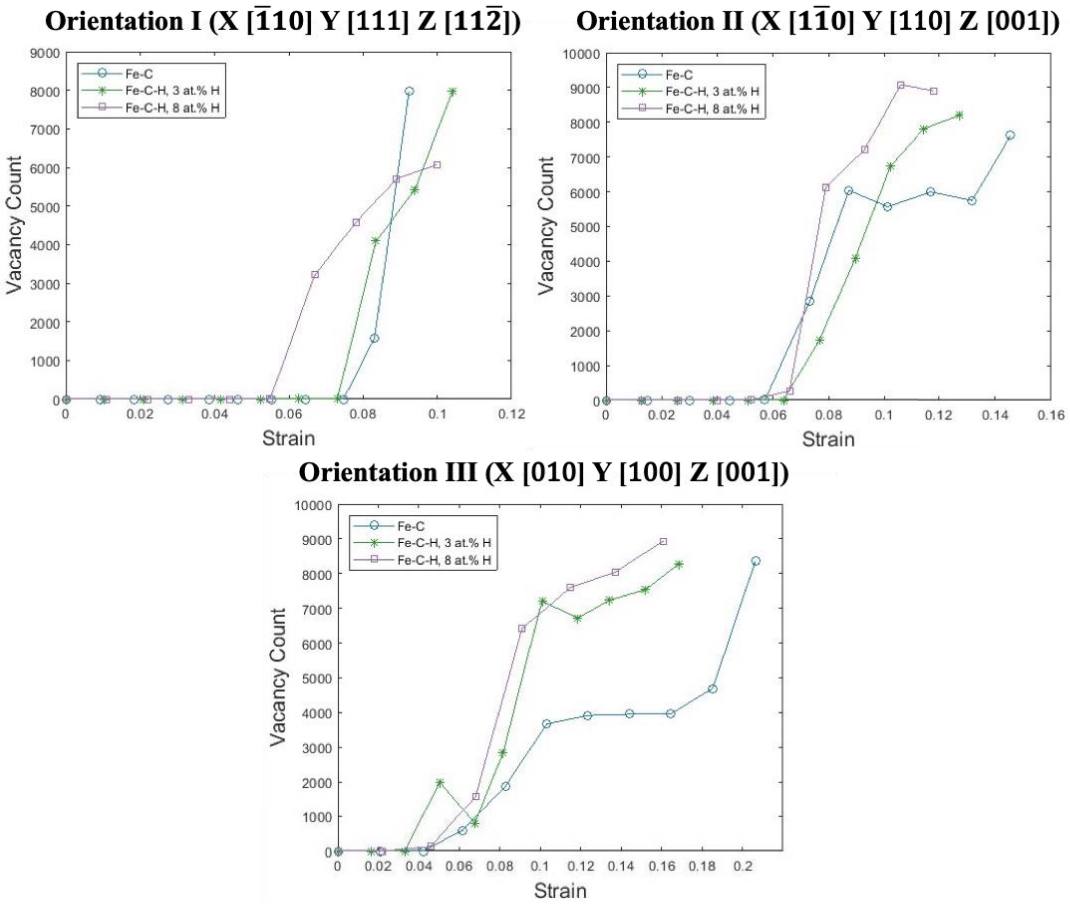

Figure 50 – Plots depicting vacancy count with increasing strain for all orientations.

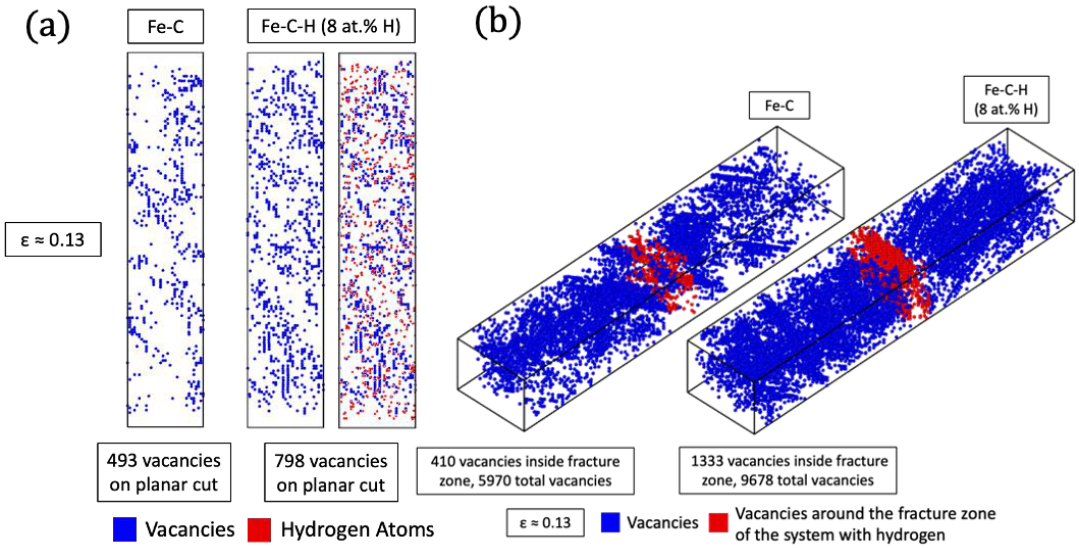

Figure 51 – (a) Visualization of vacancies at the same strain level for the base Fe-C system and Fe-C-H system with a hydrogen concentration of 8 at.%. Blue spots indicate vacancy sites, red spots indicate hydrogen atoms. The planar cut is made at the middle of the systems. (b) Visualization of vacancies at the same strain level near the fracture point for the Fe-C-H system. The concentration of vacancy clusters around the fracture zone is notably higher than in the Fe-C system, with a significantly higher total number of vacancies throughout the system.

4.2.2 Modified Embedded Atom Method

Starting with the stress-strain curve, Figure 52 illustrates the stress-strain responses for all orientations. Table 9 shows a comparison between the peak stress and the fracture strain. Figure 53 presents the corresponding simulation snapshots taken near the point of fracture for all orientations. A similar trend observed with the BOP is shown here, with the exception of Orientation II, where the introduction of hydrogen typically reduces both the peak stress and the fracture strain, though the peak stress is only reduced slightly at most. However, as seen in Orientation II, where the fracture strain increases as hydrogen concentration is increased, and the peak stress remains virtually the same. Contrastingly, in Orientation I, a marginal rise in peak stress is observed at a hydrogen concentration of 3 at. %, but it does not significantly change at the higher hydrogen concentration of 8 at. %, which remains comparable to the base Fe-C system. Furthermore, unlike the behavior under the BOP, Orientation I does not exhibit an increase in fracture strain with increasing hydrogen concentration from 3 at. % H to 8 at. %.

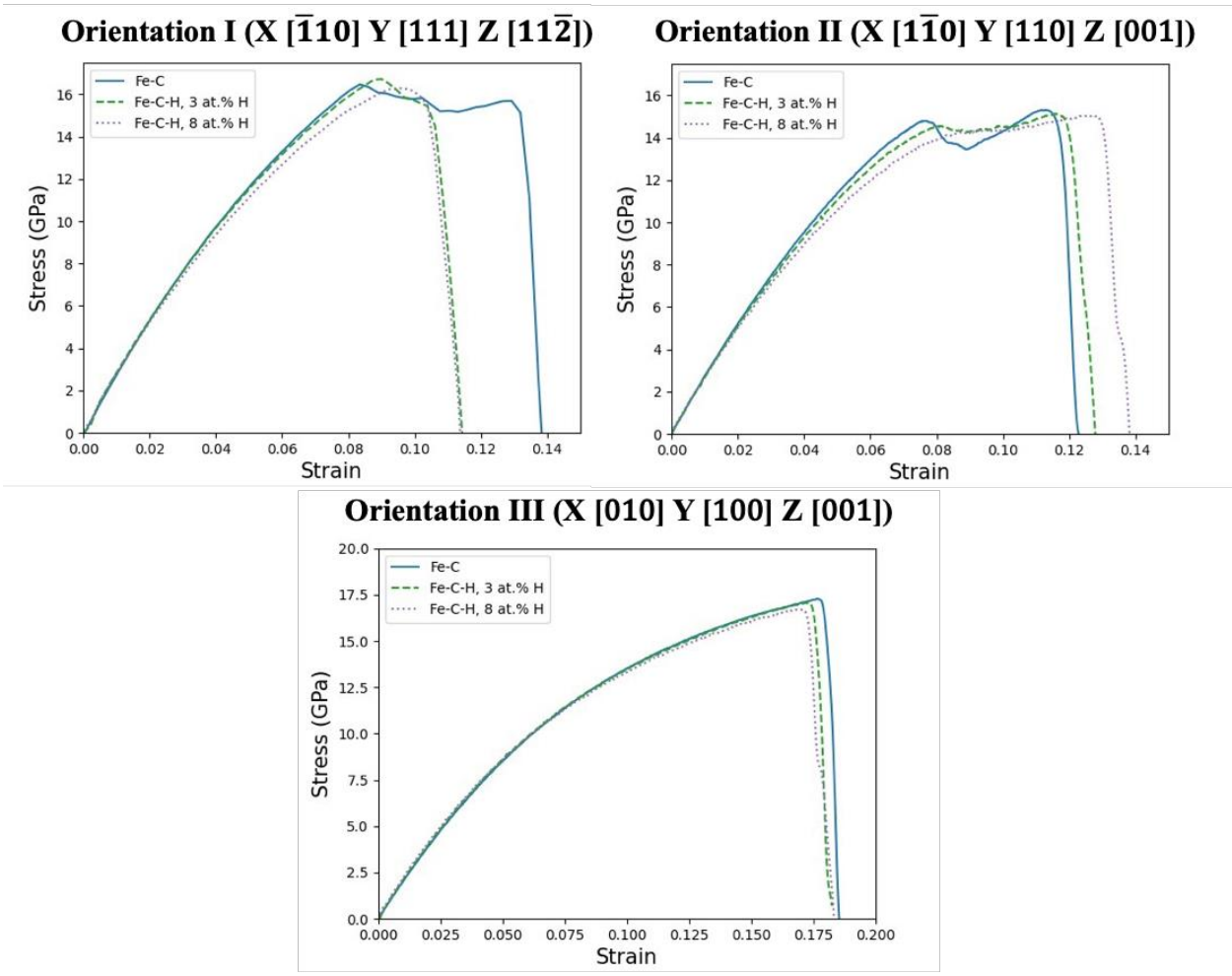

Figure 52 – Plots depicting stress – strain response for all orientations.

Table 9 – Comparison of peak stress and fracture strain for all orientations.

Orientation	System	Peak stress (GPa)	Change (%)	Fracture strain	Change (%)
Orientation I	Fe-C	16.48	-	0.132	-
	Fe-C-H, 3 at. % H	16.35	-1%	0.104	-21%
	Fe-C-H, 8 at. % H	16.34	-1%	0.104	-21%
Orientation II	Fe-C	15.14	-	0.113	-
	Fe-C-H, 3 at. % H	15.16	0%	0.116	2%
	Fe-C-H, 8 at. % H	15.10	-0.3%	0.127	12%
Orientation III	Fe-C	17.28	-	0.176	-
	Fe-C-H, 3 at. % H	17.09	-1%	0.172	-2%
	Fe-C-H, 8 at. % H	16.77	-3%	0.170	-3%

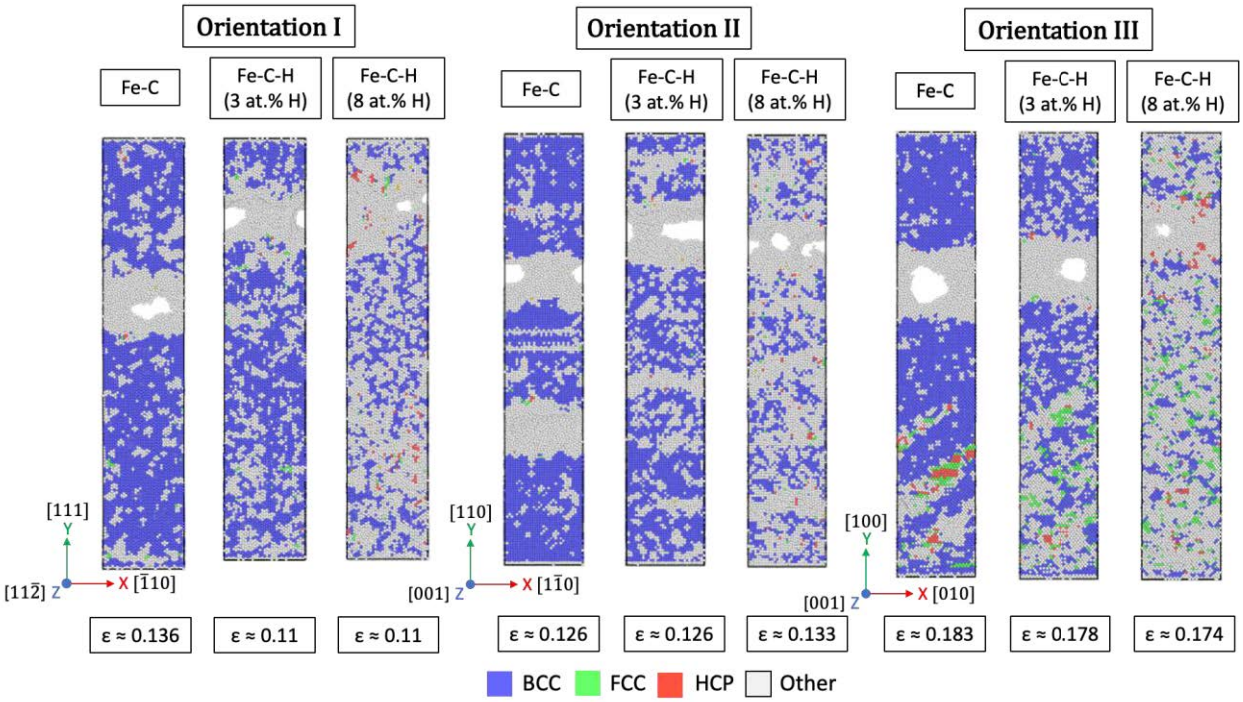

Figure 53 – Simulation snapshots during loading, at fracture strain, for all orientations.

The yielding initiation mechanism, at least for Orientations I and II, is dislocation emission, accompanied by phase transformation, even though it is significantly less compared to what was observed with the BOP, as discussed before in Case 1. Orientation III does not show any emission of dislocations, only phase transformation. Figure 54 displays the dislocation density plots for Orientations I and II. In this case, in both Orientation I and II, any presence of hydrogen generally reduces the amount and length of dislocations emitted for most of the plastic strain range, the lowest being at a concentration of 8 at. % H, further suggesting that hydrogen generally suppresses dislocation emission. This observation, along with hydrogen delaying dislocation emission when using this potential, marks a divergence from the HELP mechanism, particularly when contrasted with the results obtained under the previous set of boundary conditions. Specifically, in the range of approximately 0.09 to 0.1 strain, Orientation I with 1 at. % H exhibits a spike in dislocation density that surpasses the base Fe-C system. Even if the base Fe-C system yields and starts emitting dislocations earlier that the systems with hydrogen, it maintains structural integrity for longer until

it reaches a higher fracture strain, contrary to the system with 1 at. % H which exhibits fracture soon after yielding. Thus, the latter shows higher dislocation emission within a narrower strain range. Figure 55 provides a visual comparison of simulation snapshots, showcasing dislocation behavior of all systems at varying strains for Orientation I, and at a consistent strain for Orientation II. They visually confirm the trend discussed before, showing a general decrease in the quantity and length of dislocations as the hydrogen concentration is increased. Phase transformation remains limited with this potential, as expected, due to the generally lower stress levels reached. Figures 56-58 present the relative phase distributions for Orientations I, II, and III respectively. Orientation I seemingly does not exhibit any phase transformation, and Orientations II and III do show phase transformation at the highest concentration of 8 at. % H indicating, in this case, that the presence of hydrogen can enhance phase transformation in these orientations. This markedly shows the influence of the boundary conditions, especially in Orientation III, as the previous results with the periodic boundary condition in all axes suggest that, overall, hydrogen does not promote BCC to FCC/HCP phase transformation.

As with Case 1, plastic deformation marks the initiation of vacancy formation. Figure 59 presents the vacancy formation plots for all orientations. In Orientations I and II, the incorporation of hydrogen appears to produce a more pronounced increase in vacancy formation before fracture. However, this effect appears to be capped at a certain hydrogen concentration, as the highest tested concentration of 8 at. % does not increase the vacancies formed when compared to the base Fe-C system. Orientation III demonstrates minimal disparities between the models. Nonetheless, the overarching trend suggests that hydrogen typically augments vacancy formation under strain, reinforcing the notion of the HESIV mechanism being at play, even if it seems that the increase in vacancy formation does not follow a somewhat linear relation with the hydrogen concentration.

As such, these results point again to HESIV as seemingly having the largest role in the final fracture of the systems, as voids are formed due to the accumulation of vacancies.

As observed so far, the single-crystalline simulations do help in gaining initial insights. Nonetheless, there are many factors that can play a role in the results, namely the orientations, boundary conditions and potentials used. For example, initially the all-periodic boundary conditions prevented the systems from reaching fracture, and even if the presence of hydrogen increased the formation of vacancies and affected the dislocation emission, their effect on the plastic region of the stress-strain response remained unclear. This was circumvented by implementing the shrink-wrapped boundary condition in the Y direction, which permitted fracture to occur and allowed better observations of the effects of HESIV. The subsequent case (Case 3) introduces two bicrystalline models to add complexity through the inclusion of a GB as an effort to introduce imperfections and hopefully gain more insight into how hydrogen affects the system response. The boundary condition in the Y direction will be kept as shrink-wrapped, anticipating fracture. Fully periodic boundary conditions were not employed, as the intent was to induce and closely analyze the fracture within the models, especially now with the presence of a GB.

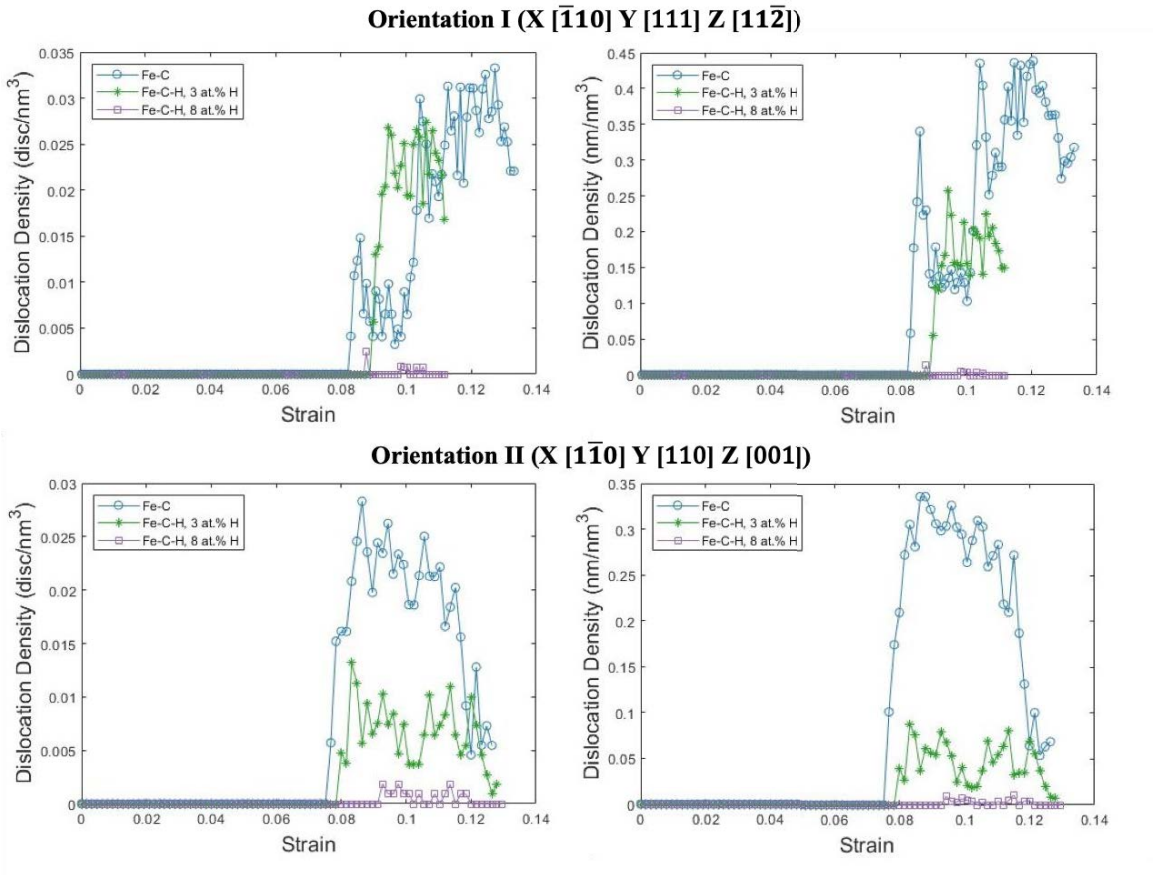

Figure 54 – Plots depicting dislocation density with increasing strain for all orientations.

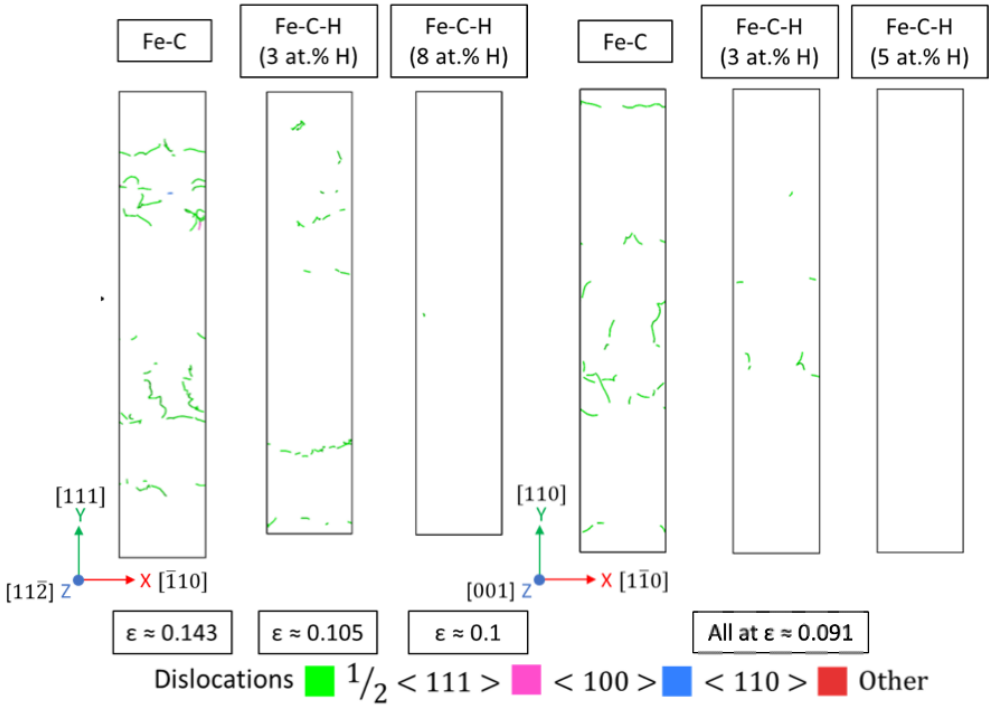

Figure 55 – Simulation snapshots comparing dislocation formation at various strains in Orientation I and at the same strain in Orientation II.

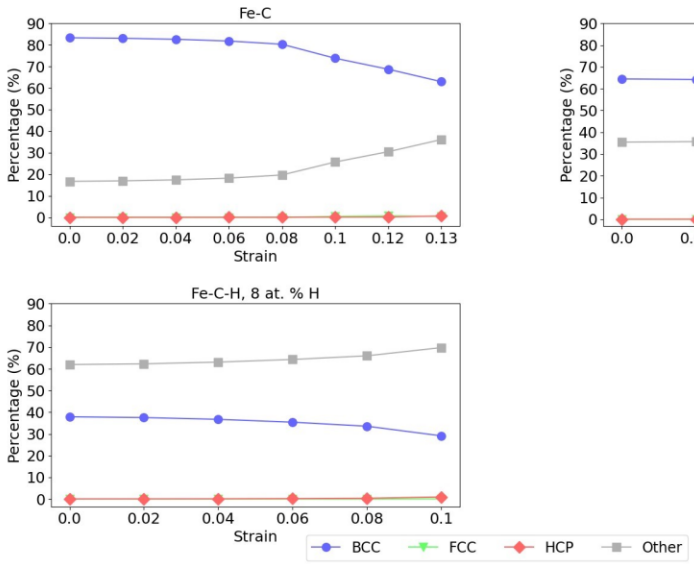

Figure 56 – Plots depicting the relative distribution of the structural phases with strain for Orientation I (X [$\bar{1}$10] Y [111] Z [11$\bar{2}$]).

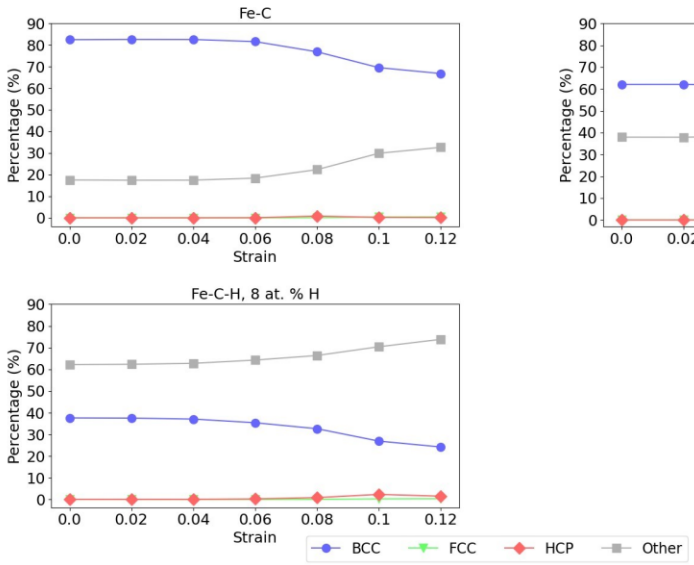

Figure 57 – Plots depicting the relative distribution of the structural phases with strain for Orientation II (X [1$\bar{1}$0] Y [110] Z [001]).

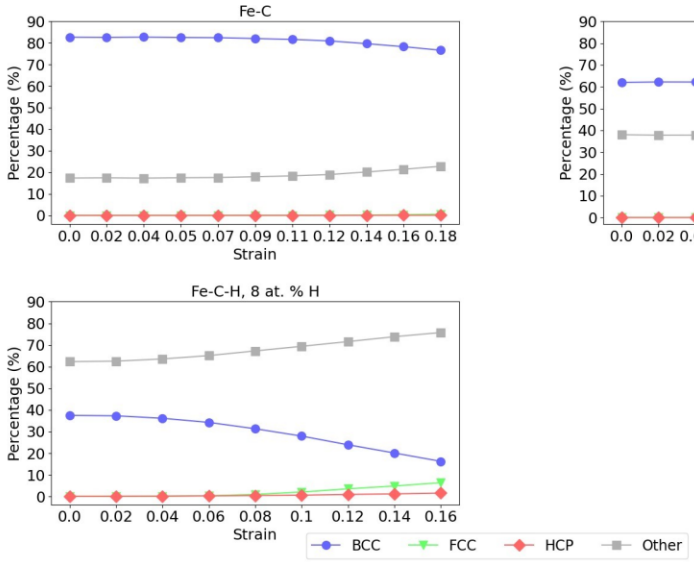

Figure 58 – Plots depicting the relative distribution of the structural phases with strain for Orientation III (X [010] Y [100] Z [001]).

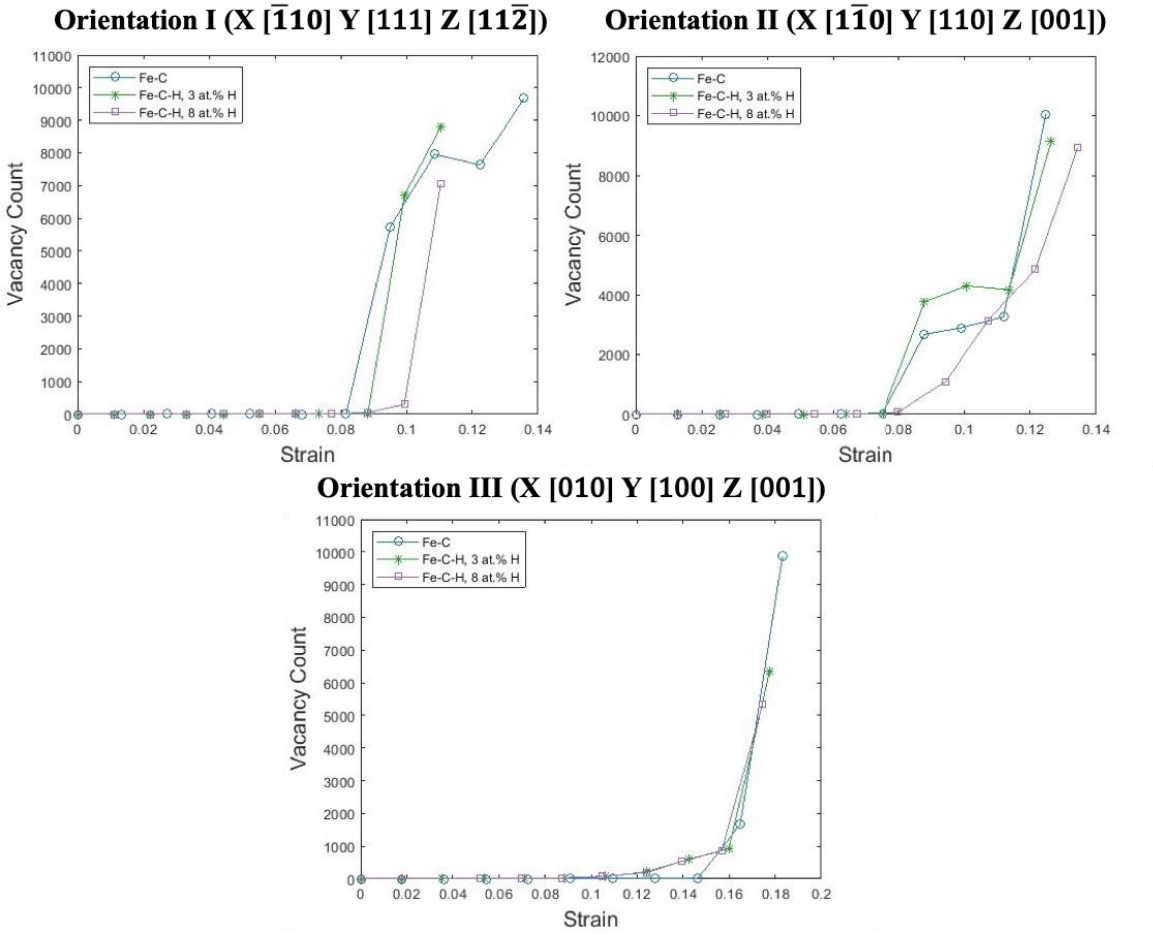

Figure 59 – Plots depicting vacancy count with increasing strain for all orientations.

4.3 Case 3: Bicrystalline with Shrink-Wrap Boundary Condition in Y Axis

For the bicrystalline models, both potentials will be discussed together. Figure 60 illustrates the stress-strain response for the Σ5 and Σ3 systems using both potentials. Figure 61 presents simulation snapshots, at or near fracture, for the Σ5 and Σ3 systems using the BOP. Similarly, Figure 62 shows the same information for the Σ5 and Σ3 systems using the MEAM potential. Table 10 shows the corresponding comparison between the base systems and those with hydrogen, for both Σ5 and Σ3 systems, using both potentials. It is worth mentioning again that the Fe-C-H systems now feature a considerably reduced hydrogen concentration of 100, 150 and 200 wt. ppm, at and around the GB, calculated in respect to the total amount of iron atoms in the system. Starting with the results using the BOP, the Σ5 systems all fracture at the GB. However, the introduction of hydrogen leads to a decrease in both peak stress and strain at the point of fracture. Observing the Σ3 systems, the base Fe-C system does not fail at the GB. Yet, once hydrogen is introduced, the fracture shifts to the GB. The presence of hydrogen at the GB also diminishes the stress and strain at fracture, with the exception of the Fe-C-H system with a hydrogen concentration of 100 wt. ppm, where both stress and strain exhibit a slight increase. This echoes the findings from Matsubara [31], and while that study focused more on misorientations by rotating GBs, it goes to show that hydrogen effect can vary depending on orientations, type of GB and, of course, concentration. The results using the MEAM potential align with what was observed with the BOP, yet the smoother curves and reduced strain at fracture in the presence of hydrogen are clear. In this case, the Σ5 Fe-C system did not fail at the GB. However, when hydrogen was introduced, the fracture did occur at the GB, mirroring a similar effect to the Σ3 Fe-C system using the BOP. In all Σ3 systems, fracture consistently occurs at the GB, with an increase in hydrogen concentration leading to lower stress and strain at the point of fracture. It is important to highlight that the

decrease in fracture stress and strain in both Σ5 and Σ3 systems with hydrogen is significantly more pronounced than the decrease observed with the BOP, suggesting that hydrogen has a more substantial impact with the MEAM potential as the atomic model increases in complexity.

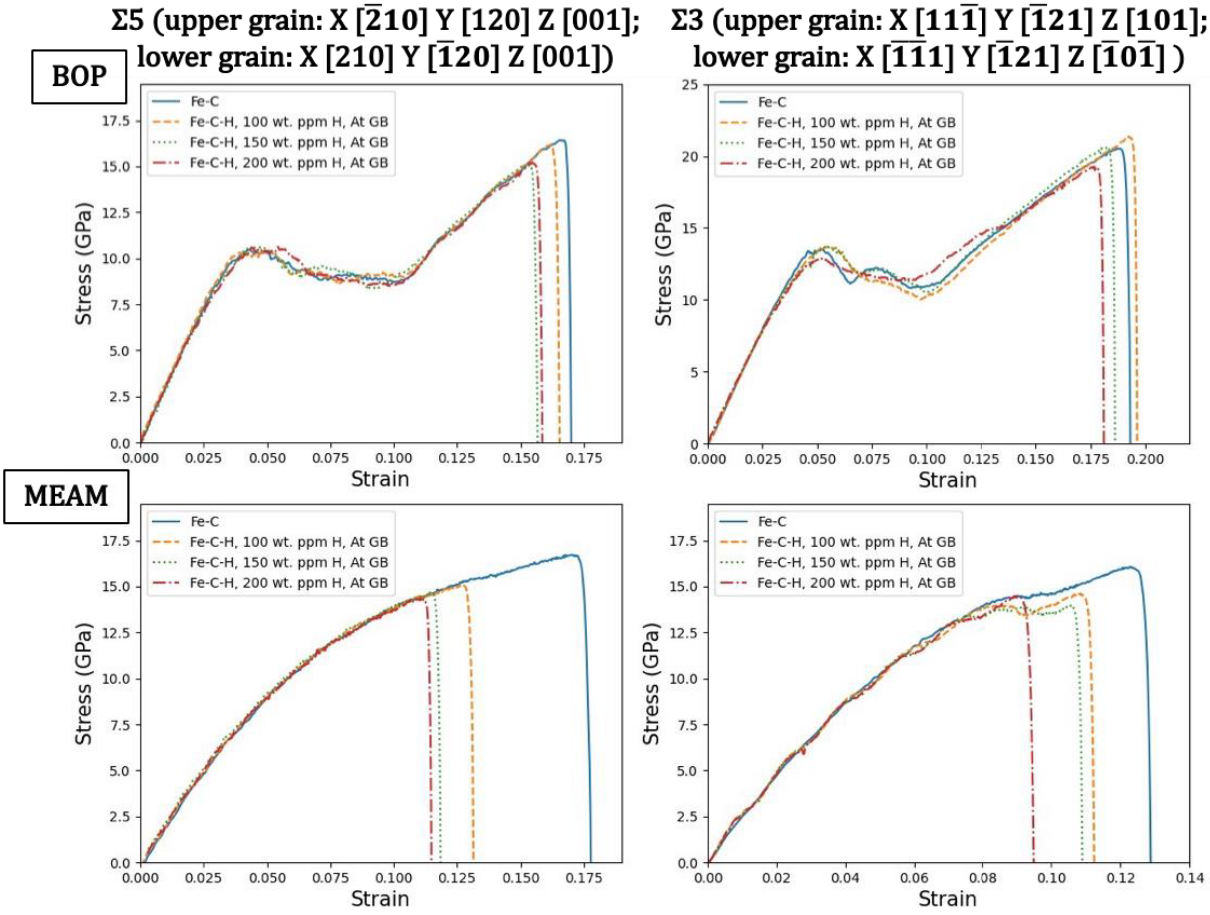

Figure 60 – Plots depicting stress – strain response for the bicrystalline Σ5 and Σ3 systems using both potentials.

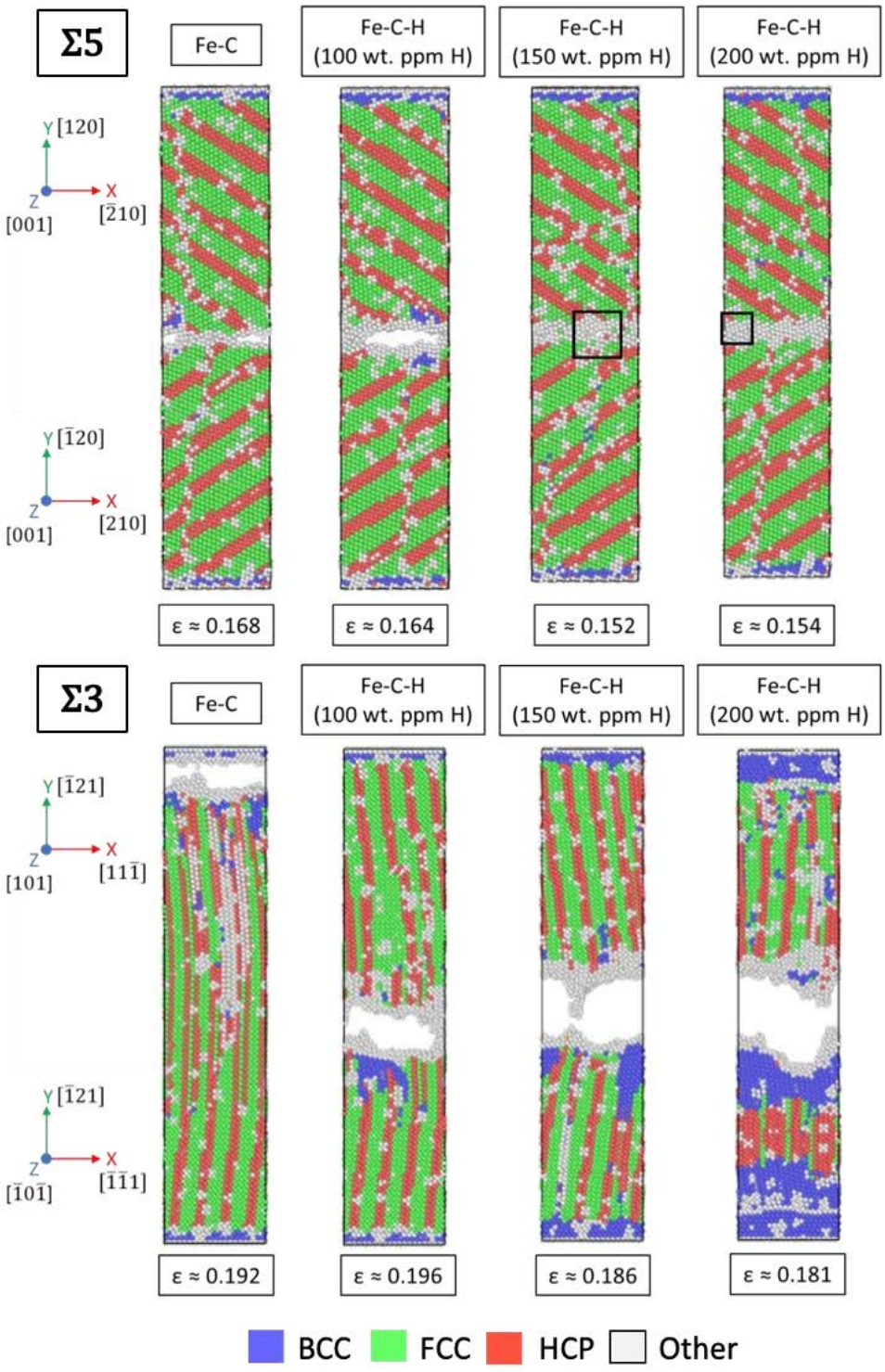

Figure 61 – Simulation snapshots during loading, at or near fracture strain, for the bicrystalline Σ5 and Σ3 systems using the BOP.

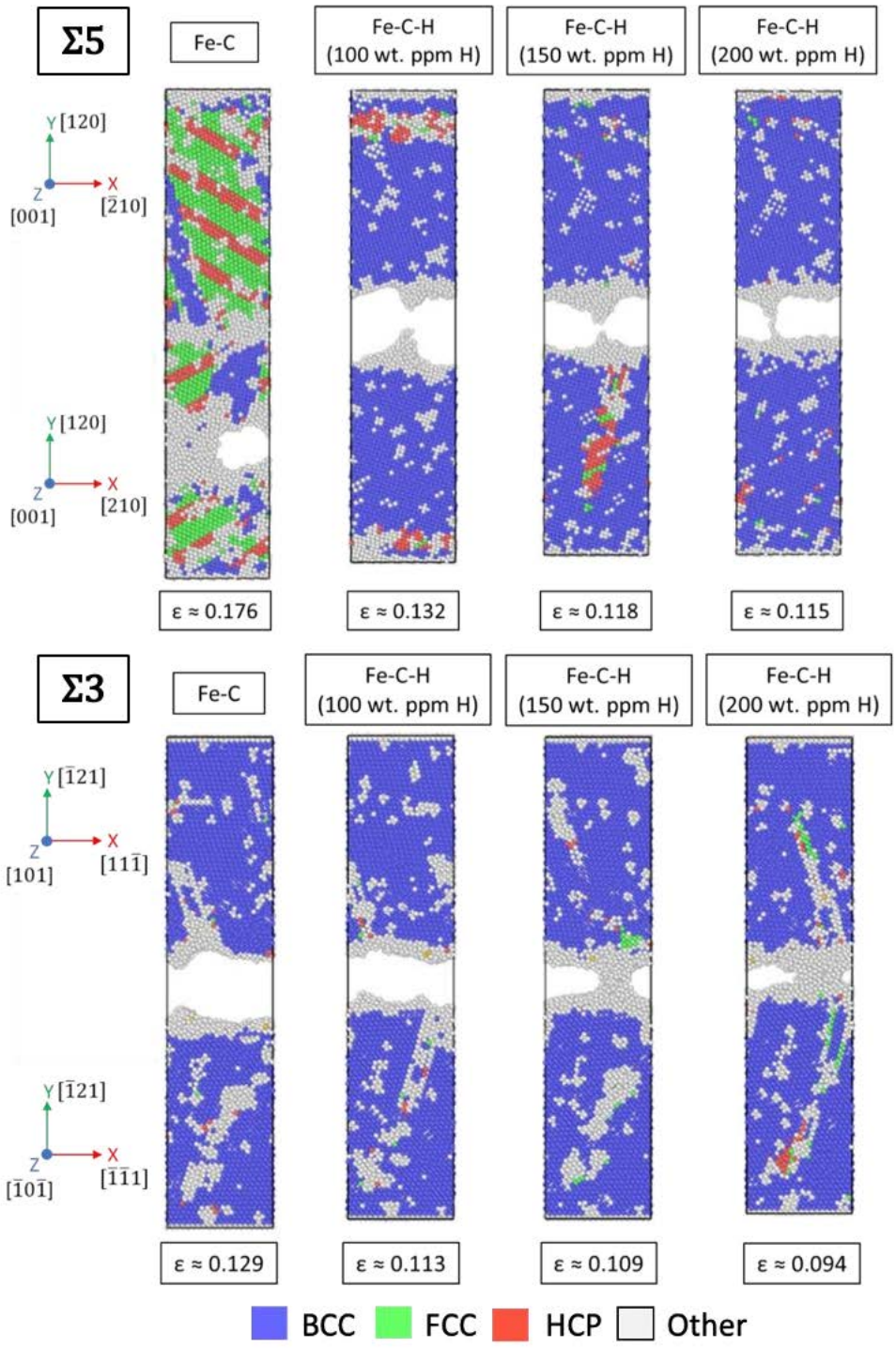

Figure 62 – Simulation snapshots during loading, at or near fracture strain, for the bicrystalline Σ5 and Σ3 systems using the MEAM potential.

Table 10 – Comparison of peak stress and fracture strain for all bicrystalline systems.

Potential	GB Model	System	Peak stress (GPa)	Change (%)	Fracture strain	Change (%)
BOP	Bicrystalline Σ5	Fe-C	16.41	-	0.168	-
		Fe-C-H, 100 wt. ppm H, at GB	16.20	-1%	0.162	-4%
		Fe-C-H, 150 wt. ppm H, at GB	15.10	-8%	0.152	-9%
		Fe-C-H, 200 wt. ppm H, at GB	15.23	-7%	0.155	-8%
	Bicrystalline Σ3	Fe-C	20.58	-	0.19	-
		Fe-C-H, 100 wt. ppm H, at GB	21.35	4%	0.19	2%
		Fe-C-H, 150 wt. ppm H, at GB	20.69	1%	0.18	-3%
		Fe-C-H, 200 wt. ppm H, at GB	19.30	-6%	0.18	-6%
MEAM	Bicrystalline Σ5	Fe-C	16.66	-	0.173	-
		Fe-C-H, 100 wt. ppm H, at GB	15.16	-9%	0.127	-26%
		Fe-C-H, 150 wt. ppm H, at GB	14.71	-12%	0.114	-34%
		Fe-C-H, 200 wt. ppm H, at GB	14.40	-14%	0.110	-36%
	Bicrystalline Σ3	Fe-C	16.11	-	0.123	-
		Fe-C-H, 100 wt. ppm H, at GB	14.66	-9%	0.108	-12%
		Fe-C-H, 150 wt. ppm H, at GB	14.02	-13%	0.106	-14%
		Fe-C-H, 200 wt. ppm H, at GB	14.50	-10%	0.090	-27%

As dislocation emission is not observed in any of the systems, phase transformation seems to be the only yielding initiation mechanism. Figures 63 and 64 illustrate the relative phase distributions for the Σ5 and Σ3 systems, respectively, using the BOP. Figures 65 and 66 show the same using the MEAM potential. A consistent trend seen before emerges again, with the BOP displaying a markedly accelerated phase transformation rate prior to fracture in both absence and presence of hydrogen. The MEAM potential does exhibit more phase transformation this time compared to Case 2, suggesting that its earlier absence of transformation in the single-crystalline model with shrink-wrapped boundary conditions might be attributed to the lack of imperfections, in this case

the GB. However, the MEAM potential always demonstrates less transformation than the BOP. Furthermore, the introduction of hydrogen seems to reduce the likelihood of transformation, but in the sense that fracture occurs at the GB before more transformation can take place, even though some transformation is still evident, especially in the Σ5 system. Notably, the structure reverts mostly back to BCC once the fracture happens, as the load is released, suggesting that this transformation is not permanent. To study the effect that carbon has on phase transformation, Figure 67 illustrates how carbon atoms act as potential nucleation sites for the BCC to FCC/HCP transformation, by comparing an Fe system with an Fe-C system using the BOP. In the Fe system, the phase transformation predominantly originates at the GB, like studied by Ma et al. [112], as a mechanism for energy release as previously discussed. Conversely, while the Fe-C system also showcases transformation at the GB, simultaneous transformations occur at specific locations where C atoms are present. This underscores the notion that C atoms serve as nucleation sites for phase transformation [107].

As observed in Cases 1 and 2, the plastic region marks the initiation in vacancy formation. Figure 68 illustrates vacancy formation for the Σ5 and Σ3 systems using both potentials. Going further, Figure 69 shows the vacancy sites (specially at the GB) formed at or around fracture strain, for both Σ5 and Σ3 systems, using the MEAM potential. These are complemented by Table 11, which includes a comparison of all the systems with hydrogen against the Fe-C system, measuring the vacancies formed at and near GB for both potentials. Although the trend may exhibit some variability, similar to specific orientations in single-crystalline models, the general observation is that the introduction of hydrogen augments the creation of these vacancies. Notably, this occurs at a much lower concentration than what was previously discussed in single-crystalline systems. It is worth noting how the presence of hydrogen at the GB in Figure 69 increases the number of

vacancies formed locally at the same strain level, as seen in Case 2, where the accumulation of vacancies around the hydrogen atoms was observed. Interestingly, the highest hydrogen concentration does not always correlate with a proportional increase in local vacancy formation, and it seems capped at the hydrogen concentration of 150 wt. ppm. This suggest that this concentration limit might be around the mentioned concentration. Nonetheless, this pattern implies that hydrogen, through the HESIV mechanism, promotes void generation and coalescence at the GB, leading to fracture, as discussed by Xing et al. [99] and other experimental studies [71], [73], [75], [76], [95]. Also, the HEDE mechanism could be at play due to the reduction in cohesive energy at the GB [14], [71]–[73]. However, these simulations do not provide direct evidence to support this hypothesis. The potential involvement of this mechanism could suggest a synergistic relationship between the HESIV and HEDE mechanisms, the two contributing to fracture. This is similar to what is proposed both experimentally and with simulations by Matsubara [31], in the way of the crack propagating by interlinking isolated failures. Similarly, Ogawa et al. [95] and Tomatsu et al. [73] experimentally observe that failure can result from the expansion and linkage of isolated microcracks, accompanied by microvoid formation at the GB, even if HELP is also proposed as one of the mechanisms at play (particularly in the transport of hydrogen to the GB), which is not observed in these results.

In the concluding scenario, Case 4, a transition to a polycrystalline model is made, significantly elevating the level of complexity by incorporating multiple GBs. Similar to Cases 2 and 3, the boundary condition in the Y direction will remain shrink-wrapped. As mentioned throughout, this specific condition is consistently chosen to facilitate the occurrence of fractures, a critical aspect of the study, particularly in the inherently complex polycrystalline structures. The introduction of these conditions aims to provide deeper insights into how fractures propagate in materials with

multiple GBs, thereby enhancing our understanding of material failure mechanisms in more complex systems. Emphasis was given to the MEAM potential through the examination of various hydrogen concentrations, as the reduced energy release from phase transformation provides clearer insights into the impacts of hydrogen.

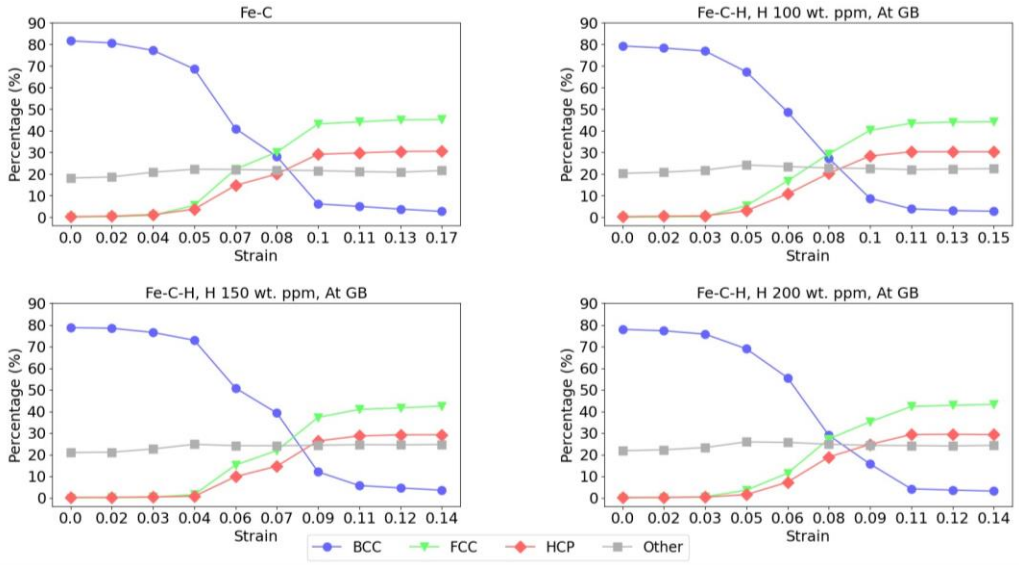

Figure 63 – Plots depicting the relative distribution of the structural phases with strain for the bicrystalline Σ5 systems using the BOP.

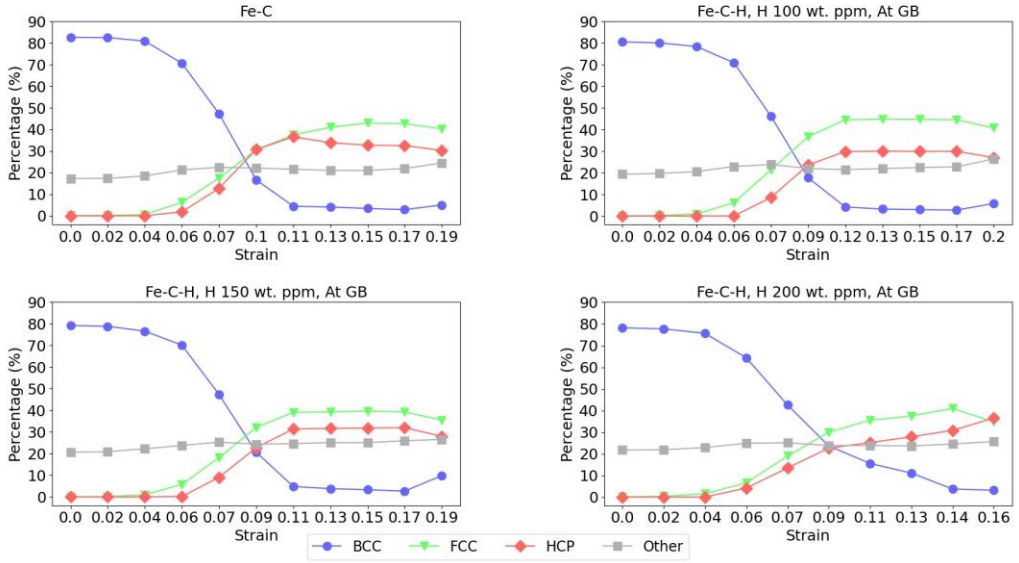

Figure 64 – Plots depicting the relative distribution of the structural phases with strain for the bicrystalline Σ3 systems using the BOP.

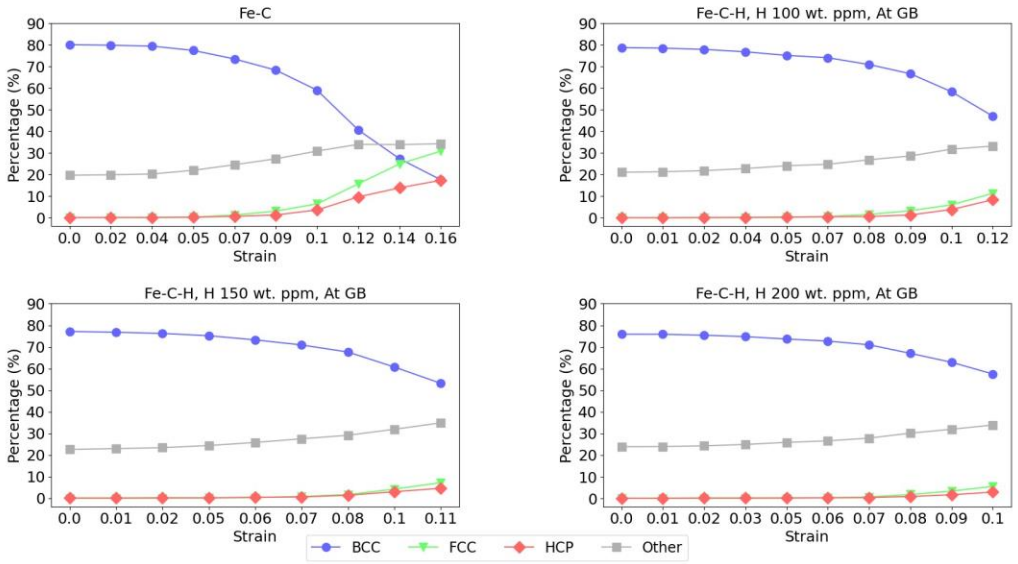

Figure 65 – Plots depicting the relative distribution of the structural phases with strain for the bicrystalline Σ5 systems using the MEAM potential.

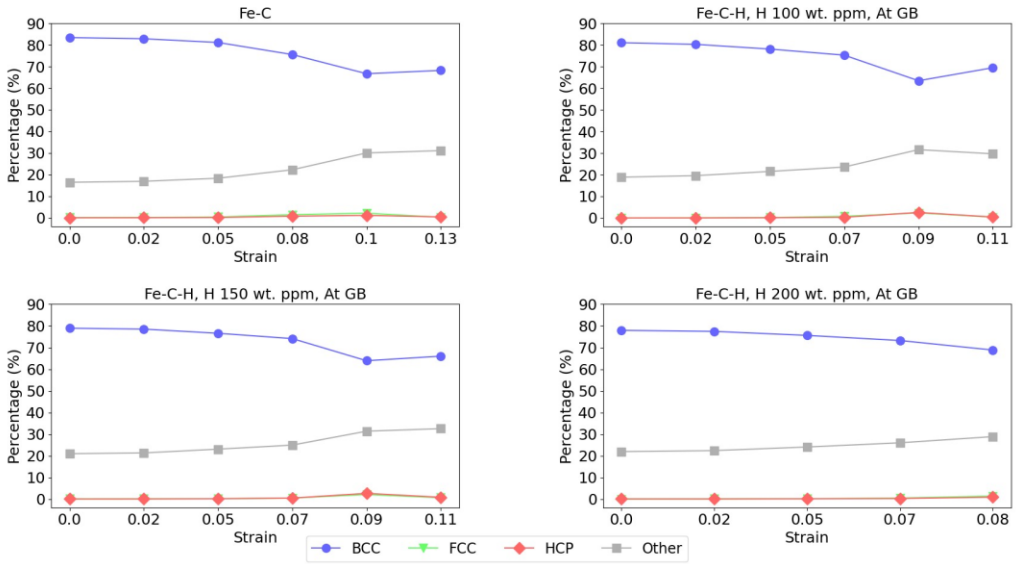

Figure 66 – Plots depicting the relative distribution of the structural phases with strain for the bicrystalline Σ3 systems using the MEAM potential.

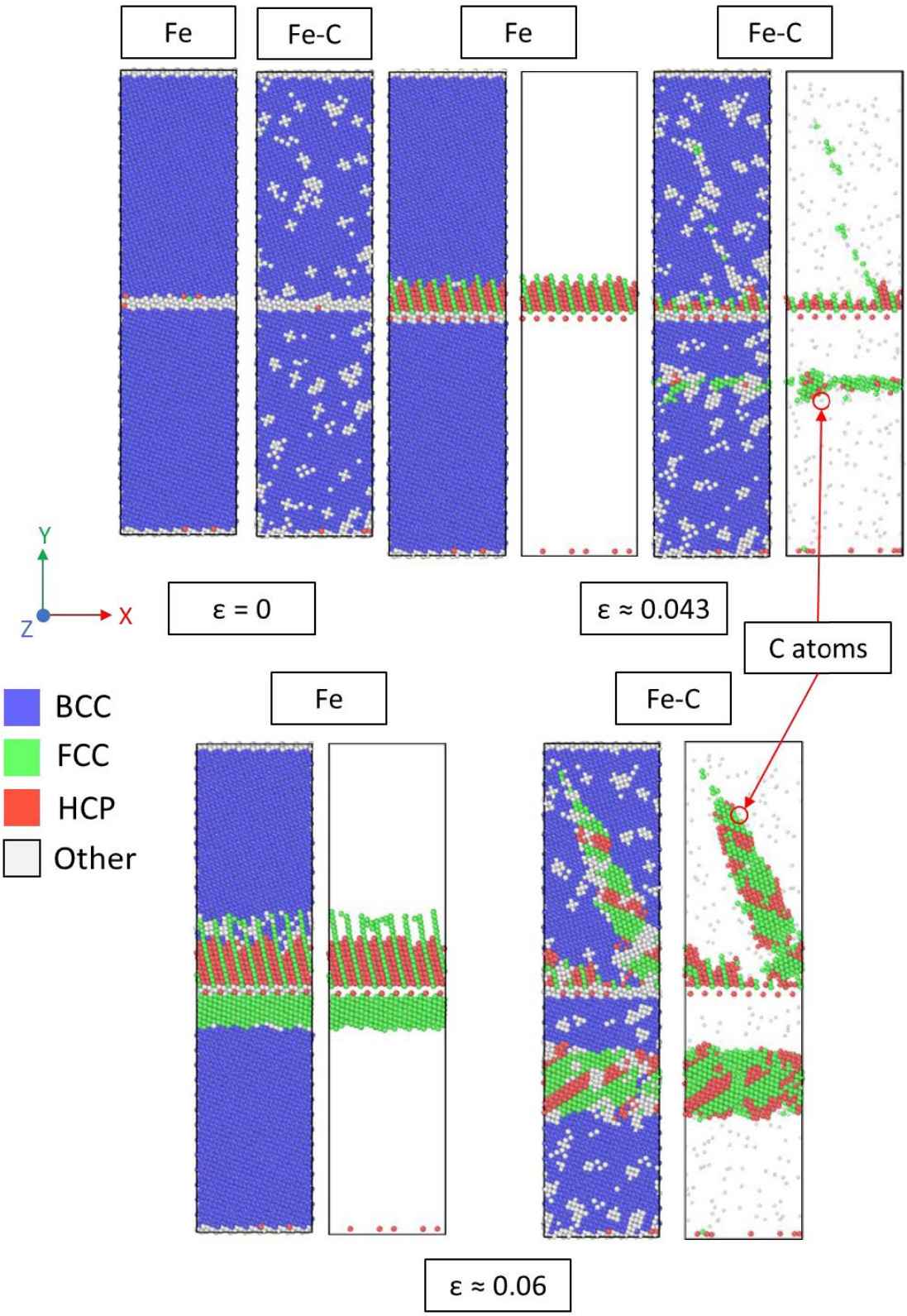

Figure 67 – Snapshots taken on bicrystalline Σ5 Fe and Fe-C systems using the BOP. Note how carbon atoms serve as nucleation sites for phase transformation.

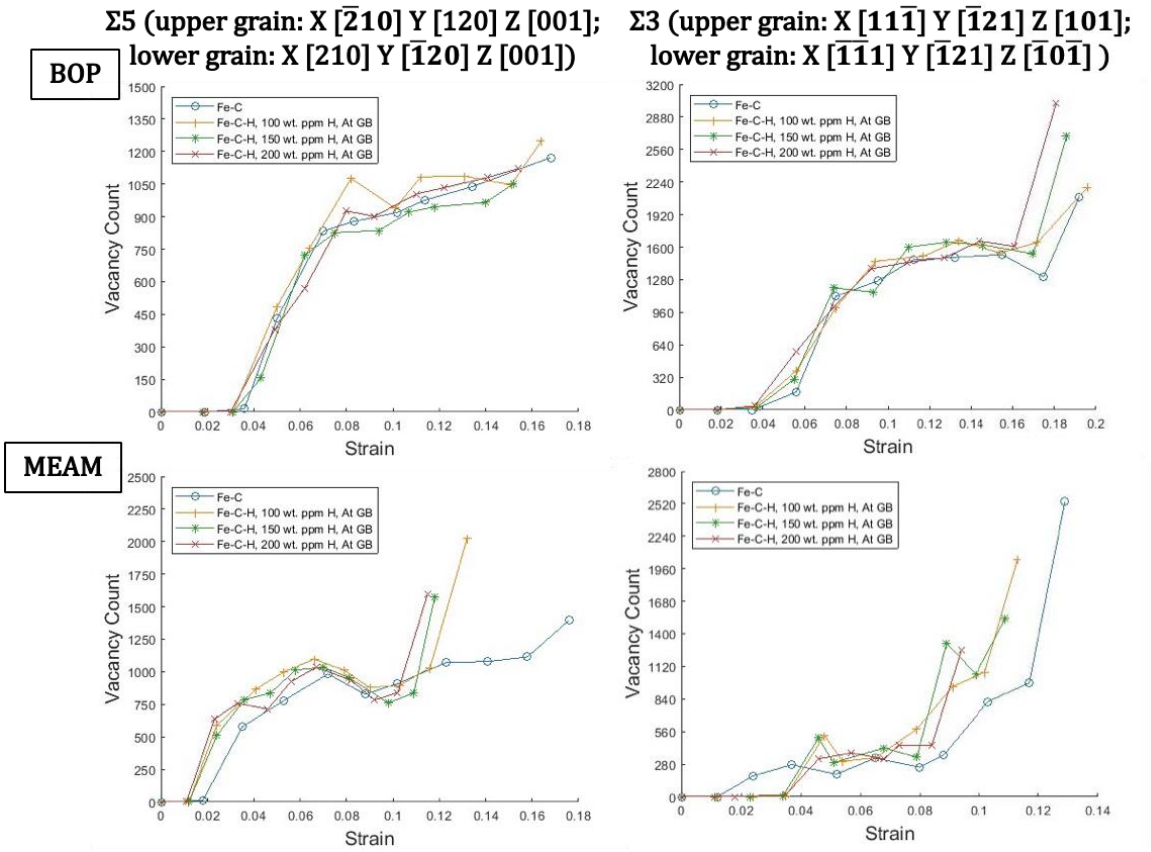

Figure 68 – Plots depicting vacancy count with increasing strain for the bicrystalline Σ5 and Σ3 systems using both potentials.

Table 11 – Comparison of vacancies near or at the GB and total vacancies for all bicrystalline systems at fracture strain.

Potential	GB model	System	Vacancies near and at GB	Change (%)
BOP	Bicrystalline Σ5	Fe-C	151	-
		Fe-C-H, 100 wt. ppm H, at GB	180	19.2%
		Fe-C-H, 150 wt. ppm H, at GB	163	7.9%
		Fe-C-H, 200 wt. ppm H, at GB	187	23.8%
	Bicrystalline Σ3	Fe-C	88	-
		Fe-C-H, 100 wt. ppm H, at GB	190	115.9%
		Fe-C-H, 150 wt. ppm H, at GB	230	161.4%
		Fe-C-H, 200 wt. ppm H, at GB	200	127.3%
MEAM	Bicrystalline Σ5	Fe-C	136	-
		Fe-C-H, 100 wt. ppm H, at GB	193	41.9%
		Fe-C-H, 150 wt. ppm H, at GB	198	45.6%
		Fe-C-H, 200 wt. ppm H, at GB	181	33.1%
	Bicrystalline Σ3	Fe-C	70	-
		Fe-C-H, 100 wt. ppm H, at GB	98	40.0%
		Fe-C-H, 150 wt. ppm H, at GB	217	210.0%
		Fe-C-H, 200 wt. ppm H, at GB	120	71.4%

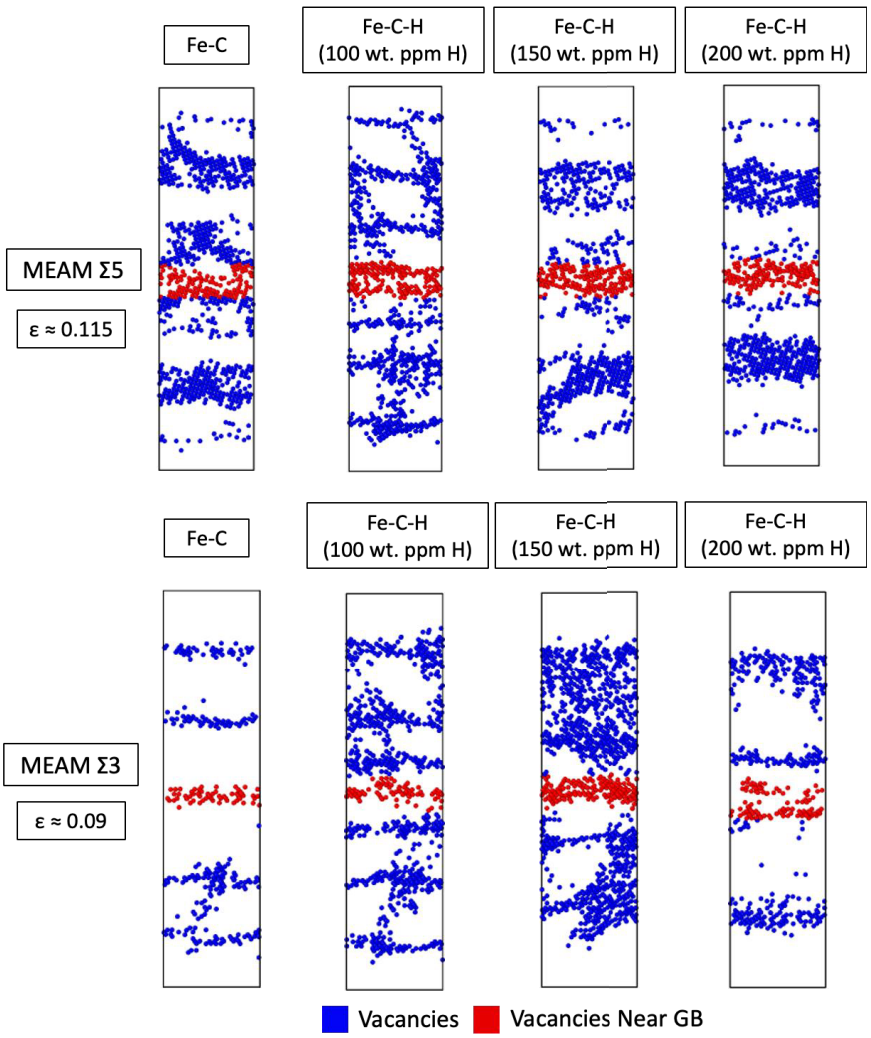

Figure 69 – Visualization of vacancies at fracture strain for both bicrystalline Σ5 and Σ3 systems using the MEAM potential. The blue spots correspond to vacancy sites, red spots to vacancies near the GB.

4.4 Case 4: Polycrystalline with Shrink-Wrap Boundary Condition in Y Axis

4.4.1 Bond Order Potential

Figure 70 illustrates the stress-strain response for the polycrystalline systems. Table 12 compares the systems by measuring the peak stress obtained and the strain at fracture. Figure 71 shows simulation snapshots at the considered failure point (initiation of fracture) of all systems. Hydrogen located within the grain appears to have a lesser impact, whereas hydrogen at the GB and randomized exert a pronounced influence under these conditions. Hydrogen at the GB even

slightly shifts the failure initiation point compared to the Fe-C system and the other two hydrogen distributions, although it remains within a proximate area. It is notable how the phase transformation bands vary between grains because, as mentioned throughout, this transformation favors {110} planes [94], [113] which are relatively oriented differently in each grain.

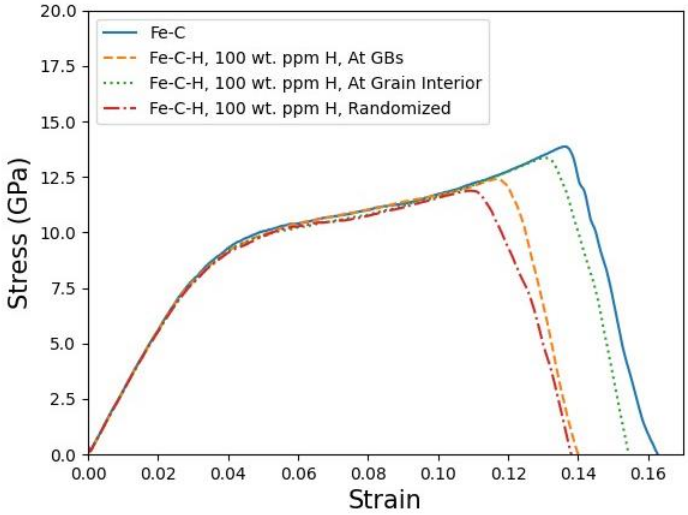

Figure 70 – Plot depicting stress - strain response for the polycrystalline systems.

Table 12 – Comparison of peak stress and fracture strain for all polycrystalline systems.

System	Peak stress (GPa)	Change (%)	Fracture Strain	Change (%)
Fe-C	13.88	-	0.136	-
Fe-C-H, 100 wt. ppm H, at GB	12.43	-10%	0.117	-14%
Fe-C-H, 100 wt. ppm H, at GI	13.37	-4%	0.130	-4%
Fe-C-H, 100 wt. ppm H, Randomized	11.89	-14%	0.109	-20%

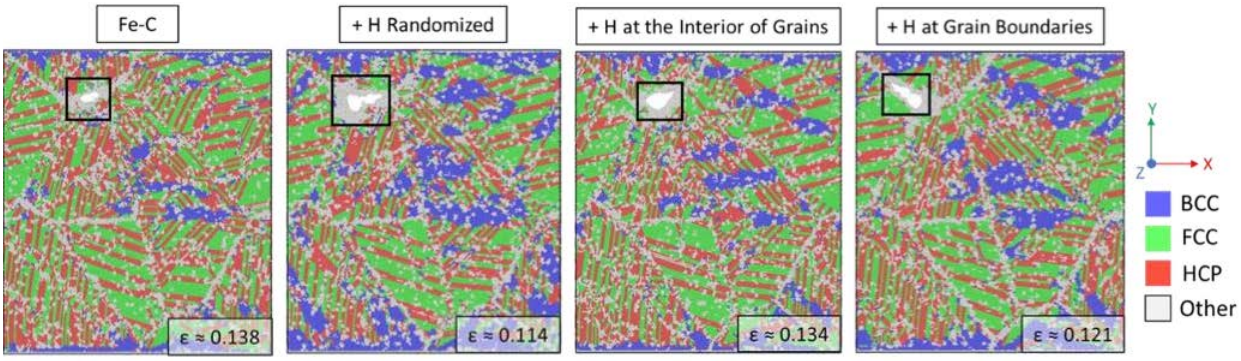

Figure 71 – Simulation snapshots during loading, at fracture strain, for the polycrystalline systems. Hydrogen concentration of 100 wt. ppm.

For these polycrystalline systems, the yielding initiation mechanisms seems to be solely phase transformation, as no dislocations are emitted in any of the systems. Figure 72 illustrates the relative phase distributions for all systems. There is virtually no change in the phase transformation across all models if observed at the same strain level, either pointing away from hydrogen aiding phase transformation or the hydrogen concentration is not high enough to see any effect. Yield is observed to occur around the same strain for all models, indicating that at this concentration, the presence of hydrogen does not seem to cause earlier yielding.

As observed so far, the plastic region marks the start of vacancy formation. Figure 73 illustrates vacancy formation across all the systems, which seems to increase when hydrogen is present. Even with uniform concentrations, vacancy formation displays variability, suggesting that hydrogen location plays an important role. As such, as with Cases 2 and 3, hydrogen can be the inferred cause for the local accumulation of vacancies, eventually forming larger voids and the initiation of fracture. Building on these insights, a possible synergistic interaction between HESIV and HEDE mechanisms can be once again suggested, which leads to enhanced local vacancy creation, an increase in local voids, and a reduction in cohesive strength at the GBs. Once more, such observations align with the findings reported by Matsubara [31], Ogawa et al. [95] and Tomatsu et al. [73] and Xing et al. [99].

The final set of results, utilizing the MEAM potential with this polycrystalline model, delves deeper by increasing hydrogen concentration and presenting figures that illustrate the formation of vacancies. This culminates the results and discussion section and transitions into the concluding chapter, providing an overview and synthesis of the findings.

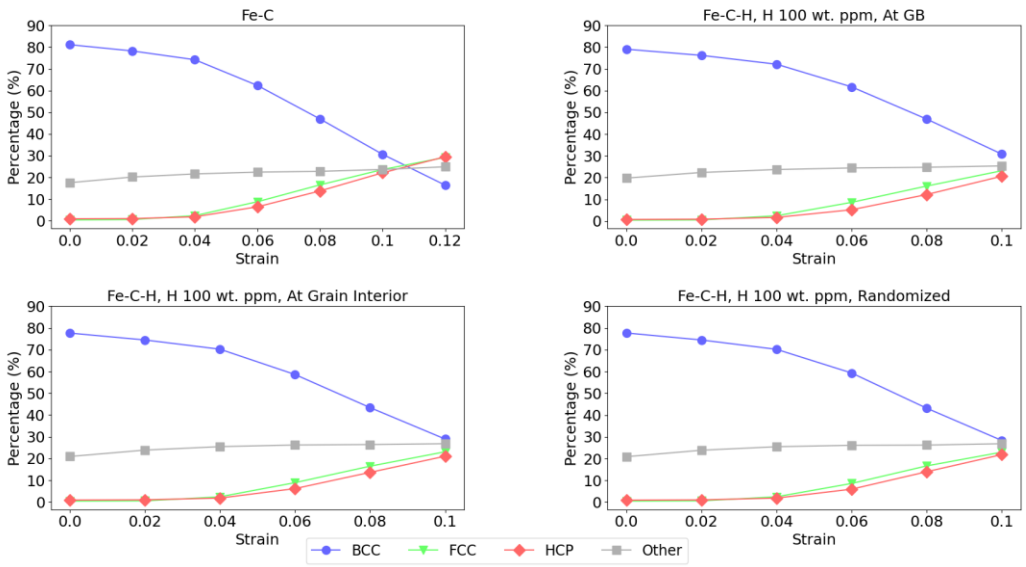

Figure 72 – Plots depicting the relative distribution of the structural phases with strain for the polycrystalline systems. Hydrogen concentration of 100 wt. ppm.

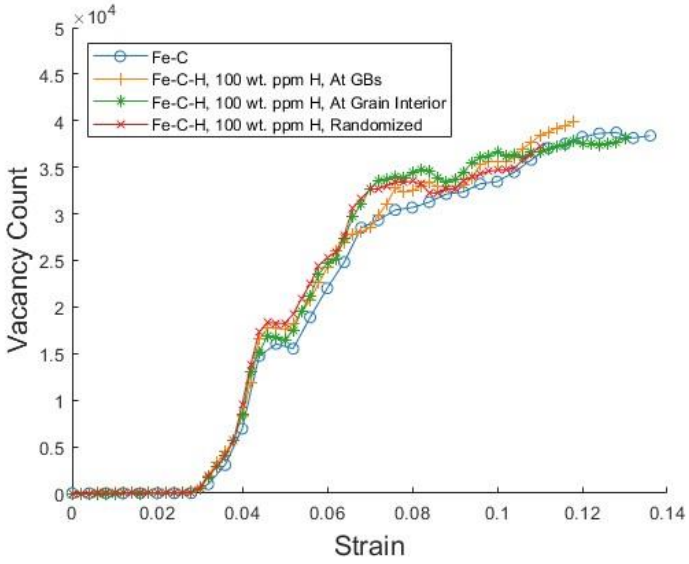

Figure 73 – Plot depicting vacancy count with increasing strain for the polycrystalline systems. Hydrogen concentration of 100 wt. ppm.

4.4.2 Modified Embedded Atom Method

Figure 74 depicts the stress-strain responses of the base Fe-C system against varying hydrogen concentrations of 100, 150, and 200 wt. ppm at the different locations. Table 13 provides a comparative analysis of the hydrogen-free model with hydrogen-containing models. Figure 75 presents simulation snapshots at fracture strain of the base system and systems with the

aforementioned hydrogen concentrations and locations. Hydrogen located in at random positions was only run for 100 wt. ppm, the other two locations for all concentrations (100, 150 and 200 wt. ppm). Contrary to expectations based on results with the BOP, there is no observed reduction of mechanical properties in the presence of randomized hydrogen; rather, the model with hydrogen slightly elevates the peak stress and fracture strain. Hydrogen placed at the interior of the grains slightly reduces the peak stress and strain, but not by much. Only the hydrogen placed at the GBs have a greater effect. Also, hydrogen placed at the interior of the grains and at the GBs shift the point of fracture to the upper left, but hydrogen at the GBs makes the fracture happen at a lower strain. Interestingly, the fracture point in the system without hydrogen is singular, but in the system with randomized hydrogen, fracture begins to manifest in a second location (in the same general upper left area). Phase transformation is limited with this potential as compared to the BOP, as expected at this point. The findings from the polycrystalline model suggest that the MEAM potential is better suited for studying hydrogen effects in larger and more complex models, based on the impact that hydrogen has in shifting the point where the fracture starts. This is attributed to the reduced phase transformations by reducing the associated energy release.

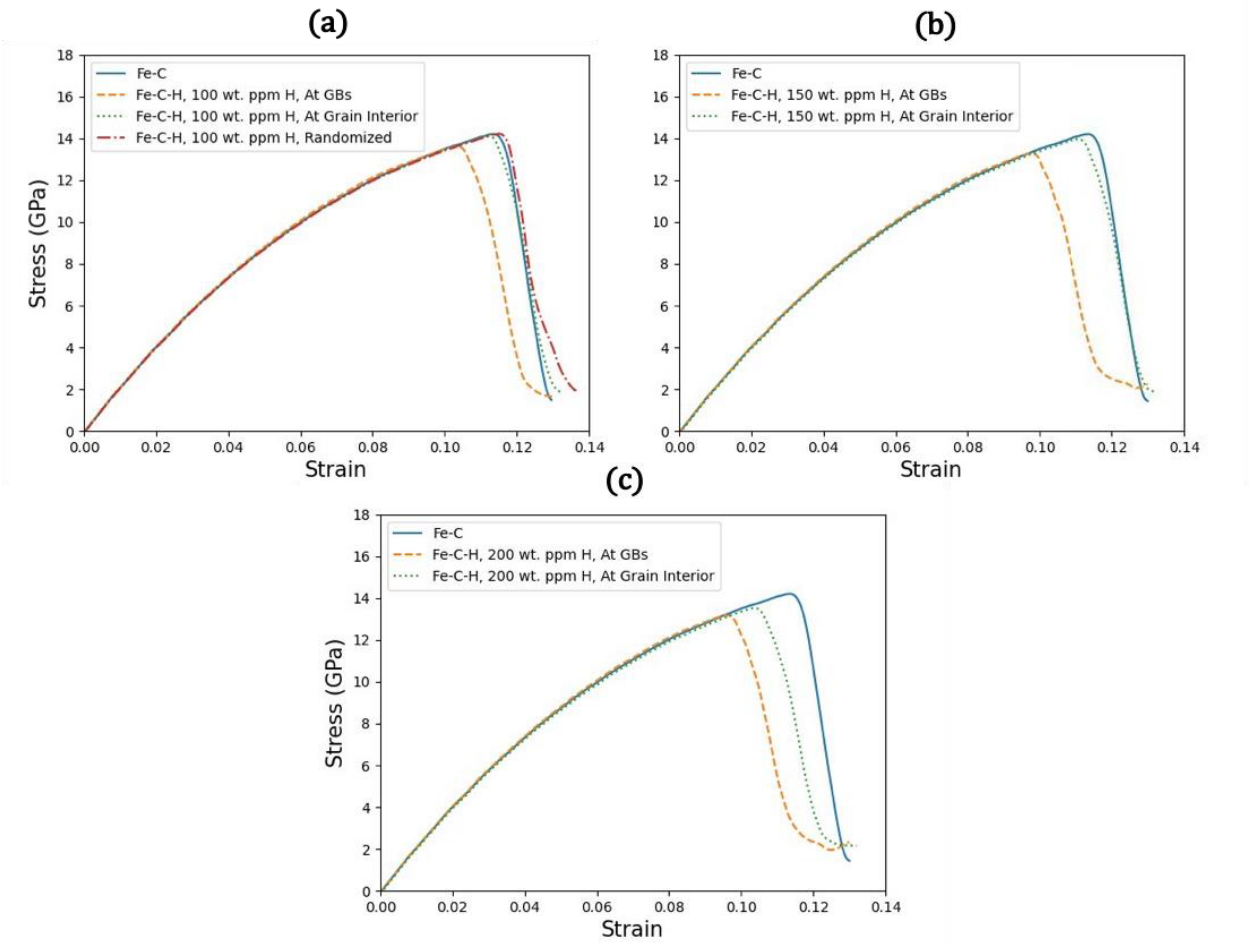

Figure 74 – Plots depicting stress - strain response for the polycrystalline systems at different hydrogen concentrations: (a) 100 wt. ppm., (b) 150 wt. ppm. and (c) 200 wt. ppm.

Table 13 – Comparison of peak stress and fracture strain for all polycrystalline models.

System	Peak stress (GPa)	Change (%)	Fracture Strain	Change (%)
Fe-C	14.21	-	0.113	-
Fe-C-H, 100 wt. ppm H, at GB	13.61	-4%	0.103	-9%
Fe-C-H, 100 wt. ppm H, at GI	14.13	-1%	0.112	-1%
Fe-C-H, 100 wt. ppm H, Randomized	14.23	0.15%	0.115	1%
Fe-C-H, 150 wt. ppm H, at GB	13.30	-6%	0.098	-14%
Fe-C-H, 150 wt. ppm H, at GI	13.97	-2%	0.111	-2%
Fe-C-H, 200 wt. ppm H, at GB	13.19	-7%	0.096	-15%
Fe-C-H, 200 wt. ppm H, at GI	13.53	-5%	0.104	-9%

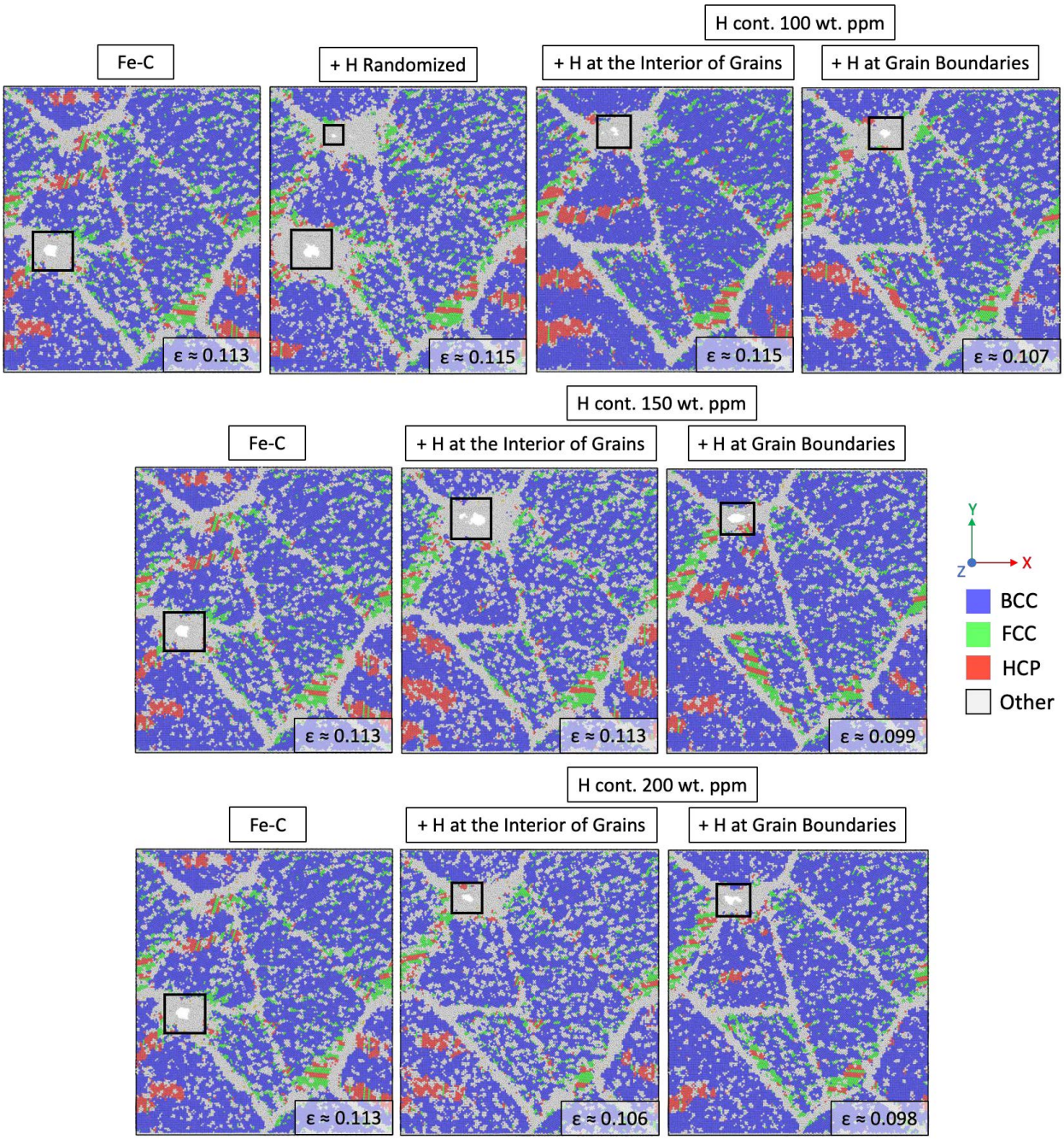

Figure 75 – Simulation snapshots during loading, at fracture strain, for the polycrystalline systems.

For yielding, phase transformation plays the primary role, as dislocation emission, though present, contributes minimally. Figures 76-78 illustrate the dislocation density plots for the base Fe-C and the Fe-C-H system with hydrogen concentrations of 100, 150, and 200 wt. ppm respectively. Overall, the same trend of hydrogen inhibiting dislocation emission is followed. Hydrogen located

at the interior of the grains seems to generate more dislocations as compared to hydrogen located at the GBs (which is observed to suppress dislocations the most) plus the highest dislocation emission is both at a hydrogen concentration of 100 and 200 wt. ppm, even surpassing the base Fe-C system continuously. Nonetheless, the overall number of dislocations formed is very low, as shown in Figure 79. In general, these results can suggest that the location of hydrogen has an effect on dislocation emission. Figures 80-82 illustrate the relative phase distributions for the base Fe-C system against the Fe-C-H systems with varying hydrogen concentrations of 100, 150, and 200 wt. ppm at the different locations, respectively. This illustration reveals no significant alterations in phase transformation across systems, mirroring the observations made in the preceding polycrystalline models with the BOP. Nonetheless, using the MEAM potential, hydrogen at the GBs seem to slightly increase the phase transformation, suggesting that the location of hydrogen can have a role in the transformation, even if just slightly. Nonetheless, all systems virtually yield at the same strain.

Inside the plastic range, Figure 83 illustrates vacancy formation across all the systems, comparing the base Fe-C system against varying hydrogen concentrations of 100, 150, and 200 wt. ppm at the different locations. In these instances, the presence of hydrogen appears to make virtually no increase, in general, to the total number of vacancies formed, but do increase the local formation for vacancies. Nonetheless, increasing the hydrogen concentration does indeed increase the number of vacancies formed in a significant portion of the strain range, surpassing the base Fe-C system. Also, hydrogen located at the interior of the grains seems to constantly form more vacancies under strain when compared to hydrogen at the GBs, but the latter fails at a lower strain, pointing out to HESIV increasing the local number of vacancies and eventually forming larger voids that lead to failure. As discussed so far, a possible synergistic effect of HESIV and HEDE

exist by increasing the local vacancy formation, generating more local voids, and lowering the cohesive strength at GBs. Increasing hydrogen concentration naturally accentuates the effects. This further supports observations made by Matsubara [31], Ogawa et al. [95] and Tomatsu et al. [73] and Xing et al. [99]. Similar to findings in Cases 2 and 3, Figure 84 depicts snapshots showing the vacancy formation for the Fe-C system and Fe-C-H system with the highest hydrogen concentration (200 wt. ppm), at different strains, having the approximate contour of the GBs included. It clearly shows the increase in the local vacancy formation (promoting HESIV) both in the systems with hydrogen at the GBs and at the interior of the grains, even if the total number of vacancies is less at some strains. This supports the results observed on the bicrystalline systems in Case 3, as the fracture origin can shift to the GB once hydrogen is present. This local increase in local vacancy formation is very evident at the fracture point.

The last chapter, Chapter 5, serves as the culmination of this thesis, providing a comprehensive recapitulation of the key findings and implications derived from the study. Additionally, this final chapter delves into potential steps for future research, wrapping up the discussion on this academic subject.

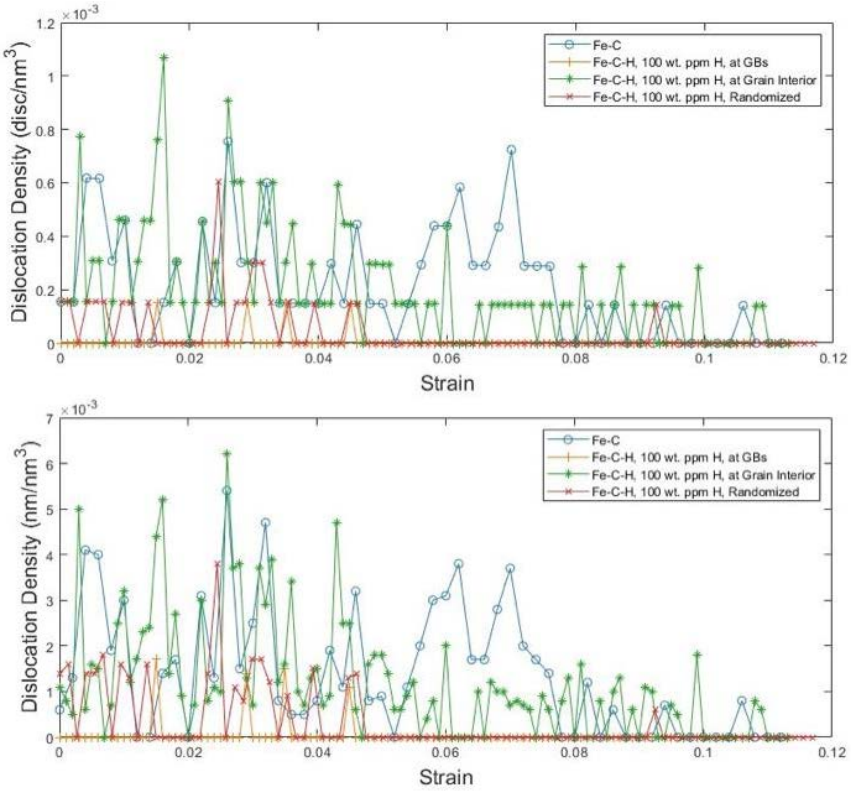

Figure 76 – Plots depicting dislocation density with increasing strain for the polycrystalline systems. Hydrogen concentration of 100 wt. ppm.

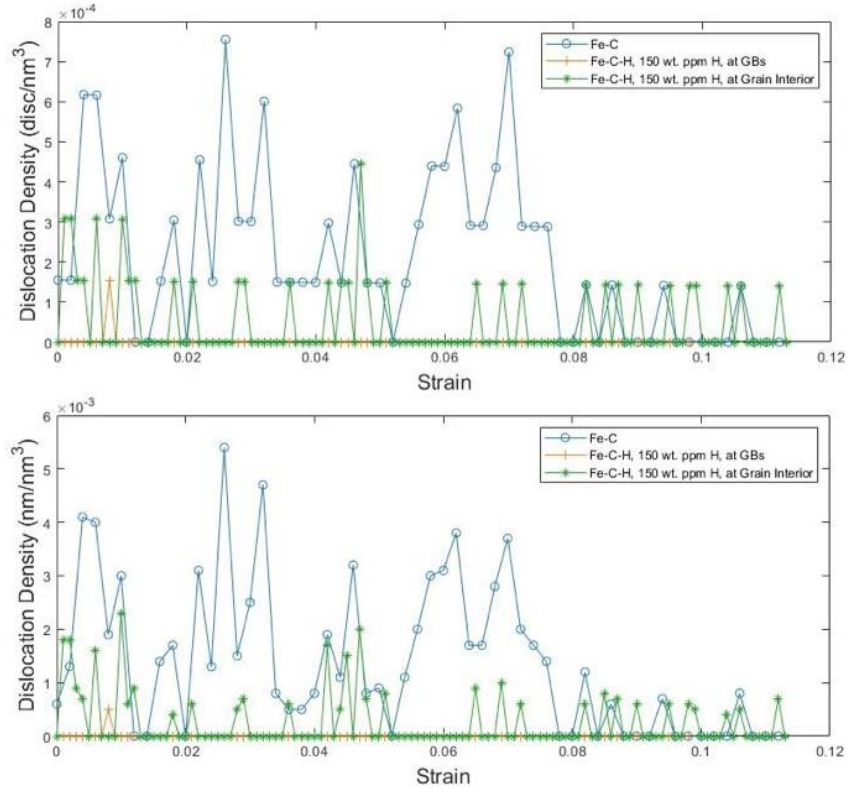

Figure 77 – Plots depicting dislocation density with increasing strain for the polycrystalline systems. Hydrogen concentration of 150 wt. ppm.

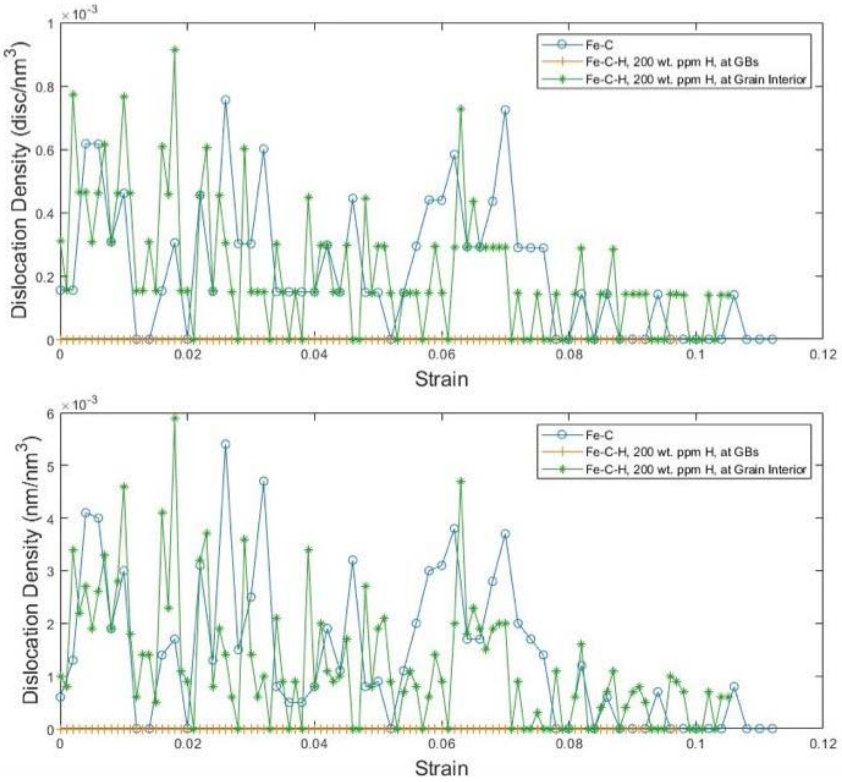

Figure 78 – Plots depicting dislocation density with increasing strain for the polycrystalline systems. Hydrogen concentration of 200 wt. ppm.

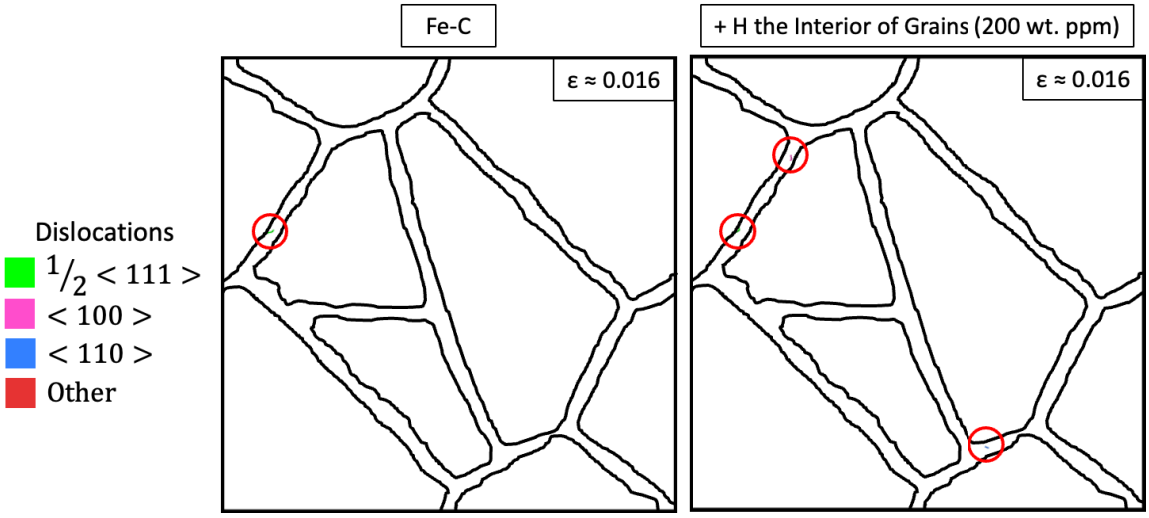

Figure 79 - Snapshot of the dislocations generated (red circle) in the base Fe-C system and Fe-C-H system with a hydrogen concentration of 200 wt. ppm at the interior of the grains. Even if this system with hydrogen generates more dislocations, their overall quantity remains quite low.

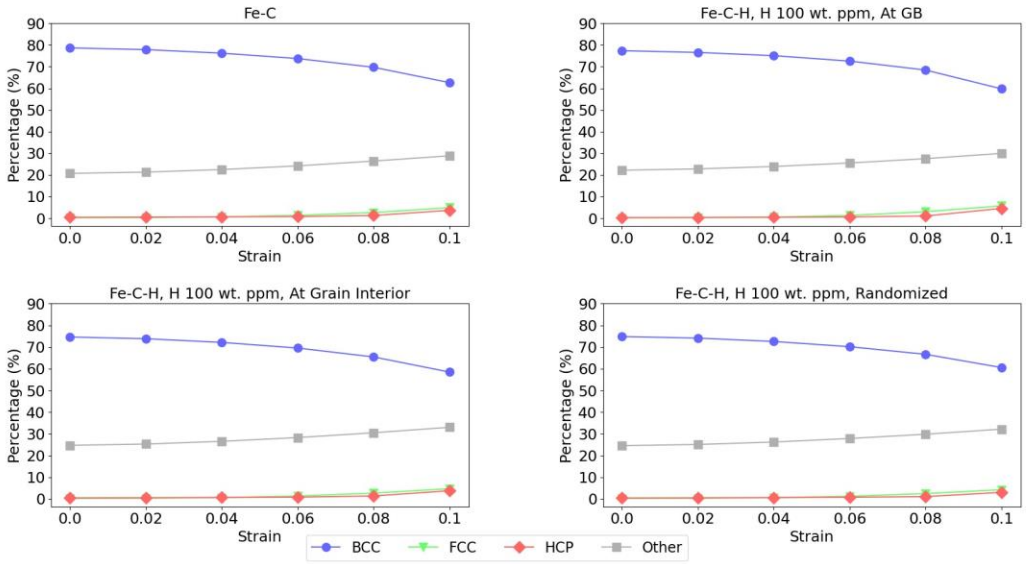

Figure 80 – Plots depicting the relative distribution of the structural phases with strain for the polycrystalline systems. Hydrogen concentration of 100 wt. ppm.

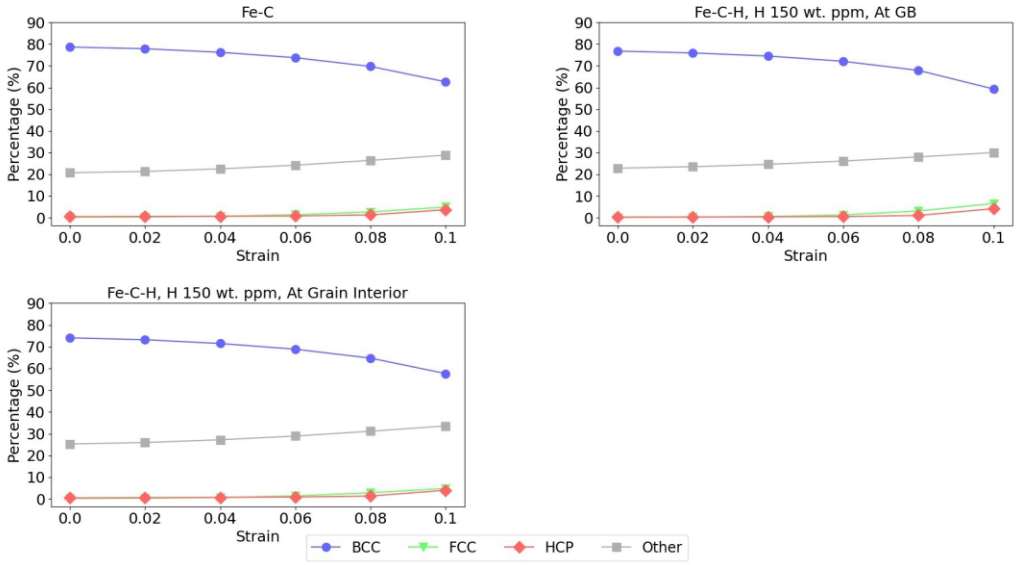

Figure 81 – Plots depicting the relative distribution of the structural phases with strain for the polycrystalline systems. Hydrogen concentration of 150 wt. ppm.

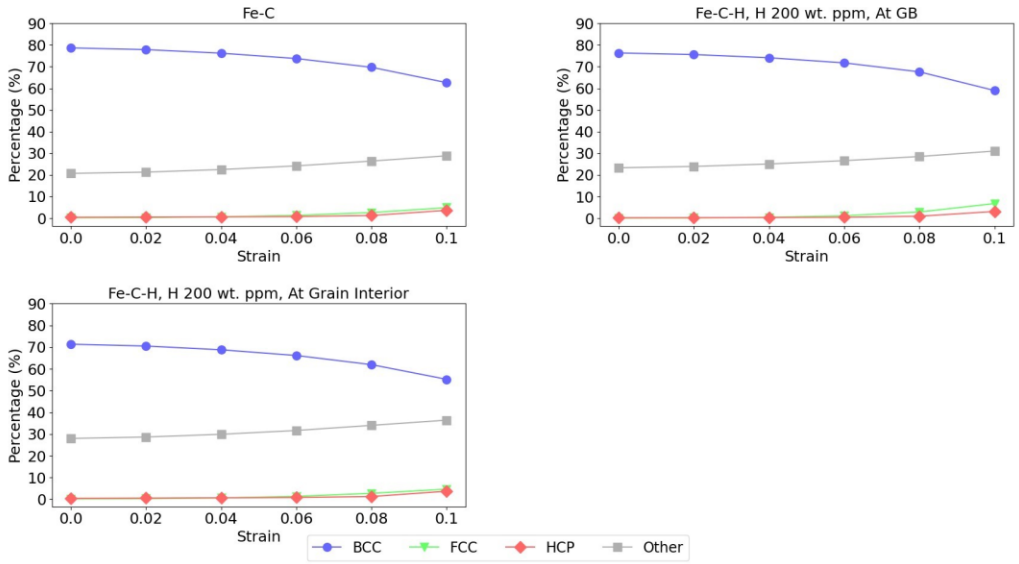

Figure 82 – Plots depicting the relative distribution of the structural phases with strain for the polycrystalline systems. Hydrogen concentration of 200 wt. ppm.

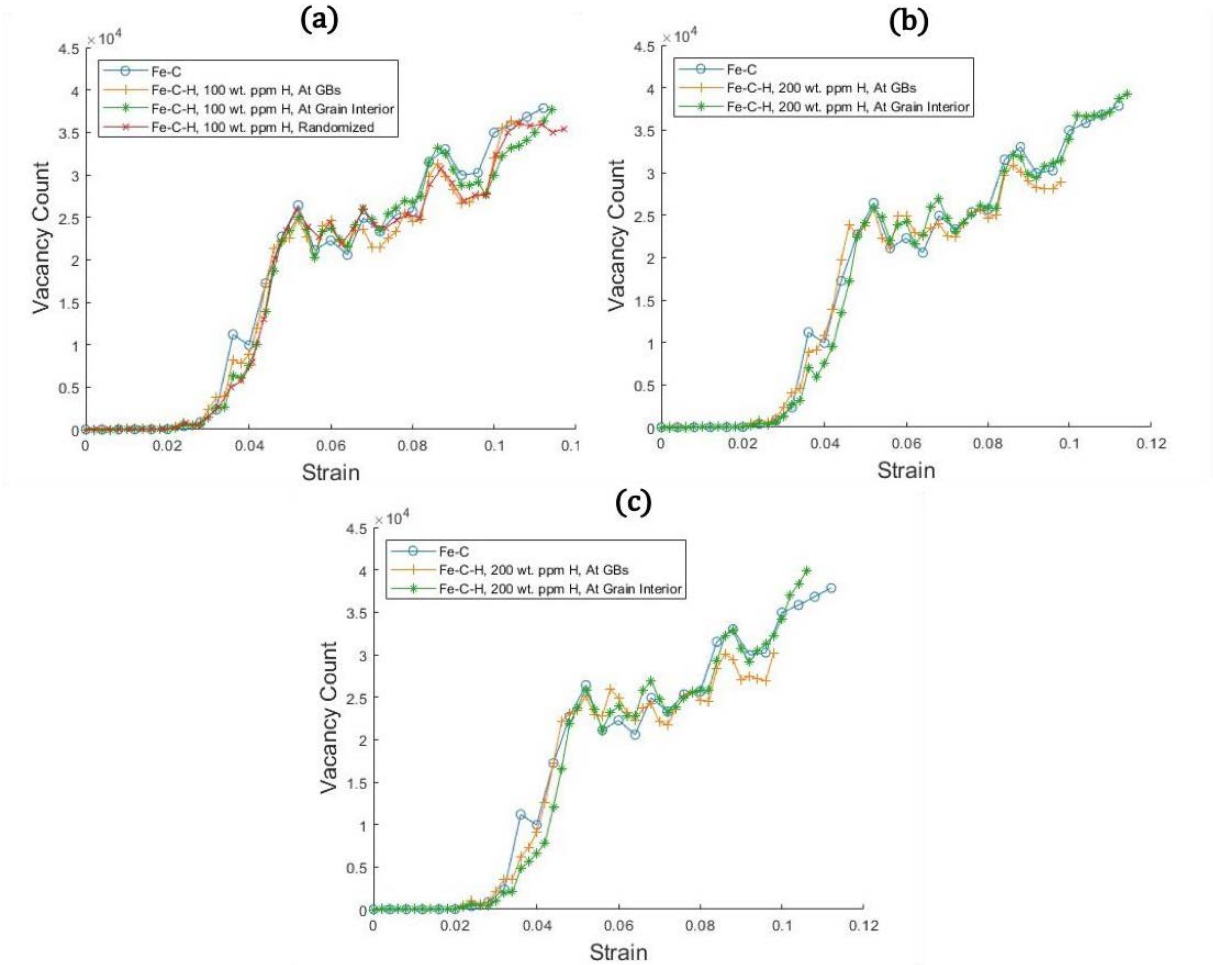

Figure 83 – Plots depicting vacancy count with increasing strain for the polycrystalline systems at different hydrogen concentrations: (a) 100 wt. ppm., (b) 150 wt. ppm. and (c) 200 wt. ppm.

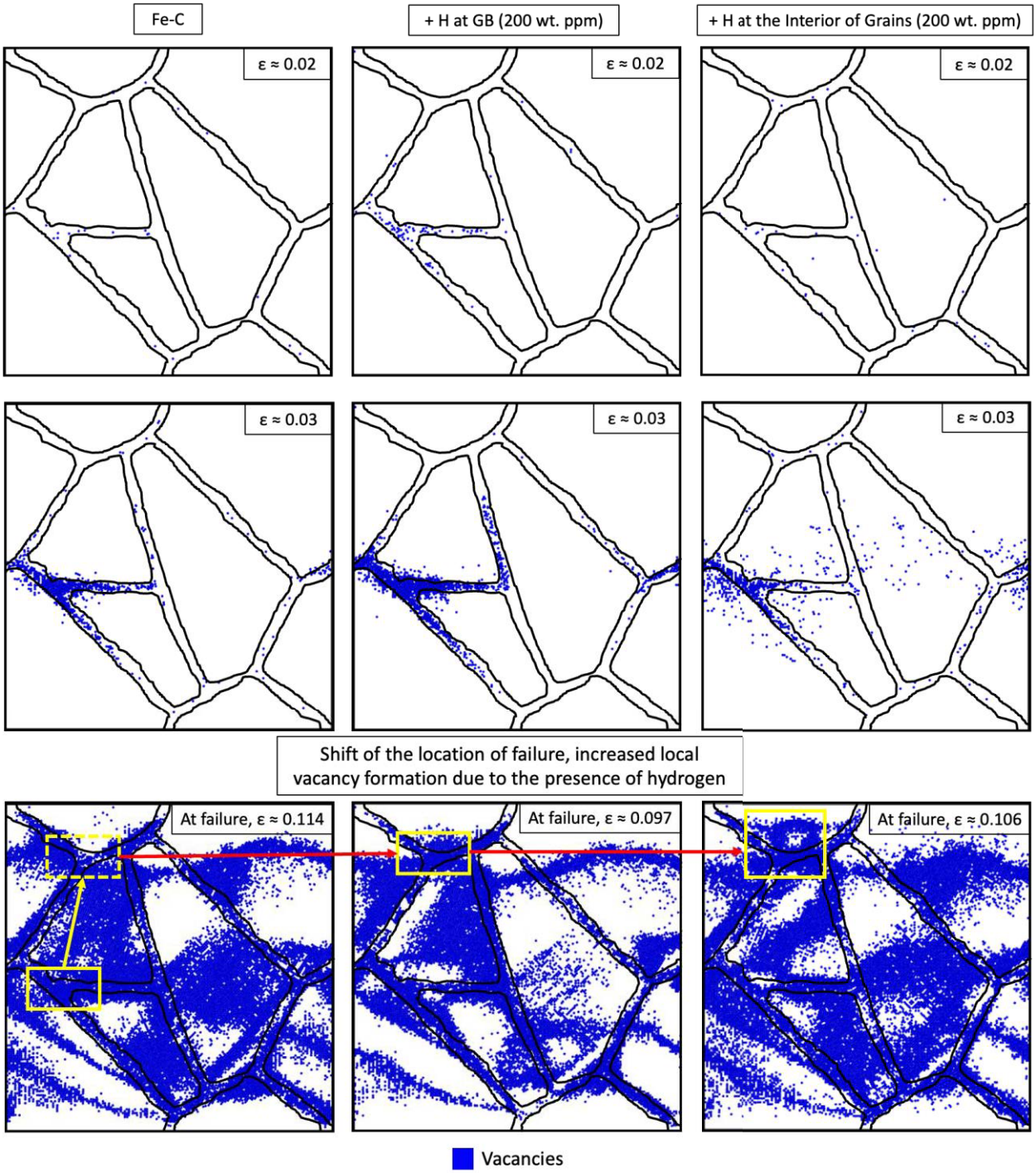

Figure 84 – Visualization of vacancies at different strains for Fe-C and Fe-C-H systems with the highest hydrogen concentration of 200 wt. ppm, using the MEAM potential. The blue spots correspond to vacancy sites. Notice how the presence of hydrogen increases the local formation of vacancies, enough to shift the area where the fracture occurs.

Chapter 5: Summary, Contributions, and Future Suggestions

5.1 Summary

This study has illuminated the effect of hydrogen on the mechanical properties of Fe-C systems by conducting MD simulations using recent BOP and MEAM potentials. The summary is presented in bullet points below, under different scopes, in an effort to precise the communication of key ideas.

Stress-strain response:

1. With both potentials, hydrogen generally induces a decline in peak stress and affects strain behavior before failure, with these effects modulated by the applied boundary conditions (periodic boundary conditions suppress fracture, while shrink-wrapped boundaries enhance it).
2. Hydrogen can affect peak stress and peak strain differently depending on the orientation, pointing to anisotropic properties. Naturally, by increasing complexity in the atomic models, such as the inclusion of many GBs in a polycrystalline model, anisotropy would be less noticeable.

Vacancy formation:

1. In the plastic region, hydrogen consistently promotes vacancy formation, indicative of the HESIV mechanism. However, there appears to be a threshold in local hydrogen concentration, beyond which vacancy formation may decrease, though still higher than in hydrogen-free scenarios as observed in the single-crystalline with the shrink-wrapped boundary condition, bicrystalline and polycrystalline models.
2. The bicrystalline and polycrystalline models clearly show that vacancy formation can be prominently initiated in areas with hydrogen presence.

3. Vacancy formation directly affects the failure point, as it increases local vacancies and void formation, leading to earlier failure.

Phase transformation:

1. Overall, the findings largely indicate that hydrogen does not significantly increase phase transformation, but nonetheless can activate this mechanism at a lower strain, causing earlier yielding. Conversely, carbon distinctly acts as a nucleation site for this process, as seen in the bicrystalline system.
2. The potential type has a great effect of phase transformation. The BOP potential exhibits higher transformation rates compared to the MEAM potential, which often shows minimal or no transformation under similar conditions, primarily due to overall lower stress levels reached in the latter.
3. Phase transformation seems to occur through lattice shearing, particularly favoring {110} planes. This shearing leads to visually distinct bands in the models that varies with the crystal orientation. Consequently, the orientation of the crystal directly determines the observable extent of phase transformation.

Dislocation emission:

1. There may be a specific hydrogen concentration range where hydrogen enhances dislocation emission, supporting HELP. However, exceeding this range appears to inhibit dislocation emission, as confirmed by numerous studies in the literature.
2. Dislocation emission seems more prevalent under the MEAM potential, possibly due to the significantly lower phase transformation rate. This reduction in energy release through phase transformation possibly leads to energy being discharged via dislocation emission instead.

3. The HELP mechanism is typically more active at lower strain rates, which are below the high strain rates usually employed in MD simulations.

HE mechanisms:

1. Among the HE mechanisms of HELP, HESIV, and HEDE, the HESIV mechanism was the most prominently observed in the current studied scenarios, with the results consistently pointing to a general and local increase in vacancy formation as hydrogen concentration increases.
2. Results from the bicrystalline and polycrystalline systems indicate that hydrogen enhances local vacancy formation and facilitates fracture through the interconnection of these vacancies, aligning with the HESIV mechanism. While there is no direct evidence to support HEDE, a potential synergistic interaction between HESIV and HEDE could lead to vacancy formation while simultaneously weakening cohesive strength at the GBs. This synergistic effect mirrors to a great extent the mechanisms proposed by various studies, but nonetheless HELP is also included as playing a role in transporting hydrogen to the GBs in those studies.

5.2 Contribution to original knowledge

This study aims to deepen the understanding of HE in Fe-C steels through MD simulations using two advanced Fe-C-H ternary interatomic potentials. It explores the impact of hydrogen on mechanical properties such as the stress-strain response across different atomic models, highlighting anisotropic properties in the single-crystalline models across various orientations. The research further reveals vacancy formation induced by hydrogen, particularly its role in material failure through the accumulation of local vacancies that coalesce into larger voids, leading to fracture. This is notably observed in the bicrystalline and polycrystalline models, where hydrogen can relocate the initial fracture location seen in the respective Fe-C model to new sites, i.e. to the

GBs or to areas near the original fracture location. Although conclusive evidence for the presence of HEDE is lacking, its interaction with HESIV could potentially enhance the observed degradation in mechanical properties, suggesting a synergistic effect between HESIV and HEDE. Additionally, the study provides insights into the potential effects of hydrogen on phase transformations and dislocation emissions, the former with preliminary findings on the HELP mechanism, though definitive conclusions remain pending. This thesis also serves to compare the two available BOP and MEAM Fe-C-H ternary potentials, aiming to assist in selecting the appropriate interatomic potential for future simulations, underscoring the suitability of the MEAM potential for complex scenarios. This is in contrast to the BOP, which demonstrates more aggressive phase transformation rates and might hinder or reduce the visibility on the effects of hydrogen.

5.3 Suggestions for future research

Despite the inherent limitations of MD, it remains a crucial tool in atomistic simulations, corroborating the observed behaviors and trends in the hydrogen interaction with Fe-C systems, provided that the interpretations are contextualized and validated against experimental data. As with any simulation, results are only as accurate as their inputs, so continuous analysis for inconsistencies is essential. The ongoing advancements in computational capacities are contributing significantly to the enrichment of the understanding through MD simulations, emphasizing the symbiotic relationship with experimental results. Therefore, carrying out key experiments designed to be closer, as much as possible, to what is used in simulation is the main suggestion for future work. This will help guide and verify the future MD simulations. In addition, the following points are suggested for the future research:

1. Reducing the strain rate if computational capacity limits permit.

2. Expand the model size for polycrystalline models by including more grains and incorporating a mix of low angle and high angle grain boundaries (GBs).
3. Alternatively, focus on mechanistic simulations by using smaller models.
4. Building expertise to create and adjust potentials in-house could be beneficial.

References

[1] Y. Murakami, “Hydrogen embrittlement” in *Metal Fatigue*, Elsevier, 2019, pp. 567–607. doi: 10.1016/b978-0-12-813876-2.00021-2.

[2] K. O. Findley, S. K. Lawrence, M. K. O’Brien, “Engineering challenges associated with hydrogen embrittlement in steels” in *Encyclopedia of Materials: Metals and Alloys*, Elsevier, 2021, pp. 235–249. doi: 10.1016/B978-0-12-819726-4.00086-7.

[3] S. G. Nnabuife, E. Oko, B. Kuang, A. Bello, A. P. Onwaulu, S. Oyagha, J. Whidborne, “The prospects of hydrogen in achieving net zero emissions by 2050: a critical review”, *Sustainable Chemistry for Climate Action,* vol. 2, p. 100024, Jan. 2023, doi: 10.1016/J.SCCA.2023.100024.

[4] G. A. Reigstad, S. Roussanaly, J. Straus, R. Anantharaman, R. de Kle, M. Akhurst, N. Sunny, W. Goldthorpe, L. Avignon, J. Pearce, S. Flamme, G. Guidati, E. Panos, C. Bauer, “Moving toward the low-carbon hydrogen economy: experiences and key learnings from national case studies”, *Advances in Applied Energy*, vol. 8, p. 100108, Dec. 2022, doi: 10.1016/J.ADAPEN.2022.100108.

[5] S. van Renssen, “The hydrogen solution?”, *Nature Climate Change*, vol. 10, no. 9, pp. 799–801, Aug. 2020, doi: 10.1038/s41558-020-0891-0.

[6] Z. Wang, J. Liu, F. Huang, Y. J. Bi, S. Q. Zhang, “Hydrogen diffusion and its effect on hydrogen embrittlement in DP steels with different martensite content”, *Frontiers in Materials*, vol. 7, p. 620000, Dec. 2020, doi: 10.3389/FMATS.2020.620000/BIBTEX.

[7] T. J. Carter, L. A. Cornish, “Hydrogen in metals”, *Engineering Failure Analysis*, vol. 8, no. 2, pp. 113–121, Apr. 2001, doi: 10.1016/S1350-6307(99)00040-0.

[8] O. Barrera, D. Bombac, Y. Chen, T.D. Daff, E. Galindo-Nava, P. Gong, D. Haley, R. Horton, I. Katzarov, J. R. Kermode, C. Liverani, M. Stopher, F. Sweeney, “Understanding and mitigating hydrogen embrittlement of steels: a review of experimental, modelling and design progress from atomistic to continuum”, *Journal of Materials Science*, vol. 53, no. 9. Springer New York LLC, pp. 6251–6290, May 01, 2018. doi: 10.1007/s10853-017-1978-5.

[9] M. Nagumo, “Preface” in *Fundamentals of Hydrogen Embrittlement*, Singapore: Springer Science, 2016, pp. v–vi.

[10] I. M. Robertson, P. Sofronis, A. Nagao, M.L. Martin, S. Wang, D. W. Gross, K. E. Nygren, “Hydrogen Embrittlement Understood”, *Metallurgical and Materials Transactions A: Physical Metallurgy and Materials Science*, vol. 46, no. 6, pp. 2323–2341, Jun. 2015, doi: 10.1007/s11661-015-2836-1.

[11] M. A. Mohtadi-Bonab, M. Masoumi, “Different aspects of hydrogen diffusion behavior in pipeline steel”, *Journal of Materials Research and Technology*, vol. 24, pp. 4762–4783, May 2023, doi: 10.1016/J.JMRT.2023.04.026.

[12] A. Drexler, B. Helic, Z. Silvayeh, K. Mraczek, C. Sommitsch, J. Domitner, “The role of hydrogen diffusion, trapping and desorption in dual phase steels”, *Journal of Materials Science*, vol. 57, no. 7, pp. 4789–4805, Feb. 2022, doi: 10.1007/S10853-021-06830-0/FIGURES/10.

[13] M. Nagumo, “Chapter 1 Solid Solution” in *Fundamentals of Hydrogen Embrittlement*, M. Nagumo, Ed., Singapur: Springer Science, 2016, pp. 1–6.

[14] D. E. Spearot, R. Dingreville, C. J. O'Brien, "Atomistic simulation techniques to model hydrogen segregation and hydrogen embrittlement in metallic materials" in *Handbook of Mechanics of Materials*, S. Schmauder, C.-S. Chen, K. K. Chawla, N. Chawla, W. Chen, Y. Kagawa, Eds., Singapore: Springer Nature, 2019, pp. 357–390.

[15] X. Li, X. Ma, J. Zhang, E. Akiyama, Y. Wang, X. Song, "Review of hydrogen embrittlement in metals: hydrogen diffusion, hydrogen characterization, hydrogen embrittlement mechanism and prevention", *Acta Metallurgica Sinica*, vol. 33, no. 6. Chinese Society for Metals, pp. 759–773, Jun. 01, 2020. doi: 10.1007/s40195-020-01039-7.

[16] A. S. Kholtobina, R. Pippan, L. Romaner, D. Scheiber, W. Ecker, V. I. Razumovskiy, "Hydrogen trapping in bcc iron", *Materials*, vol. 13, no. 10, May 2020, doi: 10.3390/ma13102288.

[17] P. Šesták, M. Friák, M. Šob, "The effect of hydrogen on the stress-strain response in Fe3Al: an ab initio molecular-dynamics study", *Materials*, vol. 14, no. 15, Aug. 2021, doi: 10.3390/ma14154155.

[18] S. Taketomi, R. Matsumoto, "Atomistic simulations of hydrogen effects on lattice defects in alpha iron", *Handbook of Mechanics of Materials*, pp. 283–300, Jan. 2019, doi: 10.1007/978-981-10-6884-3_11/FIGURES/5.

[19] D. Herlach, C. Kottler, T. Wider, K. Maier, "Hydrogen embrittlement of metals", *Physica B: Condensed Matter*, vol. 289–290, pp. 443–446, 2000, doi: 10.1016/S0921-4526(00)00431-2.

[20] X. Wu, H. Zhang, M. Yang, W. Jia, Y. Qiu, L. Lan, "From the perspective of new technology of blending hydrogen into natural gas pipelines transmission: mechanism,

experimental study, and suggestions for further work of hydrogen embrittlement in high-strength pipeline steels", *International Journal of Hydrogen Energy*, vol. 47, no. 12. Elsevier Ltd, pp. 8071–8090, Feb. 08, 2022. doi: 10.1016/j.ijhydene.2021.12.108.

[21] U. S. Meda, N. Bhat, A. Pandey, K. N. Subramanya, M. A. Lourdu Antony Raj, "Challenges associated with hydrogen storage systems due to the hydrogen embrittlement of high strength steels", *International Journal of Hydrogen Energy*, vol. 48, no. 47. Elsevier Ltd, pp. 17894–17913, Jun. 01, 2023. doi: 10.1016/j.ijhydene.2023.01.292.

[22] B. Sun, D. Wang, X. Lu, D. Wan, D. Ponge, X. Zhang, "Current challenges and opportunities toward understanding hydrogen embrittlement mechanisms in advanced high-strength steels: a review", *Acta Metallurgica Sinica*, vol. 34, no. 6. Chinese Society of Metals, pp. 741–754, Jun. 01, 2021. doi: 10.1007/s40195-021-01233-1.

[23] X. Xing, H. Zhang, G. Cui, J. Liu, Z. Li, "Hydrogen inhibited phase transition near crack tip – an atomistic mechanism of hydrogen embrittlement", *International Journal of Hydrogen Energy*, vol. 44, no. 31, pp. 17146–17153, Jun. 2019, doi: 10.1016/j.ijhydene.2019.04.205.

[24] J. Song, W. A. Curtin, "A nanoscale mechanism of hydrogen embrittlement in metals", *Acta Materialia*, vol. 59, no. 4, pp. 1557–1569, Feb. 2011, doi: 10.1016/j.actamat.2010.11.019.

[25] L. Dong, S. Wang, G. Wu, J. Gao, X. Zhou, H. Wu, X. Mao, "Application of atomic simulation for studying hydrogen embrittlement phenomena and mechanism in iron-based alloys", *International Journal of Hydrogen Energy*, vol. 47, no. 46, pp. 20288–20309, May 2022, doi: 10.1016/J.IJHYDENE.2022.04.119.

[26] L. S. Morrissey, S. Nakhla, “Molecular dynamics simulations of the hydrogen embrittlement base case: atomic hydrogen in a defect free single crystal”, *Molecular Simulation*, vol. 48, no. 13, pp. 1214–1222, Sep. 2022, doi: 10.1080/08927022.2022.2077936.

[27] J. Song, W. A. Curtin, “Atomic mechanism and prediction of hydrogen embrittlement in iron”, *Nature Materials*, vol. 12, no. 2, pp. 145–151, Feb. 2013, doi: 10.1038/nmat3479.

[28] J. Song, W. A. Curtin, “Mechanisms of hydrogen-enhanced localized plasticity: an atomistic study using α-Fe as a model system”, *Acta Materialia*, vol. 68, pp. 61–69, Apr. 2014, doi: 10.1016/j.actamat.2014.01.008.

[29] A. Tehranchi, W. A. Curtin, “The role of atomistic simulations in probing hydrogen effects on plasticity and embrittlement in metals”, *Engineering Fracture Mechanics*, vol. 216. Elsevier Ltd, Jul. 01, 2019. doi: 10.1016/j.engfracmech.2019.106502.

[30] X. Xing, G. Den, H. Zhang, G. Cui, J. Liu, Z. Li, B. Wang, S. Li., C. Qi, “Molecular dynamics studies of hydrogen effect on intergranular fracture in α-iron”, *Materials*, vol. 13, no. 21, pp. 1–15, Nov. 2020, doi: 10.3390/ma13214949.

[31] K. Matsubara, “Application of molecular dynamics calculations to elucidation of the mechanism of hydrogen-induced crack initiation in fracture toughness tests using tempered martensitic steels”, *ISIJ International*, vol. 62, no. 10, pp. 2107–2117, 2022, doi: 10.2355/isijinternational.ISIJINT-2022-153.

[32] R. Matsumoto, S. Seki, S. Taketomi, N. Miyazaki, “Hydrogen-related phenomena due to decreases in lattice defect energies - molecular dynamics simulations using the embedded

atom method potential with pseudo-hydrogen effects", *Computational Materials Science*, vol. 92, pp. 362–371, 2014, doi: 10.1016/j.commatsci.2014.05.029.

[33] W. H. Johnson, "II. On some remarkable changes produced in iron and steel by the action of hydrogen and acids", *Proceedings of the Royal Society of London*, vol. 23, no. 156–163, pp. 168–179, Dec. 1875, doi: 10.1098/RSPL.1874.0024.

[34] C. D. Beachem, "New model for hydrogen-assisted cracking (hydrogen embrittlement)", *Metallurgical Transactions*, vol. 3, no. 2, pp. 441–455, Jan. 1972, doi: 10.1007/BF02642048.

[35] L. B. Pfeil, "The effect of occluded hydrogen on the tensile strength of iron", *Royal Society*, vol. 112, no. 760, pp. 182–195, Aug. 1926, doi: 10.1098/RSPA.1926.0103.

[36] P. Cotterill, "The hydrogen embrittlement of metals", *Progress in Materials Science*, vol. 9, no. 4, pp. 205–301, 1961, doi: 10.1016/0079-6425(61)90005-6.

[37] A. R. Troiano, "The role of hydrogen and other interstitials in the mechanical behavior of metals: (1959 Edward De Mille Campbell Memorial Lecture)", *Metallography, Microstructure, and Analysis*, vol. 5, no. 6, pp. 557–569, Dec. 2016, doi: 10.1007/S13632-016-0319-4/FIGURES/20.

[38] S. A. Shipilov, "From first discoveries in the late 1800s to atomistic simulation and life prediction in the early 2000s: 130 years of stress corrosion cracking research" in *Environmental Degradation of Materials and Corrosion Control in Metals*, J. Luo, M. Elboujdaini, D. Shoesmith, P. C. Patnaik, Eds., Montreal: Canadian Institute of Mining, Metallurgy and Petroleum, 2003, pp. 127-158. 2

[39] R. Engelman, “The second industrial revolution, 1870-1914 - US history scene”. Accessed: Sep. 27, 2023. [Online]. Available: https://ushistoryscene.com/article/second-industrial-revolution/

[40] Stephanie Muntone, “Second Industrial Revolution | Education.com”. Accessed: Sep. 27, 2023. [Online]. Available: https://web.archive.org/web/20131022224325/http://www.education.com/study-help/article/us-history-glided-age-technological-revolution/

[41] T. J. Misa, “The making of modern America, 1865-1925”, A Nation of Steel, Feb. 2023, doi: 10.56021/9780801849671.

[42] D. S. Landes, “The unbound prometheus: technological change and industrial development in Western Europe from 1750 to the present, second edition”, *Cambridge University Press*, pp. 1–576, Jan. 2012, doi: 10.1017/CBO9780511819957.

[43] W. Macfarlane, *A Practical Guide to Iron and Steel Works Analyses: Being Selections from “Laboratory Notes on Iron and Steel Analyses”.* Madison: Longmans, Green, and Co., 1911.

[44] J. H. Andrew, “A few suggestions on the theories of occlusion of gases by metals”, *Transactions of the Faraday Society*, vol. 14, no. 0, pp. 232–239, Jan. 1919, doi: 10.1039/TF9191400232.

[45] W. C. Hothersall, “The spontaneous cracking of the necks of small arm cartridge cases”, *Transactions of the Faraday Society*, vol. 17, no. 0, pp. 201–208, Jan. 1921, doi: 10.1039/TF9211700201.

[46] A. R. Troiano, “The role of hydrogen and other interstitials in the mechanical behavior of metals: (1959 Edward De Mille Campbell Memorial Lecture)”, *Metallography, Microstructure, and Analysis*, vol. 5, no. 6, pp. 557–569, Dec. 2016, doi: 10.1007/S13632-016-0319-4/FIGURES/20.

[47] C. Miki, K. Homma, T. Tominaga, “High strength and high performance steels and their use in bridge structures”, *Journal of Constructional Steel Research*, vol. 58, no. 1, pp. 3–20, Jan. 2002, doi: 10.1016/S0143-974X(01)00028-1.

[48] R. Bjorhovde, “Development and use of high performance steel”, *Journal of Constructional Steel Research*, vol. 60, no. 3–5, pp. 393–400, 2004, doi: 10.1016/S0143-974X(03)00118-4.

[49] M. Y. Demeri, “Mechanical working (strain hardening)”, *Advanced High-Strength Steels - Science, Technology, and Applications*, 2013, Accessed: Apr. 02, 2024. [Online]. Available: https://www.asminternational.org/advanced-high-strength-steels-science-technology-and-applications/results/-/journal_content/56/05370G/PUBLICATION/

[50] W. M. Garrison, “Ultrahigh-strength steels for aerospace applications”, *JOM*, vol. 42, no. 5, pp. 20–24, May 1990, doi: 10.1007/BF03220942/METRICS.

[51] J. Li, D. Zhan, Z. Jiang, H. Zhang, Y. Yang, Y. Zhang, “Progress on improving strength-toughness of ultra-high strength martensitic steels for aerospace applications: a review”, *Journal of Materials Research and Technology*, vol. 23, pp. 172–190, Mar. 2023, doi: 10.1016/J.JMRT.2022.12.177.

[52] M. G. H. Wells, “Advances in steels for aerospace applications”, *Key Engineering Materials*, vol. 77–78, pp. 71–80, Jan. 1992, doi:10.4028/WWW.SCIENTIFIC.NET/KEM.77-78.71.

[53] Y. Tomita, “Development of fracture toughness of ultrahigh strength low alloy steels for aircraft and aerospace applications”, *Materials Science and Technology*, vol. 7, no. 6, pp. 481–489, 1991, doi: 10.1179/MST.1991.7.6.481.

[54] M. V. Maisuradze, M. A. Ryzhkov, “Microstructure and mechanical properties of high strength alloyed steel for aerospace application”, *Solid State Phenomena*, vol. 284, pp. 351–356, 2018, doi: 10.4028/WWW.SCIENTIFIC.NET/SSP.284.351.

[55] T. Okura, “Materials for Aircraft Engines”. Accessed: Oct. 31, 2023. [Online]. Available: https://www.colorado.edu/faculty/kantha/sites/default/files/attached-files/73549-116619_-_takehiro_okura_-_dec_17_2015_1027_am_-_asen_5063_2015_final_report_okura.pdf

[56] H. K. Birnbaum, “Mechanical properties of metal hydrides”, *Journal of the Less Common Metals*, vol. 104, no. 1, pp. 31–41, Dec. 1984, doi: 10.1016/0022-5088(84)90433-8.

[57] D. Eliezer, D. G. Chakrapani, C. J. Altstetter, E. N. Pugh, “The influence of austenite stability on the hydrogen embrittlement and stress- corrosion cracking of stainless steel”, *Metallurgical Transactions A*, vol. 10, no. 7, pp. 935–941, Jul. 1979, doi: 10.1007/BF02658313/METRICS.

[58] N. J. Petch, “The lowering of fracture-stress due to surface adsorption”, *Philosophical Magazine*, vol. 1, no. 4, pp. 331–337, 1956, doi: 10.1080/14786435608238106.

[59] D. Tromans, “On surface energy and the hydrogen embrittlement of iron and steels”, *Acta Metallurgica et Materialia*, vol. 42, no. 6, pp. 2043–2049, Jun. 1994, doi: 10.1016/0956-7151(94)90029-9.

[60] C. St. John, W. W. Gerberich, “Effect of loading mode on hydrogen embrittlement”, *Metallurgical Transactions*, vol. 4, no. 2, pp. 589–594, 1973, doi: 10.1007/BF02648714/METRICS.

[61] R. A. Oriani, “Whitney award lecture—1987: hydrogen—the versatile embrittler”, *Corrosion*, vol. 43, no. 7, pp. 390–397, Jul. 1987, doi: 10.5006/1.3583875.

[62] T. Tabata, H. K. Birnbaum, “Direct observations of the effect of hydrogen on the behavior of dislocations in iron”, *Scripta Metallurgica*, vol. 17, no. 7, pp. 947–950, Jul. 1983, doi: 10.1016/0036-9748(83)90268-5.

[63] S. W. Baek, E. J. Song, J. H. Kim, M. Jung, U. B. Baek, S. H. Nahm, “Hydrogen embrittlement of 3-D printing manufactured austenitic stainless steel part for hydrogen service”, *Scripta Materialia*, vol. 130, pp. 87–90, Mar. 2017, doi: 10.1016/J.SCRIPTAMAT.2016.11.020.

[64] B. Gangloff, B. Somerday, “Gaseous hydrogen embrittlement of materials in energy technologies. volume 2: mechanisms, modelling and future developments”. Accessed: Sep. 27, 2023. [Online]. Available: https://books.google.ca/books?hl=en&lr=&id=9YBwAgAAQBAJ&oi=fnd&pg=PP1&dq=industries+affected+by+hydrogen+embrittlement&ots=EHl34I6jxX&sig=38u-6u4KUa7U4B4Av8frEb7d-ho#v=onepage&q=industries%20affected%20by%20hydrogen%20embrittlement&f=false

[65] R. Srinivasan, T. Neeraj, “Hydrogen embrittlement of ferritic steels: deformation and failure mechanisms and challenges in the oil and gas industry” in *JOM*, 2014, pp. 1377–1382. doi: 10.1007/s11837-014-1054-4.

[66] L. Briottet, R. Batisse, P. Bernard, C. Duret-Thual, J. Heuzé, F. Martin, F. Thebault, F. Vucko, “Industrial consequences of hydrogen embrittlement”, *Mechanics - Microstructure - Corrosion Coupling: Concepts, Experiments, Modeling and Cases*, pp. 223–244, Jan. 2019, doi: 10.1016/B978-1-78548-309-7.50010-7.

[67] M. B. Djukic, G. M. Bakic, V. S. Zeravcic, A. Sedmak, B. Rajicic, “Hydrogen embrittlement of industrial components: prediction, prevention, and models”, *Corrosion*, vol. 72, no. 7, pp. 943–961, Jul. 2016, doi: 10.5006/1958.

[68] M. Koyama, C. C. Tasan, E. Akiyama, K. Tsuzaki, D. Raabe, “Hydrogen-assisted decohesion and localized plasticity in dual-phase steel”, *Acta Materialia*, vol. 70, pp. 174–187, May 2014, doi: 10.1016/j.actamat.2014.01.048.

[69] H. K. Birnbaum, P. Sofronis, “Hydrogen-enhanced localized plasticity—a mechanism for hydrogen-related fracture”, *Materials Science and Engineering: A*, vol. 176, no. 1–2, pp. 191–202, Mar. 1994, doi: 10.1016/0921-5093(94)90975-X.

[70] M. L. Martin, M. Dadfarnia, A. Nagao, S. Wang, P. Sofronis, “Enumeration of the hydrogen-enhanced localized plasticity mechanism for hydrogen embrittlement in structural materials”, *Acta Materialia*, vol. 165, pp. 734–750, Feb. 2019, doi: 10.1016/J.ACTAMAT.2018.12.014.

[71] Y. Sugiyama, K. Takai, “Quantities and distribution of strain-induced vacancies and dislocations enhanced by hydrogen in iron”, *Acta Materialia*, vol. 208, Apr. 2021, doi: 10.1016/j.actamat.2021.116663.

[72] M. B. Djukic, G. M. Bakic, V. Sijacki Zeravcic, A. Sedmak, B. Rajicic, “The synergistic action and interplay of hydrogen embrittlement mechanisms in steels and iron: localized plasticity and decohesion”, *Engineering Fracture Mechanics*, vol. 216. Elsevier Ltd, Jul. 01, 2019. doi: 10.1016/j.engfracmech.2019.106528.

[73] K. Tomatsu, T. Omura, T. Aoki, A. Yabuuchi, A. Kinomura, “Lattice defects underneath hydrogen-induced intergranular fracture surface of Ni-Cr alloy evaluated by low-energy positron beam”, *ISIJ International*, 2023, doi: 10.2355/isijinternational.isijint-2023-080.

[74] M. Nagumo, K. Takai, “The predominant role of strain-induced vacancies in hydrogen embrittlement of steels: overview”, *Acta Materialia*, vol. 165. Acta Materialia Inc, pp. 722–733, Feb. 15, 2019. doi: 10.1016/j.actamat.2018.12.013.

[75] M. Hatano, M. Fujinami, K. Arai, H. Fujii, M. Nagumo, “Hydrogen embrittlement of austenitic stainless steels revealed by deformation microstructures and strain-induced creation of vacancies”, *Acta Materialia*, vol. 67, pp. 342–353, Apr. 2014, doi: 10.1016/j.actamat.2013.12.039.

[76] K. Okada, A. Shibata, W. Gong, N. Tsuji, “Effect of hydrogen on evolution of deformation microstructure in low-carbon steel with ferrite microstructure”, *Acta Materialia*, vol. 225, Feb. 2022, doi: 10.1016/j.actamat.2021.117549.

[77] Y. Deng, A. Barnoush, “Hydrogen embrittlement revealed via novel in situ fracture experiments using notched micro-cantilever specimens”, *Acta Materialia*, vol. 142, pp. 236–247, Jan. 2018, doi: 10.1016/J.ACTAMAT.2017.09.057.

[78] P. Novak, R. Yuan, B. P. Somerday, P. Sofronis, R. O. Ritchie, “A statistical, physical-based, micro-mechanical model of hydrogen-induced intergranular fracture in steel”, *Journal of the Mechanics and Physics of Solids*, vol. 58, no. 2, pp. 206–226, Feb. 2010, doi: 10.1016/J.JMPS.2009.10.005.

[79] R. Falkenberg, W. Brocks, W. Dietzel, I. Scheider, “Modelling the effect of hydrogen on ductile tearing resistance of steels”, *International Journal of Materials Research*, vol. 101, no. 8, pp. 989–996, Aug. 2010, doi: 10.3139/146.110368/MACHINEREADABLECITATION/RIS.

[80] M. B. Djukic, G. M. Bakic, V. S. Zeravcic, A. Sedmak, B. Rajicic, “Hydrogen embrittlement of industrial components: prediction, prevention, and models”, *Corrosion*, vol. 72, no. 7, pp. 943–961, Jul. 2016, doi: 10.5006/1958.

[81] J. Rehrl, K. Mraczek, A. Pichler, E. Werner, “Mechanical properties and fracture behavior of hydrogen charged ahss/uhss grades at high- and low strain rate tests”, *Materials Science and Engineering: A*, vol. 590, pp. 360–367, Jan. 2014, doi: 10.1016/J.MSEA.2013.10.044.

[82] D. Sasaki, M. Koyama, H. Noguchi, “Factors affecting hydrogen-assisted cracking in a commercial tempered martensitic steel: Mn segregation, MnS, and the stress state around abnormal cracks”, *Materials Science and Engineering: A*, vol. 640, pp. 72–81, Jul. 2015, doi: 10.1016/J.MSEA.2015.05.083.

[83] H. Yu, J. S. Olsen, A. Alvaro, V. Olden, J. He, Z. Zhang, "A uniform hydrogen degradation law for high strength steels", *Engineering Fracture Mechanics*, vol. 157, pp. 56–71, May 2016, doi: 10.1016/J.ENGFRACMECH.2016.02.001.

[84] S. Wang, A. Nagao, P. Sofronis, I. M. Robertson, "Hydrogen-modified dislocation structures in a cyclically deformed ferritic-pearlitic low carbon steel", *Acta Materialia*, vol. 144, pp. 164–176, Feb. 2018, doi: 10.1016/J.ACTAMAT.2017.10.034.

[85] X. Li, B. Gong, C. Deng, Y. Li, "Failure mechanism transition of hydrogen embrittlement in AISI 304 K-TIG weld metal under tensile loading", *Corrosion Science*, vol. 130, pp. 241–251, Jan. 2018, doi: 10.1016/J.CORSCI.2017.10.032.

[86] Y. Song, M. Chai, W. Wu, Y. Liu, M. Qin, G. Cheng, "Experimental investigation of the effect of hydrogen on fracture toughness of 2.25cr-1mo-0.25v steel and welds after annealing", *Materials*, Vol. 11, Page 499, vol. 11, no. 4, p. 499, Mar. 2018, doi: 10.3390/MA11040499.

[87] I. M. Dmytrakh, R. L. Leshchak, A. M. Syrotyuk, R. A. Barna, "Effect of hydrogen concentration on fatigue crack growth behaviour in pipeline steel", *International Journal of Hydrogen Energy*, vol. 42, no. 9, pp. 6401–6408, Mar. 2017, doi: 10.1016/J.IJHYDENE.2016.11.193.

[88] R. Matsumoto, S. Taketomi, S. Matsumoto, N. Miyazaki, "Atomistic simulations of hydrogen embrittlement", *International Journal of Hydrogen Energy*, vol. 34, no. 23, pp. 9576–9584, Dec. 2009, doi: 10.1016/j.ijhydene.2009.09.052.

[89] S. Li, Y. Li, Y. Lo, T. Neeraj, R. Srinivasan, X. Ding, J. Sun, L. Qi, P. Gumbsch, J. Li, "The interaction of dislocations and hydrogen-vacancy complexes and its importance for

deformation-induced proto nano-voids formation in α-Fe", *International Journal of Plasticity*, vol. 74, pp. 175–191, Nov. 2015, doi: 10.1016/j.ijplas.2015.05.017.

[90] P. Sofronis, R. M. McMeeking, "Numerical analysis of hydrogen transport near a blunting crack tip", *Journal of the Mechanics and Physics of Solids*, vol. 37, no. 3, pp. 317–350, 1989, doi: 10.1016/0022-5096(89)90002-1.

[91] A. Tehranchi, W. A. Curtin, "Atomistic study of hydrogen embrittlement of grain boundaries in nickel: i. fracture", *Journal of the Mechanics and Physics of Solids*, vol. 101, pp. 150–165, Jan. 2017, doi: 10.1016/J.JMPS.2017.01.020.

[92] X. Zhou, M. E. Foster, J. A. Ronevich, C. W. San Marchi, "Review and construction of interatomic potentials for molecular dynamics studies of hydrogen embrittlement in Fe─C based steels", *Journal of Computational Chemistry*, vol. 41, no. 13, pp. 1299–1309, May 2020, doi: 10.1002/jcc.26176.

[93] S. Mun, N. Lee, D. Dickel, S. Adibi, B. Huddleston, R. Prabhu, K. Limmer, "A modified embedded atom method (MEAM) interatomic potential for the Fe-C-H system", Sep. 2021, Accessed: Jun. 01, 2023. [Online]. Available: https://arxiv.org/abs/2109.01712v2

[94] X. Zhang, G. Lu, "Multiscale modeling of hydrogen embrittlement", *Molecular Modeling of Corrosion Processes: Scientific Development and Engineering Applications*, pp. 223–249, May 2015, doi: 10.1002/9781119057666.CH8.

[95] Y. Ogawa, D. Birenis, H. Matsunaga, O. Takakuwa, J. Yamabe, Ø. Prytz, A. Thøgersen, "The role of intergranular fracture on hydrogen-assisted fatigue crack propagation in pure iron at a low stress intensity range", *Materials Science and Engineering: A*, vol. 733, pp. 316–328, Aug. 2018, doi: 10.1016/j.msea.2018.07.014.

[96] A. Pundt, R. Kirchheim, “Hydrogen in metals: microstructural aspects”, *Annual Review of Materials Research*, vol. 36, pp. 555–608, 2006, doi: 10.1146/ANNUREV.MATSCI.36.090804.094451.

[97] K. Sakaki, T Kawase, M. Hirato, M. Mizuno, H. Araki, Y. Shirai, M. Nagumo, “The effect of hydrogen on vacancy generation in iron by plastic deformation”, *Scripta Materialia*, vol. 55, no. 11, pp. 1031–1034, Dec. 2006, doi: 10.1016/j.scriptamat.2006.08.030.

[98] J. Gou, R. Nie, X. Xing, Z. Li, G. Cui, J. Liu, X. Deng, Y. F. Cheng, “Hydrogen-induced cracking of welded X80 steel studies by experimental testing and molecular dynamics modeling”, *Corrosion Science*, vol. 214, Apr. 2023, doi: 10.1016/j.corsci.2023.111027.

[99] X. Xing, F. Li, J. Liu, G. Cui, Z. Li, Y. F. Cheng, “Molecular dynamics modeling of hydrogen-induced plastic deformation and cracking of α-iron”, *Journal of Materials Science and Technology*, vol. 176, pp. 119–131, Mar. 2024, doi: 10.1016/j.jmst.2023.07.058.

[100] M. I. Mendelev, S. Han, D. J. Srolovitz, G. J. Ackland, D. Y. Sun, M. Asta, “Development of new interatomic potentials appropriate for crystalline and liquid iron”, *Philosophical Magazine*, vol. 83, no. 35, pp. 3977–3994, Dec. 2003, doi: 10.1080/14786430310001613264.

[101] I. Rohr, H. Nahme, K. Thoma, “Material characterization and constitutive modelling of ductile high strength steel for a wide range of strain rates”, *International Journal of Impact Engineering*, vol. 31, no. 4, pp. 401–433, Apr. 2005, doi: 10.1016/j.ijimpeng.2004.02.005.

[102] J. Zhang, Y. Li, X. Li, Y. Zhai, Q. Zhang, D. Ma, S. Mao, Q. Deng, Z. Li, X. Li, X. Wang, Y. Liu, Z. Zhang, X. Han, “Timely and atomic-resolved high-temperature mechanical

investigation of ductile fracture and atomistic mechanisms of tungsten", *Nature Communications*, vol. 12, no. 1, Dec. 2021, doi: 10.1038/s41467-021-22447-y.

[103] J. A. Hawreliak, S. J. Turneaure, "Probing the lattice structure of dynamically compressed and released single crystal iron through the alpha to epsilon phase transition", *Journal of Applied Physics*, vol. 129, no. 13, Apr. 2021, doi: 10.1063/5.0042605.

[104] S. J. Wang, M. L. Sui, Y. T. Chen, Q. H. Lu, E. Ma, X. Y. Pei, Q. Z. Li, H. B. Hu, "Microstructural fingerprints of phase transitions in shock-loaded iron", *Scientific Reports*, vol. 3, Jan. 2013, doi: 10.1038/srep01086.

[105] N. Gunkelmann, E. M. Bringa, K. Kang, G. J. Ackland, C. J. Ruestes, H. M. Urbassek, "Polycrystalline iron under compression: plasticity and phase transitions", *Physical Review B - Condensed Matter and Materials Physics*, vol. 86, no. 14, Oct. 2012, doi: 10.1103/PhysRevB.86.144111.

[106] H. T. Luu, N. Gunkelmann, "Pressure-induced phase transformations in Fe-C: molecular dynamics approach", *Computational Materials Science*, vol. 162, pp. 295–303, May 2019, doi: 10.1016/j.commatsci.2019.03.011.

[107] T. Q. Nguyen, K. Sato, Y. Shibutani, "First-principles study of bcc/fcc phase transition promoted by interstitial carbon in iron", *Materials Transactions*, vol. 59, no. 6, pp. 870–875, 2018, doi: 10.2320/matertrans.M2018014.

[108] A. Castedo, J. Sanchez, J. Fullea, M. C. Andrade, P. L. De Andres, "Ab initio study of the cubic-to-hexagonal phase transition promoted by interstitial hydrogen in iron", *Physical Review B - Condensed Matter and Materials Physics*, vol. 84, no. 9, Sep. 2011, doi: 10.1103/PhysRevB.84.094101.

[109] S. Jiang, Y. Huang, K. Wang, X. Li, H. Deng, S. Xiao, W. Zhu, W. Hu, "Effects of vacancies on plasticity and phase transformation in single-crystal iron under shock loading", *Journal of Applied Physics*, vol. 130, no. 1, Jul. 2021, doi: 10.1063/5.0043880.

[110] J. L. Shao, P. Wang, F. G. Zhang, A. M. He, "Hcp/fcc nucleation in bcc iron under different anisotropic compressions at high strain rate: molecular dynamics study", *Scientific Reports*, vol. 8, no. 1, pp. 1–10, May 2018, doi: 10.1038/s41598-018-25758-1.

[111] C. Cayron, "One-step theory of fcc-bcc martensitic transformation", *Acta Crystallographica Section A: Foundations of Crystallography*, vol. 69, no. 5, pp. 498–509, Nov. 2012, doi: 10.1107/S0108767313019016.

[112] W. Ma, Y. Dong, M. Yu, Z. Wang, Y. Liu, N. Gao, L. Dong, X. Wang, "Evolution of symmetrical grain boundaries under external strain in iron investigated by molecular dynamics method", *Metals*, vol. 12, no. 9, Sep. 2022, doi: 10.3390/met12091448.

[113] Y. Lu, S. Sun, Y. Zeng, Q. Deng, Y. Chen, Y. Li, X. Li, L. Wang, X. Han, "Atomistic mechanism of nucleation and growth of a face-centered orthogonal phase in small-sized single-crystalline Mo", *Materials Research Letters*, vol. 8, no. 9, pp. 348–355, Sep. 2020, doi: 10.1080/21663831.2020.1764122.

[114] J. B. Liu, D. D. Johnson, "Bcc-to-hcp transformation pathways for iron versus hydrostatic pressure: coupled shuffle and shear modes", *Physical Review B - Condensed Matter and Materials Physics*, vol. 79, no. 13, Apr. 2009, doi: 10.1103/PhysRevB.79.134113.

[115] G. Sainath, B. K. Choudhary, "Orientation dependent deformation behaviour of BCC iron nanowires", *Computational Materials Science*, vol. 111, pp. 406–415, Jan. 2016, doi: 10.1016/J.COMMATSCI.2015.09.055.

[116] G. Aral, Y. J. Wang, S. Ogata, A. C. T. Van Duin, "Effects of oxidation on tensile deformation of iron nanowires: insights from reactive molecular dynamics simulations", *Journal of Applied Physics*, vol. 120, no. 13, Oct. 2016, doi: 10.1063/1.4963828/143856.

[117] G. Sainath, B. K. Choudhary, T. Jayakumar, "Molecular dynamics simulation studies on the size dependent tensile deformation and fracture behaviour of body centred cubic iron nanowires", *Computational Materials Science*, vol. 104, pp. 76–83, Jun. 2015, doi: 10.1016/J.COMMATSCI.2015.03.053.

[118] A. Raina, N. Sime, "Effects of anisotropy and regime of diffusion on the measurement of lattice diffusion coefficient of hydrogen in metals", *Proceedings: Mathematical, Physical and Engineering Sciences*, vol. 474, no. 2215, pp. 1–17, 2018, doi: 10.2307/26583487.

[119] J. Wang, B. Shao, D. Shan, B. Guo, Y. Zong, "The effect of hydrogen on plastic anisotropy of mg and α-ti/zr from first-principles calculations", *Materials*, vol. 16, no. 8, Apr. 2023, doi: 10.3390/MA16083016/S1.

[120] N. K. Mohandas, A. Giorgini, M. Vanazzi, T. Riemslag, S. P. Scott, V. Popovich, "Hydrogen embrittlement of inconel 718 manufactured by laser powder bed fusion using sustainable feedstock: effect of heat treatment and microstructural anisotropy", *Metals, Vol. 13, Page 418*, vol. 13, no. 2, p. 418, Feb. 2023, doi: 10.3390/MET13020418.

[121] J. Toribio, "Anisotropy of hydrogen embrittlement in cold drawn pearlitic steel: a tribute to mantegna", *Procedia Structural Integrity*, vol. 28, pp. 2438–2443, 2020, doi: 10.1016/J.PROSTR.2020.11.094.

[122] J. Toribio, D. Vergara, “Role of microstructural anisotropy in the hydrogen-assisted fracture of pearlitic steel notched bars”, *International Journal of Fracture*, vol. 182, no. 1, pp. 149–156, Jul. 2013, doi: 10.1007/S10704-013-9844-1/METRICS.

[123] A. Kimura, H. Kimura, “Hydrogen embrittlement in high purity iron single crystals”, *Materials Science and Engineering*, vol. 77, no. C, pp. 75–83, Jan. 1986, doi: 10.1016/0025-5416(86)90355-1.

[124] W. Wang, H. Fu, H. Zhang, Y. Yan, J. Li, “Effect of grain orientation on hydrogen embrittlement behavior of interstitial-free steel”, *Metals, Vol. 12, Page 981*, vol. 12, no. 6, p. 981, Jun. 2022, doi: 10.3390/MET12060981.

[125] L. Feng, X. Zhang, W. Li, M. Xiang, X. Yao, “Anisotropy and grain size dependence of the effects of hydrogen on the shock-induced spallation in iron”, *International Journal of Mechanical Sciences*, vol. 256, p. 108536, Oct. 2023, doi: 10.1016/J.IJMECSCI.2023.108536.

[126] R. Schneider, A. Raj Sharma, A. Raj, “Introduction to molecular dynamics” in *Lecture Notes in Physics*, 2008, pp. 3–40.

[127] G. C. Abell, “Empirical chemical pseudopotential theory of molecular and metallic bonding”, *Physical Review B*, vol. 31, no. 10, p. 6184, May 1985, doi: 10.1103/PhysRevB.31.6184.

[128] J. Tersoff, “Empirical interatomic potential for carbon, with applications to amorphous carbon”, *Physical Review Letters*, vol. 61, no. 25, p. 2879, Dec. 1988, doi: 10.1103/PhysRevLett.61.2879.

[129] A. Horsfield, A. Bratkovsky, M. Fearn, D. Pettifor, M. Aoki, “Bond-order potentials: theory and implementation”, *Physical Review B*, vol. 53, no. 19, p. 12694, May 1996, doi: 10.1103/PhysRevB.53.12694.

[130] T. Q. Nguyen, K. Sato, Y. Shibutani, “Development of Fe-C interatomic potential for carbon impurities in α-iron”, *Computational Materials Science*, vol. 150, pp. 510–516, Jul. 2018, doi: 10.1016/J.COMMATSCI.2018.04.047.

[131] M. I. Baskes, “Modified embedded-atom potentials for cubic materials and impurities”, *Physical Review B*, vol. 46, no. 5, p. 2727, Aug. 1992, doi: 10.1103/PhysRevB.46.2727.

[132] M. I. Baskes, B. J. Lee, H. Kim, Y. Koo Cho, “Second nearest-neighbor modified embedded atom method potentials for bcc transition metals”, *Physical Review B*, vol. 64, no. 18, p. 184102, Oct. 2001, doi: 10.1103/PhysRevB.64.184102.

[133] “Atomsk”. Accessed: Jan. 17, 2023. [Online]. Available: https://atomsk.univ-lille.fr/

[134] P. Hirel, “Atomsk: a tool for manipulating and converting atomic data files”, *Computer Physics Communications*, vol. 197, pp. 212–219, Dec. 2015, doi: 10.1016/j.cpc.2015.07.012.

[135] “LAMMPS Molecular Dynamics Simulator”. Accessed: Jan. 05, 2023. [Online]. Available: https://www.lammps.org/#gsc.tab=0

[136] “OVITO – Open Visualization Tool – Scientific visualization and analysis software for atomistic simulation data”. Accessed: Jan. 06, 2023. [Online]. Available: https://www.ovito.org/

[137] “MATLAB - MathWorks - MATLAB & Simulink”. Accessed: Jan. 06, 2023. [Online]. Available: https://www.mathworks.com/products/matlab.html

[138] “Welcome to python.org”. Accessed: May 16, 2023. [Online]. Available: https://www.python.org/

[139] “Common neighbor analysis — OVITO user manual 3.7.12 documentation”. Accessed: Jan. 19, 2023. [Online]. Available: https://www.ovito.org/docs/current/reference/pipelines/modifiers/common_neighbor_analysis.html#particles-modifiers-common-neighbor-analysis

[140] “Dislocation analysis (DXA) — OVITO user manual 3.7.12 documentation”. Accessed: Jan. 10, 2023. [Online]. Available: https://www.ovito.org/docs/current/reference/pipelines/modifiers/dislocation_analysis.html#particles-modifiers-dislocation-analysis

[141] A. Stukowski, V. V. Bulatov, A. Arsenlis, “Automated identification and indexing of dislocations in crystal interfaces”, *Modelling and Simulation in Materials Science and Engineering*, vol. 20, no. 8, Dec. 2012, doi: 10.1088/0965-0393/20/8/085007.

[142] “Wigner-Seitz defect analysis — OVITO User Manual 3.7.12 documentation”. Accessed: Jan. 11, 2023. [Online]. Available: https://www.ovito.org/docs/current/reference/pipelines/modifiers/wigner_seitz_analysis.html#particles-modifiers-wigner-seitz-analysis

[143] “boundary command — LAMMPS documentation”. Accessed: Jan. 05, 2023. [Online]. Available: https://docs.lammps.org/boundary.html

[144] “min_style cg command — LAMMPS documentation”. Accessed: Jan. 05, 2023. [Online]. Available: https://docs.lammps.org/min_style.html

[146] “8.2.5. Barostats — LAMMPS documentation”. Accessed: Jan. 05, 2023. [Online]. Available: https://docs.lammps.org/Howto_barostat.html

[146] “fix nvt command — LAMMPS documentation”. Accessed: May 16, 2023. [Online]. Available: https://docs.lammps.org/fix_nh.html

[147] “Atomsk - tutorial - grain boundary”. Accessed: Jun. 25, 2023. [Online]. Available: https://atomsk.univ-lille.fr/tutorial_grainboundaries.php

[148] “Atomsk - tutorial - polycrystals”. Accessed: Jun. 25, 2023. [Online]. Available: https://atomsk.univ-lille.fr/tutorial_polycrystal.php

[149] Y. Qin, H. Yu, J. Zhang, “Fast and memory-efficient voronoi diagram construction on triangle meshes”, *Computer Graphics Forum*, vol. 36, no. 5, pp. 93–104, Aug. 2017, doi: 10.1111/CGF.13248.

[150] C. Bohler, R. Klein, A. Lingas, C. H. Liu, “Forest-like abstract voronoi diagrams in linear time”, *Computational Geometry: Theory and Applications*, vol. 68, pp. 134–145, Mar. 2018, doi: 10.1016/j.comgeo.2017.06.013.

[151] “Voronoi tessellations – H. Paul Keeler”. Accessed: Jun. 25, 2023. [Online]. Available: https://hpaulkeeler.com/voronoi-dirichlet-tessellations/

[152] M. Ortiz, J. Ovejero-Garcia, “Effect of hydrogen on Young’s modulus of AISI 1005 and 1070 steels”, *Journal of Materials Science*, vol. 27, no. 24, pp. 6777–6781, Dec. 1992, doi: 10.1007/BF01165968/METRICS.

[153] Z. Tongyi, C. Wuyang, X. Jimei, J. Fangxin, “Effect of hydrogen on the Young’s modulus of iron”, *Chinese Journal of Engineering*, vol. 7, no. 1, pp. 55–65, 1985, doi: 10.13374/j.issn1001-053x.1985.01.019.